Technical Physics Letters, Vol. 29, No. 1, 2003, pp. 1–4. Translated from Pis'ma v Zhurnal Tekhnicheskoĭ Fiziki, Vol. 29, No. 1, 2003, pp. 3–12.
Original Russian Text Copyright © 2003 by Arapov, Volkov.

The Formation and Structure of Current Cells in a Vacuum Arc Cathode Spot

S. S. Arapov and N. B. Volkov
Institute of Electrophysics, Ural Division, Russian Academy of Sciences, Yekaterinburg, Russia
e-mail: nbv@ami.uran.ru
Received July 18, 2002

Abstract—A physical model describing the structurization and localization of electric current in the surface layer of a cathode in the initial stage of a vacuum arc discharge is proposed. According to this model, each current cell on the cathode surface represents a dislocation cell containing a ring electron vortex with the axis perpendicular to the electrode surface. It is shown that localization of the electric current at the vortex center leads to the formation of a spatial structure of hot spots acting as precursors of the explosive emission centers, the dynamics of which determines operation of the vacuum discharge. © *2003 MAIK "Nauka/Interperiodica".*

The main problem in the physics of vacuum discharge is explaining a mechanism of discharge initiation and operation [1, 2]. It is commonly accepted that a so-called cathode spot appears on the clean surface of a "cold" cathode as a result of the electric explosion of a microscopic cusp heated by the emission current (explosive electron emission) [1, 2]. In the course of the experiments described in [3], a preexplosion state and the initial stage of the electric explosion in the field emission center were observed on the cathode of an electron projector. It was established that the radius of an emission region at the time instant immediately before explosion was about 5 μm. It was suggested that this emission region represented a melt from which a microscopic cusp protruded as a result of the hydrodynamic surface instability development [4], this cusp giving rise to the explosive electron emission process. According to the results obtained in [3], the time of the microscopic cusp formation was $t_s \approx 0.1$ ns.

While there are no principal obstacles to explaining the formation of the primary explosive emission centers (or ectons according to [2]), the problem of describing the formation of secondary emission centers on the cathode surface under plasma encounters certain difficulties. As a rule, this process is described based on various ad hoc hypotheses [2, 5]. The number of such assumptions can be significantly decreased by using the hypothesis of Kesaev [6], according to which the cathode spot consists of current cells [7]. After the recent experiments of Juttner [8] and Vogel [9], it can be considered firmly established that the cathode spots possess an internal structure. According to [8], the size of the cathode spot element is $\lambda < 5$ μm. The X-ray emission with an energy of 100 eV and a duration of 0.33–1.4 ns, observed in [9] from the cathode spot at a current of 1.2–35 A (for an arc discharge initiated by a laser radiation in copper vapor), exhibited a spatial structure of bright (hot) spots with dimensions on the order of $\lambda \approx 3$ μm (the number of spots increased with the discharge current, while their dimensions remained unchanged).

Let us estimate the electric current density in the above hot spots assuming that these objects consist of a copper plasma possessing a temperature of 100 eV, the density of the corresponding solid, and a conductivity of $\sigma \approx 0.6 \times 10^6$ Ω/m (which is a lower limit of the conductivity of such plasmas [10]). Then, taking the values of i = 1.2 A and an emission pulse duration of τ = 0.33 ns, we obtain estimates for a minimum current density $j_{\min} = 2.05 \times 10^9$ A/cm^2 and a hot spot diameter d_{sp} = 0.28 μm (the corresponding volume and mass being $V_{sp} = 1.149 \times 10^{-20}$ m^3 and $M_{sp} = 1.026 \times 10^{-16}$ kg, respectively). The lower estimate of the cathode voltage drop can be obtained as $U_c = jd_{sp}\sigma^{-1}$. For j = 1.2 A, this yields U_c = 9.6 V (cf. with an experimental value of $U_{c,\,exp}$ = 15 V for an arc operating in copper vapor [11]). According to [6], the experimental minimum current through a cell is $I_{cm} = 2I_0$, where I_0 is the threshold arc current (1.6 A for Cu and W [6]); $i = 2I_{cm}$ corresponds to two cells operating simultaneously.

A comparison of the cathode spot dynamics for thin-film and bulk cathodes [6] showed that, for a film thickness of $h_{sl} \geq 1.5$ μm, the values of the crater size, the current, and the cathode drop virtually coincide with the corresponding data for a massive cathode. According to Puchkarev *et al.* [12, 13], nanosecond vacuum arcs can exist at $i < I_0$: for i = 0.8–8 A, the arc voltage and current on a wire cathode with a diameter of 100 μm behaved similarly to the analogous values in [6] (where the arc lived for milliseconds). Under these conditions, a single cycle of arc operating for 50–250 ns was observed at a tungsten point cathode with a tip radius below 0.3 μm [13]; after quenching of the arc,

1063-7850/03/2901-0001$24.00 © 2003 MAIK "Nauka/Interperiodica"

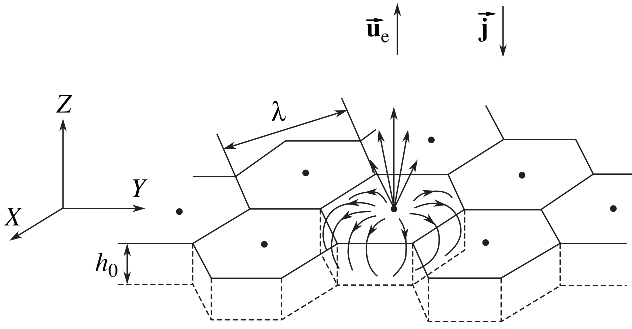

Fig. 1. Schematic diagram of the spatial structure of dislocation cells with ring electron vortices (black dots indicate the hot spots—precursors of the explosive emission centers).

the radius of the fused cathode tip was 1–1.5 μm. In the region of threshold currents, there are considerable fluctuations δU in the cathode voltage drop: when a cathode spot moves to a new site in an arc with $i = 2$ A at a tungsten cathode, this scatter reaches $\delta U = 5$–10 V. A minimum current density estimated from the cathode spot patterns is $j_{\min} \approx (1–2) \times 10^7$ A/cm^2 [14].

The above experimental data can be consistently interpreted only within the framework of the models employing the hypothesis of current cells. Unfortunately, the questions as to when the current cells are formed and what is their structure were not considered in the original papers [2, 6, 7]. The aim of this study was to consider the formation of the spatial structure of the current cells and hot spots (as precursors of the primary explosive emission centers) in the initial stage of a vacuum discharge (this removes difficulties related to the formation of secondary emission centers). We will also obtain some quantitative characteristics of the current cells (see also [15]).

Current cell formation in the initial stage of a vacuum discharge requires certain conditions to be fulfilled in the surface layer of a cathode. From the standpoint of mechanics, the plastic flow of a material with a large density of dislocations is analogous to the flow of an incompressible liquid possessing a large shear viscosity. Let us assume that the emission region with a diameter of 5 μm (such as was observed in [3]) represents the surface layer of a field-emitting cathode saturated with dislocations (the density of dislocations in the surface layers of a material is much greater than that in the bulk [16]). According to the modern physics of plasticity [17], there are four levels of plastic deformation corresponding to different spatial scales λ: (i) microscopic, with $\lambda_m = (1–30)a$, where a is the crystal lattice constant; (ii) mesoscopic, featuring the formation of dislocated substructures with $\lambda_{sub} = 0.1$–3 μm; (iii) structural, with $\lambda_{st} = 20$–200 μm; and (iv) macroscopic, with $\lambda_m \geq 10\lambda_{st}$. Based on the sound velocity C_s (which is limiting for the motion of dislocations), we conclude that the mesoscopic level is characterized (for $C_{s0} = 4 \times 10^3$ m/s in tungsten [18]) by a time scale $t_{sub} \approx 0.025$–0.75 ns. The mean free path of dislocations $l_d = 0.1$–10 μm [17] corresponds to a time scale of $t_\lambda \approx 0.025$–2.5 ns. As can be seen, the aforementioned estimate for the time of the liquid metal cusp formation [3] falls within the interval of times characteristic of the mesoscopic level of plastic deformation. The above estimate ($d_{sp} = 0.28$ μm) of the hot spot diameter for the experiments of Vogel [9] also falls within the range of dimensions characteristic of the mesoscopic level.

These data allow us to put forward the hypothesis that current cells are essentially dislocation cells formed in the surface layer (saturated with dislocations) of a cathode on the mesoscopic level of plastic deformation [17, 19, 20]. According to the reaction-diffusion models of the dislocation kinetics, a characteristic scale of the dislocated structures is $\lambda = (1–10)h$ [19], where h is the thickness of the so-called plastic zone (in our case, $h = h_{sl} = 1.5$ μm [6]). It was demonstrated [21] that hot spots are formed at the axes of the ring electron (current) vortices arising in an incompressible liquid metal conductor (carrying current) as a result of the convective magnetohydrodynamic (MHD) instability with the most rapidly developing mode corresponding to the perturbation wavelength

$$\lambda = 2.32L, \quad (1)$$

where $L \sim h_{sl}$ is a characteristic scale in the problem under consideration. The presence of dislocations in the solid conductor leads to a change in the internal geometry [22, 23] which (by analogy with the case of a liquid metal conductor featuring hydrodynamic vortices) favors the development of a convective MHD instability in the solid conductor (carrying current) and the formation of ring electron vortices inside the cells [23].

Taking into account peculiarities of the electromagnetic field topology, we can formulate the main idea of this study as follows: the current cell represents a hexagonal dislocation cell containing a ring electron vortex with the axis perpendicular to the cathode surface and a characteristic size of $\lambda = 2.32h_{sl} = 3.48$ μm (for $h_{sl} = 1.5$ μm). This hypothesis is illustrated by Fig. 1, showing a qualitative pattern of the current cell structure (black dots indicate the localization of hot spots).

In order to provide for the conditions necessary and sufficient for hot spot explosion, after which the material of the current cell is emitted into the discharge gap, it is necessary to introduce an energy equal to the heat of sublimation $W_{sub} = j^2 d_{sp}(C_{s0}\sigma)^{-1}$ [15] into the metal over a period of time shorter than the sound propagation time, so that

$$Q_* = U_c j_* = W_{sub} C_{s0}. \quad (2)$$

Here, U_c is the voltage drop across a hot spot (which serves as a lower estimate for the cathode potential drop); j_* is the current density at the cell axis (Fig. 1); W_{sub} is the sublimation energy; and C_{s0} is the sound

velocity in the metal under normal conditions. Equation (2) determines the power flux Q_* required for the formation of hot spots in a given metal within a finite time: $Q_* = 2.722 \times 10^{14}$ W/m^2 (for Cu) and 6.135×10^{14} W/m^2 (for W). The quantities Q_*, I_{cm}, and h_{sl} are the main quantitative characteristics of a system of current cells and hot spots (precursors of the explosive emission centers or ectons). Once the j_* value is known, Eq. (2) gives a lower estimate of the cathode potential drop. For the above estimate ($j_{min} = 2.05 \times 10^9$ A/cm^2) of the lower current density in the experiments of Vogel [9], we obtain $U_c = 13.5$ V (cf. with $U_{c,\,exp} = 15$ V for an arc operating in copper vapor [11]).

Using Eq. (2), we can evaluate the minimum current density j_{min} in the explosive emission centers at a given arc discharge voltage U_0. For a copper cathode, $U_a = 20$ V [11] and, hence, $j_{min} = 1.386 \times 10^9$ A/cm^2; for a tungsten cathode, $U_a = 25$–30 V [11] and $j_{min} = (2.045$–$2.454) \times 10^9$ A/cm^2 (the lower value of j_{min} corresponds to $U_a = 30$ V). These estimates of j_{min} (for $I_{cm} = 3.2$ A) correspond to the following values of the hot spot diameter and the characteristic current cell size: for Cu, $d_{sp} = 0.542$ μm, $\lambda = 3.542$ μm; for W, $d_{sp} = 0.407$–0.446 μm, $\lambda = 3.407$–3.446 μm. Formula (1) gives the characteristic current cell size of $\lambda = 3.48$ μm.

Although the above estimates of the characteristic current cell size were obtained based on various considerations, the values are in a satisfactory agreement. The loss of a current cell is determined by emission of the material into the discharge gap as a result of the microexplosion. Assuming that the resulting crater (formed at the cell site) has a hemispherical shape, we can estimate the minimum current density at which the current cell is lost: for $i \sim 1$–3.2 A, $j_{min} \sim (0.7$–$2.26) \times 10^7$ A/cm^2. This value agrees well with the experimental estimates obtained for j_{min} in [14] using the cathode spot patterns in the region of threshold currents: $j_{min} = (1$–$2) \times 10^7$ A/cm^2. Substituting these values into Eq. (2) confirms that no current cell can exist at such small current densities because $U_c = (3.07$–$6.135) \times 10^3$ V $\gg U_a$.

According to Hähner [20], hexagonal dislocation cells form as a result of a nonequilibrium phase transition induced by noise (i.e., by fluctuations of the stress and the deformation rate) in the statistical ensemble of dislocations. At a certain noise level, the dislocation distribution function exhibits a qualitative change [20]. The characteristic size of the dislocation cell is determined by the correlation length ξ of the dislocation ensemble [20]:

$$\lambda \approx 2\xi = (2\pi)^{-1}(\mu b(\alpha S)^{-1})^{1/2}\rho^{-1/4}, \tag{3}$$

where $\alpha = 0.3$ [20]; μ is the shear modulus; b is the Burgers vector (following [20], below we will use $b = 2.5 \times 10^{-10}$ m); $S = 2.5 \times 10^{-3}\langle\tau^{int}\rangle$ [24, 25] is the response function corresponding to mutual transformations of the deformation rate and effective stress fluctuations; $\langle\tau^{int}\rangle$ is the time-averaged stress determined by dynamics of the dislocation ensemble (a good estimate being provided by the yield point σ_T); and ρ is the dislocation density.

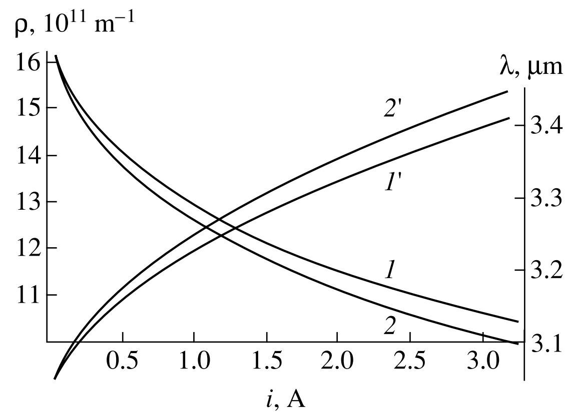

Fig. 2. Plots of (*1*', *2*') the characteristic current cell size λ and (*1*, *2*) the corresponding dislocation densities ρ versus current amplitude at the working arc voltages $U_a = 25$ (*1*, *1*') and 30 V (*2*, *2*') calculated using formula (3) for a tungsten cathode with $\mu = 1.515 \times 10^{12}$ Pa and $\langle\tau^{int}\rangle = \sigma_T = 1.08 \times 10^8$ Pa.

Figure 2 presents the plots of the characteristic current cell size and the corresponding dislocation densities versus current amplitude for two values of the working arc voltage on a tungsten cathode, $U_a = 25$ V (curves *1*' and *1*) and 30 V (curves *2*' and *2*, respectively), calculated using formula (3) for $\mu = 1.515 \times 10^{12}$ Pa (the average shear modulus for tungsten from the range of $\mu = (8.8$–$23.5) \times 10^{11}$ Pa [26]) and $\langle\tau^{int}\rangle = \sigma_T = 1.08 \times 10^8$ Pa [26]. As can be seen, the density of dislocations necessary for current cell formation significantly decreases with increasing current. The estimates of the dislocation density are very close to those observed in the surface layers of metals [16]. It should be taken into account that the energy of dislocation formation near the surface is significantly lower as compared to that in the bulk and that the electric current passage favors the production of dislocations [23].

Now let us briefly consider a possible scenario of cathode spot operation. Initiation of vacuum discharge leads to the formation of current cells at an amount necessary for normal arc operation in the electric circuit with a given power supply source. In the range of threshold currents ($i \le I_{cm}$), only one current cell is initially formed, while the other cells occur in the latent state. After emitting material into the discharge gap, the primary current cell can no longer obey condition (2) and ceases to operate. This leads to an increase in the voltage drop across the surface layer of the cathode and the near-cathode dense layer of the plasma containing a condensed disperse phase of the material. As a result,

the current redistributes between the exhausted cell and one of the neighboring cells. Selection of the second cell among the set of potential ones is determined by the maximum Poynting vector on the cathode surface. Thus, as the current drops in the primary cell and builds up in the secondary cell, two cells are simultaneously operating with $I_c < I_{cm}$. Upon the loss of the former cell, the latter operates alone until onset of the loss process, after which the process is repeated as described above. Since the arc cannot operate on sites occupied by the lost cells, the symmetry of the initial structure of current cells is broken and the spatiotemporal evolution of the cells acquires a random character. In the case of greater arc currents, many cells operate simultaneously. The probability of losing a separate cell and initiating a new one from the latent set is greater at the edge of the cathode spot. For this reason, the cathode spot slowly migrates toward the maximum Poynting vector.

Thus, we have proposed a physical model describing the structurization and localization of electric current (with the formation of hot spots–precursors of the explosive emission centers), which consistently explains an entire set of experimental facts. Current cells, representing hexagonal dislocation cells containing ring electron vortices, are formed in the surface layer of the cathode in the initial stage of vacuum discharge as a result of nonlinear interaction between conduction electrons and an ensemble of dislocations. The structure of current cells and hot spots is characterized by three basic parameters: (i) the thickness of the dislocation-saturated cathode surface layer h_{sl} ($h_{sl} = 1.5$ μm [6]); (ii) the limiting cell current I_{cm} ($I_{cm} = 3.2$ A for W and Cu [6]); and (iii) the power flux necessary for explosive emission center formation Q_* ($Q_* = 2.722 \times 10^{14}$ W/m^2 for Cu and 6.135×10^{14} W/m^2 for W).

Acknowledgments. The authors are grateful to G.A. Mesyats, L.M. Baskin, G.A. Dyuzhev, and N. Vogel for their interest in this study and for stimulating, fruitful discussions of various aspects of the proposed physical model.

This study was supported by the Russian Foundation for Basic Research, project nos. 97-02-16177 and 00-02-17428.

REFERENCES

1. G. A. Mesyats and D. I. Proskurovsky, *Pulsed Discharges in Vacuum* (Springer-Verlag, Berlin, 1989).
2. G. A. Mesyats, Pis'ma Zh. Éksp. Teor. Fiz. **57**, 88 (1993) [JETP Lett. **57**, 95 (1993)]; Usp. Fiz. Nauk **165**, 601 (1995) [Phys. Usp. **38**, 567 (1995)]; G. A. Mesyats, *Cathode Phenomena in a Vacuum Discharge: The Breakdown, the Spark and the Arc* (Nauka, Moscow, 2000).
3. A. V. Batrakov, S. A. Popov, and D. I. Proskurovskiĭ, Pis'ma Zh. Éksp. Teor. Fiz. **67**, 280 (1998) [JETP Lett. **67**, 299 (1998)].
4. N. M. Zubarev, Zh. Éksp. Teor. Fiz. **114**, 2043 (1998) [JETP **87**, 1110 (1998)]; Phys. Rev. E **65**, 055301 (2002).
5. A. A. Valuev and G. E. Norman, Zh. Éksp. Teor. Fiz. **116**, 2176 (1999) [JETP **89**, 1180 (1999)].
6. I. G. Kesaev, *Cathode Processes of Vacuum Arc* (Nauka, Moscow, 1968).
7. L. P. Harris, *Vacuum Arcs, Theory and Applications,* Ed. by J. M. Lafferty (Wiley, New York, 1980).
8. B. Juttner, IEEE Trans. Plasma Sci. **27**, 836 (1999).
9. N. Vogel, Pis'ma Zh. Éksp. Teor. Fiz. **67**, 622 (1998) [JETP Lett. **67**, 647 (1998)]; *Proceedings of XVIII International Symposium on Discharge and Insulation into Vacuum, 1998* (Technical University, Eindhoven, 1998), Vol. 1, p. 202; IEEE Trans. Plasma Sci. **27**, 864 (1999).
10. N. B. Volkov and A. Z. Nemirovsky, J. Phys. D **24**, 693 (1991); N. B. Volkov, Doctoral Dissertation in Physics and Mathematics (Yekaterinburg, 1999).
11. *Handbook of Vacuum Arc Science and Technology: Fundamentals and Applications*, Ed. by R. L. Boxman, D. M. Sanders, and Ph. J. Martin (Noyes Publ., Park Ridge, 1995).
12. V. F. Puchkarev, D. I. Proskurovskiĭ, and A. M. Murzakaev, Zh. Tekh. Fiz. **57**, 2324 (1987) [Sov. Phys. Tech. Phys. **32**, 1405 (1987)].
13. V. F. Puchkarev, D. I. Proskurovskiĭ, and A. M. Murzakaev, Zh. Tekh. Fiz. **58**, 88 (1988) [Sov. Phys. Tech. Phys. **33**, 51 (1988)].
14. V. F. Puchkarev and A. M. Murzakaev, J. Phys. D **23**, 26 (1990).
15. A. M. Mourzakaev and N. B. Volkov, in *Proceedings of XVIII International Symposium on Discharge and Insulation into Vacuum, 1998* (Technical University, Eindhoven, 1998), Vol. 1, p. 302; N. B. Volkov, in *Proceedings of 1st International Congress on Radiation Physics, High Current Electronics, and Modification of Materials, Tomsk, Russia, 2000* (Institute of High Current Electronics, Tomsk, 2000), Vol. 2, p. 94.
16. V. P. Alekhin, in *Physics of Strength and Plasticity of the Surface Layers of Materials* (Nauka, Moscow, 1983).
17. V. I. Vladimirov and A. E. Romanov, *Disclinations in Crystals* (Nauka, Leningrad, 1986).
18. V. N. Zharkov and V. A. Kalinin, *The Equations of State of Solids under High Pressures and Temperatures* (Nauka, Moscow, 1968).
19. E. C. Aifantis, Int. J. Eng. Sci. **33**, 2161 (1995).
20. P. Hähner, Acta Mater. **44**, 2345 (1996).
21. N. B. Volkov and A. M. Iskoldsky, J. Phys. A **26**, 6635 (1993); **26**, 6649 (1993); **26**, 6667 (1993); N. B. Volkov, Doctoral Dissertation in Physics and Mathematics (Yekaterinburg, 1999).
22. J. Fridel, *Dislocations* (Pergamon, Oxford, 1964); A. Kadić and D. G. B. Edelen, *A Gauge Theory of Dislocations and Disclinations* (Springer-Verlag, Berlin, 1983).
23. N. B. Volkov, J. Phys. A **30**, 6391 (1997).
24. S. I. Basinski and Z. S. Basinski, *Dislocations in Solids,* Ed. by F. R. N. Nabarro (North-Holland, Amsterdam, 1979), Vol. 4, p. 261.
25. U. F. Kocks, A. S. Argon, and M. F. Ashby, Prog. Mater. Sci. **19**, 256 (1975).
26. *Tables of Physical Quantities*, Ed. by I. N. Kikoin (Atomizdat, Moscow, 1976).

Translated by P. Pozdeev

Technical Physics Letters, Vol. 29, No. 1, 2003, pp. 12–15. Translated from Pis'ma v Zhurnal Tekhnicheskoĭ Fiziki, Vol. 29, No. 1, 2003, pp. 27–35.
Original Russian Text Copyright © 2003 by Kagadeĭ, Nefyodtsev, Proskurovsky, Romanenko, Shirokova.

The Effect of Hydrogenation on the Sink Breakdown Voltage of Transistors Based on Ion-Doped Gallium Arsenide Structures

V. A. Kagadeĭ[a], E. V. Nefyodtsev[a], D. I. Proskurovsky[b], S. V. Romanenko[b], and L. S. Shirokova[b]

[a] *Institute of Semiconductor Devices, State Research and Production Enterprise, Tomsk, Russia*

[b] *Institute of High-Current Electronics, Siberian Division, Russian Academy of Sciences, Tomsk, Russia*

e-mail: vak@lve.hcei.tsc.ru

Received June 26, 2002

Abstract—It was found that the hydrogenation of ion-doped gallium arsenide structures leads to an increase in the sink breakdown voltage of high-power microwave Schottky barrier field effect transistors based on such structures (from 7 up to 17 V) and in the power of related microwave integration circuits (by a factor of up to 2.4). Data characterizing the dependence of the increase in the transistor breakdown voltage and the device power on the hydrogenation regime are presented. Possible mechanisms explaining the effect of hydrogenation on the electrical properties of gallium arsenide and the parameters of semiconductor devices are considered. © *2003 MAIK "Nauka/Interperiodica".*

The characteristics of high-power microwave Schottky barrier field effect transistors (SBFETs) and related microwave integration circuits (ICs) are determined to a considerable extent by electrical properties of the channel–substrate junctions and semi-insulating gallium arsenide (GaAs) substrates [1]. Most of the microwave devices implementing SBFETs are based on ion-doped GaAs structures, which is explained by the simplicity and high production efficiency of ion implantation technology. However, the electrical properties of such ion-implanted structures are far from being ideal and the resulting SBFETs are characterized by a low sink breakdown voltage (about 7–8 V) and, hence, by a comparatively low power. These drawbacks are related to the lack of sharp channel–substrate interface, the presence of electrically active centers (defects) in the subsurface substrate layer, and the absence of high-quality insulation between the semi-insulating GaAs substrate and the active layers [1].

As is known, the hydrogenation of the subsurface layers of epitaxial and ion-doped GaAs structures in atomic hydrogen leads to passivation of a number of electrically active shallow and deep centers [2, 3]. This treatment was reported to result in an increase of the reverse voltage of Schottky diodes [4, 5], suppression of backgating [6], a decrease in the photoconductivity relaxation time, and improvement of the current–voltage characteristics of SBFETs [7]. Therefore, further research in this direction is of considerable interest.

The experiments were performed on n^+–n type structures obtained by implanting Si^+ ions into semi-insulating GaAs plates. The electron concentration was $n_e \cong (1.5–2) \times 10^{18}$ cm^{-3} in the contact (n^+-GaAs) layer and 3×10^{17} cm^{-3} in the active (n-GaAs) layer, the thicknesses of these layers being 0.1 and 0.2 μm, respectively. Each plate was divided into two parts, one of which was subjected to hydrogenation treatment and the other served as a control. In order to prevent the chemical interaction of atomic hydrogen with GaAs on the control part, the surface was coated with a 5-nm-thick SiO_2 film grown by the method of plasmachemical deposition. The hydrogenation was effected in a flow of atomic hydrogen using a setup described elsewhere [8]. A flow with a density of 10^{15} cm^{-2} s^{-1} was produced by a source employing low-pressure arc discharge [8]. The sample temperature during hydrogenation was T = 100–200°C, the hydrogen pressure in the working chamber was 10^{-2} Pa, and the treatment duration (t_h) was varied from 5 to 200 min.

According to the results of our measurements of the capacitance–voltage characteristics, the density of charge carriers in the n^+-GaAs contact layer at a depth of 0.07 μm decreased to $n_e \cong (2–6) \times 10^{17}$ cm^{-3}. This fact indicated that atomic hydrogen penetrated into the ion-doped layer and formed electrically neutral complexes with dopant atoms. Subsequent annealing of the samples in nitrogen at 475°C for 10 min led to decay of the neutral complexes and to complete restoration of the carrier density: $(1.5–2) \times 10^{18}$ cm^{-3} at a depth of 0.025 μm. According to the experimental data presented in [9], such annealing should not significantly change the concentration of hydrogen complexes with deep centers (which decompose at a temperature much higher than that used for the annealing). This conclusion was confirmed by data on the backgating via support and also by the kinetics of photoconductivity relaxation in a biased sample structure measured as described in [6, 7]. The results of these measurements

1063-7850/03/2901-0012$24.00 © 2003 MAIK "Nauka/Interperiodica"

Table 1. The parameters of the test Schottky FETs (gate width, 100 μm) and working ICs based on nonhydrogenated samples (1–3) and the analogous structures (1AB–3AB) hydrogenated for various times

Sample number (t_h)	Saturation current, mA	Transconductance, mA/(V mm)	Cutoff voltage, V	Saturation voltage, V	Breakdown voltage, V	IC power (1.5 GHz), W
1, 2, 3	8–10	110–130	1–1.1	1.2–1.3	6–7	1.2
1AB (30 min)	10–14	125–150	1–1.4	1.2–1.5	17.5	4.2
2AB (5 min)	9–10	120	1	1	9	1.7
3AB (200 min)	12–14	110	1.2–1.3	1.4	11	2.8

Table 2. The parameters of the test SBFETs (gate width, 100 μm) and working ICs based on nonhydrogenated samples (4, 5) and the analogous hydrogenated structures (4AB, 5AB)

Sample number (t_h)	Saturation current, mA	Transconductance, mA/(V mm)	Cutoff voltage, V	Saturation voltage, V	Breakdown voltage, V	IC power (1.5 GHz), W
4	8–10	115–135	0.9–1.1	1.2–1.3	6–7	1.2
5	8–9	100	1	1	8	1.4
4AB (40 min)	11–14	130–150	1–1.2	1.3–1.5	17.5	4.2
5AB (40 min)	9–12	100–125	1.2–1.4	1.3–1.5	18	3.8

showed that the initial (nonhydrogenated) sample structures are characterized by low backgating and by fast photoconductivity relaxation. Subsequent hydrogenation for 10–120 min, followed by annealing, led to a certain decrease in the backgating via support and in the photoconductivity relaxation time. These changes are indicative of passivation of deep centers [6, 7].

Characterized with respect to the electrical properties as described above, the hydrogenated and control parts of each plate were used to create microwave ICs involving high-power buried-gate SBFETs fabricated by the same technological route. Table 1 presents the parameters of test SBFETs and working microwave ICs based on nonhydrogenated (control) structures and those hydrogenated for various times (t_h). As can be seen, the hydrogenation does not lead to significant changes in most of the transistor parameters except for the sink breakdown voltage U_b. The samples hydrogenated for t_h = 30 min exhibit a certain increase in the transconductance, a sharp growth in the U_b value (from 6–7 V in the control to 17.5 V), and a significant increase in the device power (from 1.2 to 4.2 W). For shorter (5 min) and longer (200 min) hydrogenation times, the breakdown voltage increase is not as pronounced (U_b = 9–11 V). The results of these experiments showed that a twofold increase in U_b is achieved for t_h = 20–120 min.

Table 2 presents the results of determination of the parameters of test SBFETs and working microwave ICs based on the structures hydrogenated for t_h = 40 min in comparison to the control. As is seen, the hydrogenated SBFETs possess a 2–2.5 times greater sink breakdown voltage and, accordingly, a higher working power. In addition, the hydrogenation leads to some increase in the transconductance and saturation current of the transistor.

The experimental dependence of U_b on the hydrogenation time is determined by the total amount of atomic hydrogen dissolved in GaAs and by the hydrogen concentration in the n^+–n junction, at the doped layer–substrate interface, and/or in the semi-insulating GaAs substrate. A similar increase in the reverse voltage of Schottky diodes formed directly on the surface of epitaxial GaAs structures (Fig. 1a) was previously observed after hydrogenation for a shorter time (t_h = 5 min) [5]. In the microwave SBFETs with a buried gate (Fig. 1b), the same effect is obtained after a longer treatment (t_h = 20–120 min) because atomic hydrogen has to penetrate to a greater depth.

This explanation was confirmed by calculations of the hydrogen penetration into an n^+–n structure performed using the model described in [10–12] and developed in our recent paper [13]. The refined model takes into account the process of hydrogen diffusion and the formation and decay of hydrogen molecules

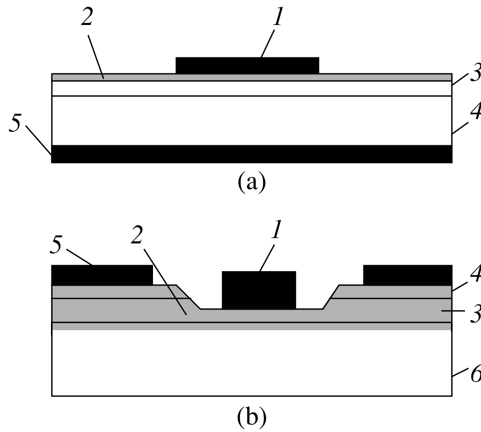

Fig. 1. Schematic diagrams showing the cross sections of hydrogenated epitaxial GaAs-based structures of (a) a surface Schottky barrier diode and (b) an ion-doped buried-gate SBFET (shaded area indicates the region of hydrogen penetration): (*1*) Schottky barrier; (*2*) hydrogenated layer; (*3*) *n*-GaAs layer; (*4*) n^+-GaAs layer; (*5*) ohmic contact; (*6*) semi-insulating GaAs substrate.

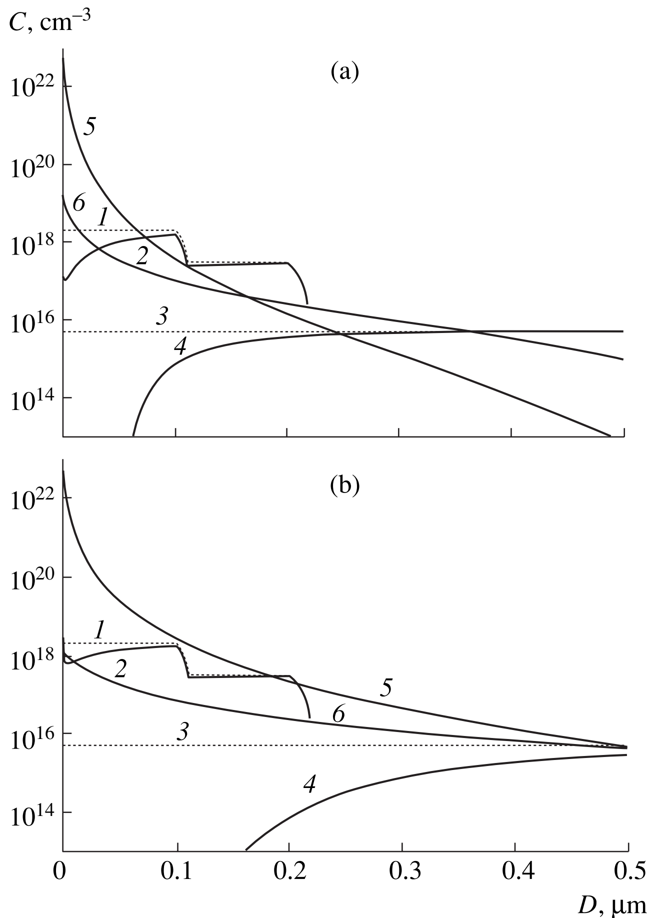

Fig. 2. Calculated depth–concentration profiles of the electrically active (*1*, *2*) shallow and (*3*, *4*) deep centers in GaAs structures (*1*, *3*) before and (*2*, *4*) after hydrogenation for (a) 5 min and (b) 40 min. Curves *5* and *6* show the profiles of atomic and molecular hydrogen, respectively, in the hydrogenated samples.

and the complexes of hydrogen with shallow and deep centers. In addition, allowance was made for a decrease in the probability of atomic hydrogen penetration into GaAs caused by a barrier of immobile interstitial hydrogen molecules formed in the subsurface layer.

Figure 2 shows the depth–concentration profiles of atomic and molecular hydrogen and the shallow and deep centers of the EL2 type in GaAs. After a 5-min hydrogenation, a significant passivation of EL2 centers takes place to a depth of 0.1–0.15 μm. The concentration of deep centers in the active *n*-GaAs layer decreases rather insignificantly, while that at the channel–substrate interface and in the semi-insulating GaAs substrate is unchanged. The treatment for t_h = 40 min results in hydrogen penetration to a greater depth, whereby the concentration of deep active centers significantly decreases both in the doped n^+–n layer and in the semi-insulating GaAs (down to a depth of 0.4 μm).

The results of experiments and calculations indicate that the increase in U_b is caused by the penetration of atomic hydrogen into the active *n*-GaAs layer and into deeper semi-insulating GaAs layers, leading to effective passivation of the active centers in these layers. A relatively low sink breakdown voltage (U_b = 11 V) observed in sample 3 upon prolonged hydrogenation (t_h = 200 min) is probably explained by the excess amount of hydrogen leading to the formation of new active defects. This suggestion is confirmed by the fact that only sample 3 exhibited a significant dependence of photoconductivity on the applied voltage. No such dependence was observed in the sample structures hydrogenated for a shorter time.

The conclusion that an increase in the electrical parameters of SBFETs is due to the passivation of defects inherent in ion-doped structures was confirmed in a special experiment. In this case, the test SBFETs and working microwave ICs fabricated using an analogous technology were based on n^+–n structures with a buffer layer of low-temperature GaAs grown by molecular beam epitaxy (MBE). The substrates were made of the same semi-insulating GaAs as that employed in the ion-doped structures described above. The high quality of epitaxial layers grown by MBE and the low concentration of defects in the samples provided for a sink breakdown voltage on the level of U_b = 16–18 V and a working power of 4 W. The hydrogenation of such epitaxial structures, conducted in various regimes, did not lead to a further increase in the SBFET parameters.

Thus, we found, for the first time, that the hydrogenation of ion-doped n^+–n GaAs structures leads to a more than twofold increase in the sink breakdown voltage of SBFETs and to a corresponding increase in the working power of related microwave ICs.

Acknowledgments. The authors are grateful to A.V. Golikov for measuring IC parameters and fruitful discussions and to L.M. Romas' for his help in conducting experiments.

REFERENCES

1. *GaAs FET Principles and Technology*, Ed. by J. V. DiLorenzo and D. D. Khandelwal (Artech House, Dedham, 1982; Radio i Svyaz', Moscow, 1988).
2. S. M. Myers, M. I. Baskes, H. K. Birnbaum, *et al.*, Rev. Mod. Phys. **64**, 559 (1992).
3. J. W. Corbett, S. J. Pearton, and M. Stavola, in *Defect Control in Semiconductors*, Ed. by K. Sumino (North-Holland, Amsterdam, 1990), pp. 53–63.
4. U. K. Chakrabarti, S. J. Pearton, W. S. Hobson, *et al.*, Appl. Phys. Lett. **57**, 887 (1990).
5. V. G. Bozhkov, V. A. Kagadeĭ, and N. A. Torkhov, Fiz. Tekh. Poluprovodn. (St. Petersburg) **32** (2), 1343 (1998) [Semiconductors **32**, 1196 (1998)].
6. V. A. Kagadeĭ, Yu. V. Lilenko, L. S. Shirokova, and D. I. Proskurovsky, Pis'ma Zh. Tekh. Fiz. **25** (13), 37 (1999) [Tech. Phys. Lett. **25**, 522 (1999)].
7. V. A. Kagadeĭ, Yu. V. Lilenko, L. S. Shirokova, and D. I. Proskurovsky, Pis'ma Zh. Tekh. Fiz. **26** (7), 1 (2000) [Tech. Phys. Lett. **26**, 269 (2000)].
8. V. A. Kagadei and D. I. Proskurovsky, J. Vac. Sci. Technol. A **16** (4), 2556 (1998).
9. É. M. Omel'yanovskiĭ, V. F. Pakhomov, and F. Ya. Polyakov, Fiz. Tekh. Poluprovodn. (Leningrad) **21** (5), 842 (1987) [Sov. Phys. Semicond. **21**, 514 (1987)].
10. R. Morrow, J. Appl. Phys. **66** (7), 2973 (1989).
11. N. S. Rytova, Fiz. Tekh. Poluprovodn. (Leningrad) **25** (6), 990 (1991) [Sov. Phys. Semicond. **25**, 598 (1991)].
12. N. S. Rytova, Fiz. Tekh. Poluprovodn. (Leningrad) **25** (6), 1078 (1991) [Sov. Phys. Semicond. **25**, 650 (1991)].
13. V. A. Kagadei, E. V. Nefyodtsev, and D. I. Proskurovsky, J. Vac. Sci. Technol. A **19** (4), 1871 (2001).

Translated by P. Pozdeev

Technical Physics Letters, Vol. 29, No. 1, 2003, pp. 16–18. Translated from Pis'ma v Zhurnal Tekhnicheskoĭ Fiziki, Vol. 29, No. 1, 2003, pp. 36–41.
Original Russian Text Copyright © 2003 by Dedkov, Kyasov.

The Fluctuational Electromagnetic Interaction of a Relativistic Particle with a Flat Surface

G. V. Dedkov and A. A. Kyasov

Kabardino-Balkarian State University, Nalchik, Kabardino-Balkaria, Russia

Received August 28, 2002

Abstract—General relationships between the fluctuational electromagnetic field energy, tangential force, and heating rate of a relativistic neutral particle moving near a flat surface are established for the first time. Within the framework of the fluctuational electrodynamics, closed expressions describing these quantities are obtained for arbitrary temperatures of the particle and the surface. © *2003 MAIK "Nauka/Interperiodica".*

The existing descriptions of the dissipative fluctuational electromagnetic interactions between neutral systems (see, e.g., [1–8]) still exhibit discrepancies. In our opinion, this is explained by the lack of clearly formulated relations between basic physical quantities involved in the problem, such as the fluctuational electromagnetic field energy, tangential force, heat exchange rate, spontaneous and induced components of the electric fields, currents, etc. The ambiguity results in essential differences in the character of theoretical schemes developed, leading eventually to principal discrepancies in results.

The purpose of this study was to establish general relativistic relationships between the aforementioned quantities and to calculate the values within the framework of a general method developed in our previous papers [7] for the case of a small neutral particle moving near a flat surface.

Consider a spherical nonmagnetic neutral particle possessing polarizability $\alpha(\omega)$ and moving in vacuum parallel to the flat boundary of a semi-infinite medium characterized by the dielectric permittivity $\varepsilon(\omega)$ and magnetic permeability $\mu(\omega)$. In the laboratory Cartesian coordinate system (L) fixed on the medium–vacuum interface, the particle moving with a velocity V at a distance z_0 from the surface induces the polarization $\mathbf{P}$ and magnetization $\mathbf{M}$ as described by the equations [9]

$$\mathbf{P}(\mathbf{r}, t) = \delta(x - Vt)\delta(y)\delta(z - z_0)\mathbf{d}(t), \qquad (1)$$

$$\mathbf{M}(\mathbf{r}, t) = \delta(x - Vt)\delta(y)\delta(z - z_0)\mathbf{m}(t), \qquad (2)$$

where $\mathbf{d} = (d'_x/\gamma, d'_y, d'_z)$ and $\mathbf{m} = (0, \beta d'_z, \beta d'_y)$ are the dipole and magnetic moments of the particle, respectively; $\gamma = (1 - \beta^2)^{-1/2}$; $\beta = V/c$; c is the speed of light; primed components of the fluctuational dipole moment $\mathbf{d}'$ refer to the particle rest system (R) in which $\mathbf{m}' = 0$.

Using formulas of the Lorentz transformation of the electric field strength ($\mathbf{E}$), current density ($\mathbf{j}$), and charge density (ρ) and taking into account a relation between the volume elements in the L and R frames of reference ($d\mathbf{r} = d\mathbf{r}'/\gamma$), we obtain a relationship between the statistical mean values of the work per unit time performed by the fluctuational electromagnetic field over the moving particle:

$$\int\langle\mathbf{jE}\rangle d\mathbf{r} = \gamma^{-2}\int\langle\mathbf{j}'\mathbf{E}'\rangle d\mathbf{r}' + F_x V, \qquad (3)$$

$$F_x = \int\langle\rho E_x\rangle d\mathbf{r} + \frac{1}{c}\int\langle[\mathbf{jH}]_x\rangle d\mathbf{r}', \qquad (4)$$

where F_x denotes the tangential force acting upon the moving particle in the L system. The charge and current densities are related to the polarization and magnetization vectors by the well-known relations

$$\rho = -\mathrm{div}\mathbf{P}, \quad \mathbf{j} = \partial\mathbf{P}/\partial t + c\,\mathrm{rot}\mathbf{M}. \qquad (5)$$

Using definitions of the quantities involved in Eq. (3) and carrying out the transformations, we arrive at the relationship

$$\int\langle\mathbf{jE}\rangle d\mathbf{r} = F_x V + \langle\dot{\mathbf{d}}\mathbf{E}\rangle - \beta\langle[\dot{\mathbf{d}}\mathbf{H}]_x\rangle, \qquad (6)$$

from which it follows that the value

$$\dot{Q} = \langle\dot{\mathbf{d}}\mathbf{E}\rangle - \beta\langle[\dot{\mathbf{d}}\mathbf{H}]_x\rangle \qquad (7)$$

should be treated as the rate of heating of the moving particle as a result of its interaction with the fluctuational electromagnetic field in the L system. Previously, we obtained the formula $\dot{Q} = \langle\dot{\mathbf{d}}\mathbf{E}\rangle$ in the nonrelativistic case [10]. Using the above definitions of vectors $\mathbf{d}$ and $\mathbf{m}$, we can write Eq. (7) in a more compact form as

$$\dot{Q} = \langle\dot{\mathbf{d}}\mathbf{E} + \dot{\mathbf{m}}\mathbf{H}\rangle. \qquad (8)$$

By the same token, Eq. (4) reduces, with account taken of Eqs. (1), (2), and (5), to

$$F_x = \langle\nabla_x(\mathbf{dE} + \mathbf{mH})\rangle. \qquad (9)$$

The normal force component F_z for the particle–surface interaction is obtained by substituting $x \longrightarrow z$ in for-

mula (9) (note that the substitution of coordinates has to be performed upon completing the operation of differentiation).

Using methods of the general theory of electromagnetic fluctuations [11] for calculating the correlators in Eqs. (8) and (9), we obtained the following closed relativistic expressions for F_x, F_z, and $\dot{Q}$ (with T_1 and T_2 denoting the temperatures of the particle and surface, respectively):

$$F_x = -\frac{\hbar}{\pi^2}\gamma\iiint d\omega dk_x dk_y k_x$$
$$\times\Bigg\{\alpha''(\omega\gamma)\coth\frac{\hbar\omega\gamma}{2k_BT_1}\Bigg(\frac{\exp(-2q_0^{(+)}z_0)}{q_0^{(+)}}[\Psi_e^{(+)}(\omega,\mathbf{k})\Delta_e''(\omega+k_xV)+\Psi_m^{(+)}(\omega,\mathbf{k})\Delta_m''(\omega+k_xV)]$$
$$-\frac{\exp(-2q_0^{(-)}z_0)}{q_0^{(-)}}[\Psi_e^{(-)}(\omega,\mathbf{k})\Delta_e''(\omega+k_xV)+\Psi_m^{(-)}(\omega,\mathbf{k})\Delta_m''(\omega-k_xV)]\Bigg)$$
$$+\coth\frac{\hbar\omega}{2k_BT_2}\frac{\exp(-2q_0z_0)}{q_0}(\alpha''((\omega+k_xV)\gamma)[\chi_e^{(+)}(\omega,\mathbf{k})\Delta_e''(\omega)+\chi_m^{(+)}(\omega,\mathbf{k})\Delta_m''(\omega)]$$
$$-\alpha''((\omega-k_xV)\gamma)[\chi_e^{(-)}(\omega,\mathbf{k})\Delta_e''(\omega)+\chi_m^{(-)}(\omega,\mathbf{k})\Delta_m''(\omega)])\Bigg\}, \quad (10)$$

$$F_z = -\frac{\hbar}{\pi^2}\gamma\iiint d\omega dk_x dk_y$$
$$\times\Bigg\{\alpha''(\omega\gamma)\coth\frac{\hbar\omega\gamma}{2k_BT_1}(\exp(-2q_0^{(+)}z_0)[\Psi_e^{(+)}(\omega,\mathbf{k})\Delta_e'(\omega+k_xV)+\Psi_m^{(+)}(\omega,\mathbf{k})\Delta_m'(\omega+k_xV)]$$
$$+\exp(-2q_0^{(-)}z_0)[\Psi_e^{(-)}(\omega,\mathbf{k})\Delta_e'(\omega+k_xV)+\Psi_m^{(-)}(\omega,\mathbf{k})\Delta_m'(\omega-k_xV)])$$
$$+\coth\frac{\hbar\omega}{2k_BT_2}\exp(-2q_0z_0)(\alpha'((\omega+k_xV)\gamma)[\chi_e^{(+)}(\omega,\mathbf{k})\Delta_e''(\omega)+\chi_m^{(+)}(\omega,\mathbf{k})\Delta_m''(\omega)]$$
$$+\alpha'((\omega-k_xV)\gamma)[\chi_e^{(-)}(\omega,\mathbf{k})\Delta_e''(\omega)+\chi_m^{(-)}(\omega,\mathbf{k})\Delta_m''(\omega)])\Bigg\}, \quad (11)$$

$$\dot{Q} = -\frac{\hbar}{\pi^2}\gamma\iiint d\omega dk_x dk_y\Bigg\{\alpha''(\omega\gamma)\coth\frac{\hbar\omega\gamma}{2k_BT_1}\Bigg(\frac{\exp(-2q_0^{(+)}z_0)}{q_0^{(+)}}$$
$$\times\omega[\Psi_e^{(+)}(\omega,\mathbf{k})\Delta_e''(\omega+k_xV)+\Psi_m^{(+)}(\omega,\mathbf{k})\Delta_m''(\omega+k_xV)]$$
$$+\frac{\exp(-2q_0^{(-)}z_0)}{q_0^{(-)}}[\Psi_e^{(-)}(\omega,\mathbf{k})\Delta_e''(\omega+k_xV)+\Psi_m^{(-)}(\omega,\mathbf{k})\Delta_m''(\omega-k_xV)]\Bigg) \quad (12)$$
$$-\coth\frac{\hbar\omega}{2k_BT_2}\frac{\exp(-2q_0z_0)}{q_0}(\alpha''((\omega+k_xV)\gamma)(\omega+k_xV)[\chi_e^{(+)}(\omega,\mathbf{k})\Delta_e''(\omega)+\chi_m^{(+)}(\omega,\mathbf{k})\Delta_m''(\omega)]$$
$$+\alpha''((\omega-k_xV)\gamma)(\omega-k_xV)[\chi_e^{(-)}(\omega,\mathbf{k})\Delta_e''(\omega)+\chi_m^{(-)}(\omega,\mathbf{k})\Delta_m''(\omega)])\Bigg\},$$

where

$$q_0 = (k^2 - \omega^2/c^2)^{1/2}, \ q_0^{(\pm)} = \sqrt{k^2 - (\omega \pm k_x V)^2/c^2}, \quad (13)$$

$$\Psi_e^{(\pm)}(\omega, \mathbf{k}) = 2(k^2 - k_x^2\beta^2) \times (1 - (\omega \pm k_x V)^2/k^2c^2) + \omega^2/c^2, \quad (14)$$

$$\Psi_m^{(\pm)}(\omega, \mathbf{k}) = 2k_y^2\beta^2(1 - (\omega \pm k_x V)^2/k^2c^2) + \omega^2/c^2, \quad (15)$$

$$\chi_e^{(\pm)}(\omega, \mathbf{k}) = 2(k^2 - k_x^2\beta^2)(1 - \omega^2/k^2c^2) + \frac{(\omega \pm k_x V)^2}{c^2}, \quad (16)$$

$$\chi_m^{(\pm)}(\omega, \mathbf{k}) = 2k_y^2\beta^2(1 - \omega^2/k^2c^2) + \frac{(\omega \pm k_x V)^2}{c^2}, \quad (17)$$

$$\Delta_m(\omega) = \left(\frac{\mu(\omega)q_0 - q}{\mu(\omega)q_0 + q}\right), \quad (18)$$

$$\Delta_e(\omega) = \left(\frac{\varepsilon(\omega)q_0 - q}{\varepsilon(\omega)q_0 + q}\right). \quad (19)$$

Here, single and double primes denote real and imaginary components of the corresponding quantities; integration with respect to the two-dimensional wavevector element $d\mathbf{k} = dk_x dk_y$ is performed over positive wavevector projections k_x and k_y obeying the condition $k = \sqrt{k_x^2 + k_y^2} > \omega/c$ for nonradiative modes of the fluctuational electromagnetic field, while integration with respect to frequency is performed in the interval $(0, \infty)$. In Eqs. (10)–(12), the contribution from radiative modes ($\omega > ck$) is omitted: this contribution is significant at very large distances z_0 and tends to zero in the nonrelativistic limit as $c \longrightarrow \infty$.

In the nonrelativistic limit ($c \longrightarrow \infty$), formula (10) for the tangential force simplifies to [10]

$$F_x = \frac{-2\hbar}{\pi^2}\iiint d\omega d\mathbf{k} k_x k \exp(-2kz_0) \times \left\{\alpha''(\omega)\coth\frac{\hbar\omega}{2k_B T_1}[\Delta''(\omega + k_x V) - \Delta''(\omega - k_x V)] + \Delta''(\omega)\coth\frac{\hbar\omega}{2k_B T_2}[\alpha''(\omega + k_x V) - \alpha''(\omega - k_x V)]\right\}, \quad (20)$$

where $\Delta(\omega) = (\varepsilon(\omega) - 1)/(\varepsilon(\omega) + 1)$. For the particular case of $T_1 = T_2 = T$ in the linear approximation with respect to velocity, Eq. (20) reduces to a formula coinciding with the result obtained by Tomassone and Widom [4]. It also follows from Eq. (20) that a linear (with respect to the particle velocity) relativistic correction to F_x, not containing the derivatives of $\alpha''(\omega)$ and $\Delta''(\omega)$, can be written as

$$\delta F_x = -\frac{1}{c^2}\frac{\hbar V}{2\pi z_0^3}\int_0^\infty d\omega\omega\alpha''(\omega)\Delta''(\omega) \times \left[\coth\frac{\hbar\omega}{2k_B T_1} + \coth\frac{\hbar\omega}{2k_B T_2}\right]. \quad (21)$$

In the case of $T_1 = T_2 = T$, this formula resembles the result of Dorofeev *et al.* [8] (where a somewhat different dependence on the distance was obtained, $F_x \propto z_0^{-4}$). Finally, formula (12) for the particle heating rate $\dot{Q}$ at $V = 0$ agrees with the results reported in [12, 13].

Thus, using a formalism of the theory of electromagnetic fluctuations, we performed, for the first time, the quantum-statistical averaging of the operators of a dipole force acting upon a neutral relativistic particle and determined the rate of particle heating during interaction with a fluctuational electromagnetic field at the surface.

REFERENCES

1. L. S. Levitov, Europhys. Lett. **8**, 489 (1989).
2. V. G. Polevoĭ, Zh. Éksp. Teor. Fiz. **98** (6), 1990 (1990) [Sov. Phys. JETP **71**, 1119 (1990)].
3. V. E. Mkrtchian, Phys. Lett. A **207**, 299 (1995).
4. M. S. Tomassone and A. Widom, Phys. Rev. B **56**, 4938 (1997).
5. J. B. Pendry, J. Phys.: Condens. Matter **9**, 10301 (1997).
6. A. I. Volokitin and B. N. J. Persson, J. Phys.: Condens. Matter **11**, 345 (1999).
7. G. V. Dedkov and A. A. Kyasov, Phys. Lett. A **259**, 38 (1999); Surf. Sci. **463**, 11 (2000); Fiz. Tverd. Tela (St. Petersburg) **43** (1), 169 (2001) [Phys. Solid State **43**, 176 (2001)].
8. I. Dorofeyev, H. Fuchs, B. Gotsmann, and J. Jersch, Phys. Rev. B **64**, 035403 (2001).
9. A. A. Kyasov, Pis'ma Zh. Tekh. Fiz. **28** (2), 56 (2002) [Tech. Phys. Lett. **28**, 64 (2002)].
10. G. V. Dedkov and A. A. Kyasov, Pis'ma Zh. Tekh. Fiz. **28** (8), 79 (2002) [Tech. Phys. Lett. **28**, 346 (2002)].
11. E. M. Lifshitz and L. P. Pitaevskiĭ, *Course of Theoretical Physics*, Vol. 5: *Statistical Physics* (Nauka, Moscow, 1978; Pergamon, New York, 1980), Part 2.
12. J. B. Pendry, J. Phys.: Condens. Matter **11**, 6621 (1999).
13. A. I. Volokitin and B. N. J. Persson, Phys. Rev. B **63**, 205404 (2001).

Translated by P. Pozdeev

Technical Physics Letters, Vol. 29, No. 1, 2003, pp. 19–21. Translated from Pis'ma v Zhurnal Tekhnicheskoĭ Fiziki, Vol. 29, No. 1, 2003, pp. 42–46.
Original Russian Text Copyright © 2003 by Malafaev.

On the Nature of Bond Bending in Water

N. T. Malafaev

Kharkov State Academy of Food Technology and Organization, Kharkov, Ukraine

e-mail: hdatoh@kharkov.com

Received July 23, 2002

Abstract—It is shown that the theory of the Jahn–Teller pseudoeffect provides physical ground for the hydrogen bond bending postulated by Popl (this hypothesis underlies the continuum model of water) and explains the anomalous properties of water. *© 2003 MAIK "Nauka/Interperiodica".*

Water is widely used in various technologies as a solvent. However, by no means all properties of this anomalous liquid are completely clear. Below, it is shown that the hydrogen bond bending in water, which was postulated by Popl [1] and served as a basis for the modern continuum model of water, can be explained within the framework of the theory of the Jahn–Teller pseudoeffect. For this purpose, we will analyze the mechanism of interactions between neighboring water molecules and consider the physical consequences of these interactions.

Each molecule of water possesses four hybrid orbitals arranged at angles close to tetrahedral. Two of these orbitals bind protons of the given molecule, while the other two interact with protons of the neighboring molecules, thus entering into a network of hydrogen bonds existing in water [1, 2]. The binding of neighboring molecules, despite the aforementioned bond bending, is quite strong due to large uncompensated charges on the electron shells (orbitals) of oxygen and hydrogen atoms. For this reason, the tetrahedral structure in the arrangement of water molecules is retained in the entire temperature range of existence of this compound (from 0 to 374°C). The neighboring molecules perform thousands of vibrations between the events of bond breakage. The properties of such a pair of bound molecules, called a dimer (Fig. 1), have been studied in sufficient detail [3]. The force of attraction in a dimer is analogous to the surface tension (caused by the same interaction) and must linearly decrease on heating to reach zero at a critical point. However, the presence of other competitive interactions leads to certain peculiarities of the hydrogen bonds linking the molecules.

Let us consider in more detail the electrostatic and exchange interactions between overlapping electron orbitals of two oxygen atoms O_1 and O_2 (Fig. 1). Since the contribution of the exchange interaction is usually small (not exceeding 20%) [4], we will assume the electrostatic interaction to be dominating. This interaction between orbitals of neighboring molecules gives rise to their mutual repulsion. Indeed, a decrease in the temperature of water is accompanied by a number of anomalies such as thermal expansion, viscosity, a growth in its volume upon freezing, etc. [2]. Thus, the interactions between overlapping electron orbitals in a water dimer exhibit a "repulsive" character and must lead to instability of the linear configuration of hydrogen bonds (i.e., of the O_1–H–O_2 system depicted in Fig. 1a). In connection with this, an analysis of interactions between water molecules has to be performed within the framework of the theory of the Jahn–Teller effect which is capable of describing such systems of molecules and crystals [5].

The existing theory of the Jahn–Teller effect is based on the concept of short-range order and, hence, is also applicable to molecules in liquids. The presence of a proton on the O_1–O_2 line (the axis of a dimer) significantly complicates description of the system. However, the neighboring electronegative atoms O_1 and O_2 (and their orbitals involved in hydrogen bonding) closely approach each other without any significant decrease in the magnitude of interaction. In the static (low-temperature) case of the Jahn–Teller effect, the vibrational energy is insufficient for the system to escape from the potential energy minimum. This implies that the system is stable and the hydrogen bonds are linear, which corresponds to the state of ice (Fig. 1a; for explanation, see below). As the vibrational

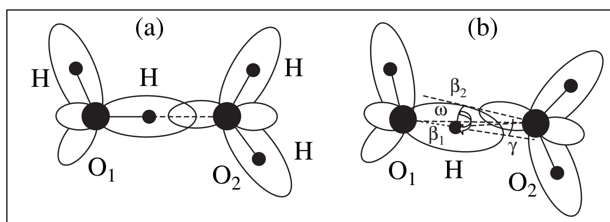

Fig. 1. Schematic diagrams illustrating the interaction between neighboring water molecules and orientation of the electron orbitals of oxygen atoms in (a) ice and (b) liquid water.

1063-7850/03/2901-0019$24.00 © 2003 MAIK "Nauka/Interperiodica"

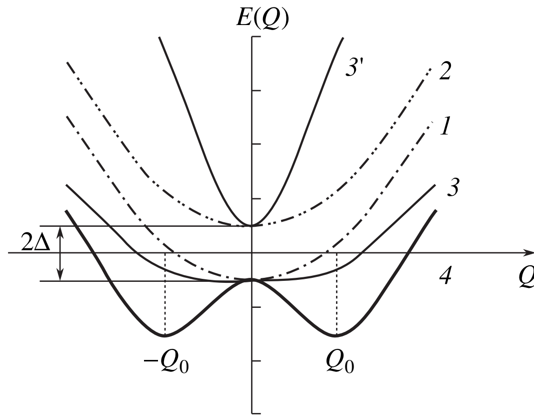

Fig. 2. Adiabatic potentials of two electron terms (*1*, *2*) and the results of their mixing due to a common singlet oscillation in the case of (*3*, *3*') weak and (*4*) strong Jahn–Teller pseudoeffect [6].

energy of atoms increases with the temperature, some transverse bending modes become energetically favorable and the systems melts, passing into a new electron-vibrational state in which the hydrogen bond angles γ exhibit bending (Fig. 1b). Since the protons of a given molecule possess thermal energy due to interaction with other molecules, the molecule features vibrational-rotational motions (in particular, around the O_1–O_2 dimer axis) at a certain frequency ω. As a result, there arise centrifugal forces favoring stabilization of the bond bending angles γ in the course of such rotation. The appearance of new rotational degrees of freedom for the protons of water probably accounts for an almost twofold increase in the heat capacity of water in the liquid state as compared to that in the solid (ice) or vapor states. Note also that, among all substances, water has the maximum value of heat capacity.

According to existing theory, the above case of a linear quasi-molecule (a dimer composed of two pseudo-degenerate water molecules) is classified as the Jahn–Teller pseudoeffect (or the Renner effect). For a weak Jahn–Teller pseudoeffect, the molecule remains linear, while a strong pseudoeffect is accompanied by bending of the molecule (or bond) characterized by the deformation [5]

$$\pm Q_0 = \sqrt{F^2/K^2 - \Delta^2/F^2}, \qquad (1)$$

where K is the elastic constant, F is the vibronic constant, and 2Δ is the energy gap between states (the formula is valid for $\Delta < F^2/K$). A decrease in the binding forces and the elastic constant upon melting leads to the appearance of minima in the adiabatic potential $E(Q)$ at the transverse (angular) deformation of $\pm Q_0$ (Fig. 2, curve *4*). For a first approximation, the adiabatic potential has the shape of a circular groove with a depth of

$$E_{\text{JT}} = (F^2/2K) + (\Delta^2 K/F^2) - \Delta. \qquad (2)$$

Therefore, water exhibits a dynamically stable electron configuration in which the rotation of molecules and protons around the dimer axes is a collective motion involving all water molecules. This collective motion is described as the electron-vibrational motion in the groove of an adiabatic potential surface having the shape of a "mexican hat" (with curve *4* in Fig. 2 representing a cross-section of this potential surface).

Bound oscillations of the electron subsystem (orbitals) and the nuclear subsystem (nuclei of atoms and molecules) lead to a decrease in the average magnitude of interactions. For the dynamic Jahn–Teller effect, this decrease is described in terms of the Ham vibronic reduction factors η^* [5]. In the case of nondiagonal (shear) interactions, these factors are calculated by the formula

$$\eta^* = E/E_0 = \exp\left(-\frac{3E_{\text{JT}}}{\hbar\omega}\right), \qquad (3)$$

where E and E_0 are the energies of nondiagonal interactions in the dynamic and static states, respectively; E_{JT} is the energy of minimum of the Jahn–Teller potential (2) (curve *4* in Fig. 2); and ω is the frequency of oscillations of the collective deformation modes (proton rotations). For the diagonal interactions, a decrease in the static interaction component E_0 amounts to about 50%, while the dynamic component is described by an expression of type (3). Thus, in the presence of vibronic reduction, the intermolecular interaction energy contains a contribution which exponentially decays with decreasing temperature. This is accompanied by the anomalous variation of all related properties, as was observed for water in the temperature interval from 0 to 80°C [6, 7].

Conclusions: (i) An allowance for the electron-vibrational interactions within the framework of the theory of the Jahn–Teller pseudoeffect explains hydrogen bond bending in water, which was postulated by Popl [1] and served as a basis for the modern continuum model of water. (ii) The dynamic state of water molecules in the liquid phase leads to the vibronic reduction of intermolecular interactions as described by the Ham factors, which explains the anomalous variation of the properties of liquid water.

Acknowledgments. The author is grateful to B.G. Emets for fruitful discussions and support.

REFERENCES

1. J. A. Popl, Proc. R. Soc. London, Ser. A **205**, 163 (1951).
2. G. N. Zatsepina, *Physical Properties and Structure of Water* (Mosk. Gos. Univ., Moscow, 1987, 2nd ed.).
3. V. Ya. Antonchenko, A. S. Davydov, and V. V. Il'in, *Foundations of Physics of Water* (Naukova Dumka, Kiev, 1991).
4. R. M. Minyaev and G. V. Orlova, Zh. Strukt. Khim. **26** (2), 13 (1985).
5. I. B. Bersuker, *The Jahn–Teller Effect and Vibronic Interactions in Modern Chemistry* (Nauka, Moscow, 1987; Plenum, New York, 1984).
6. N. T. Malafaev, in *Collection of Scientific Works of the Kharkov State Academy of Food Technology and Organization* (in Two Volumes) (Khark. Derzh. Akad. Tekhnol. Org. Kharchuvannya, Kharkov, 1998), Vol. 2, pp. 81–84.
7. N. T. Malafaev, in *Collection of Scientific Works of the Kharkov State Academy of Food Technology and Organization* (in Two Volumes) (Khark. Derzh. Akad. Tekhnol. Org. Kharchuvannya, Kharkov, 2000), Vol. 2, pp. 246–251.

Translated by P. Pozdeev

Technical Physics Letters, Vol. 29, No. 1, 2003, pp. 22–25. Translated from Pis'ma v Zhurnal Tekhnicheskoĭ Fiziki, Vol. 29, No. 1, 2003, pp. 47–55.
Original Russian Text Copyright © 2003 by Boltovets, Zorenko, Ivanov, Vlaskina, Konakova, Kudrik, P. Litvin, O. Litvin, Milenin, Abdizhaliev.

Peculiarities of the Formation and Thermal Stability of Barrier Contacts in High-Sensitivity Silicon Carbide Detector Diodes

N. S. Boltovets, A. V. Zorenko, V. N. Ivanov, S. I. Vlaskina, R. V. Konakova, Ya. Ya. Kudrik, P. M. Litvin, O. S. Litvin, V. V. Milenin, and S. K. Abdizhaliev

"Orion" State Research Institute, Kiev, Ukraine

Institute of Semiconductor Physics, National Academy of Sciences of Ukraine, Kiev, Ukraine

e-mail: konakova@isp.kiev.ua

Received August 19, 2002

Abstract—The effect of rapid thermal treatment at $T = 1000°C$ on the formation of TiB_x–n-SiC6H($000\bar{1}$) barrier contacts and Ni–n-SiC6H(0001) ohmic contacts was studied. In the former case, thermal treatment neither disturbs the layer structure nor reduces the thermal stability of the barrier contacts. The rapid annealing of an Ni–n-SiC6H(0001) structure results in the formation of a stable ohmic contact. At the same time, this treatment does not change the parameters of the static current–voltage characteristics of the Au–TiB_x–n-SiC6H($000\bar{1}$) Schottky diodes. These thermally stable diodes are characterized by a sensitivity of ~3300–3500 mV/mW at an incident radiation power of 10^{-7} W and are capable of operating at a microwave power of up to 1 W. The dynamic range of a linear portion of the conversion characteristic reaches up to 50 dB. © *2003 MAIK "Nauka/Interperiodica".*

Successful development of high-temperature solid-state electronic devices, the base material of which is silicon carbide, depends not only on the quality of the initial semiconductor but, to a considerable extent, on the properties of the ohmic and barrier contacts [1–5]. This is especially true for microwave Schottky barrier diodes, where the thermal stability of such contacts becomes a very significant factor at high input power levels. Since the quality and reliability of both discrete semiconductor devices and integrated circuits are determined by the physicochemical and structural properties of a transition layer formed in the metal–semiconductor junction [6, 7], it is still important to search for contact materials ensuring a minimum thickness of the transition layer or that do not interact at all with the semiconductor up to a temperature significantly above the working range [8–10].

The results of investigations of the contacts to silicon and gallium arsenide [11–15] showed that the above requirements are satisfied by the amorphous and quasiamorphous films of titanium nitrides and borides. Such films are characterized by chemical inertness and low diffusion permeability in combination with high electric conductivity. These factors are especially important for the barrier contacts to silicon carbide, which have to provide for the realization of the unique high-temperature properties of this semiconductor. In accordance with this, there has been an active search for the best contacts to SiC in recent years, predominantly among carbides, tungstates, and nitrides of refractory metals. We have attempted to obtain such barrier contacts, made of TiB_x, for a silicon-carbide-based Schottky barrier detector diode.

The experiments were performed with TiB_x–n-SiC6H($000\bar{1}$) barrier contacts obtained by magnetron sputtering of a stoichiometric target onto a preliminarily cleaned single crystal n-SiC (6H polytype) substrate with a donor concentration of $\sim 1 \times 10^{18}$ cm^{-3}, grown by the Lely method. The ohmic contacts were prepared by the magnetron sputtering of nickel, followed by fusion in vacuum (1.33×10^{-4} Pa) at 1000°C for 2 min. The contacts for microwelding were formed, with the aid of microelectronic techniques, by microgalvanic gold deposition after rapid thermal treatment.

We studied samples of two types: test structures and Schottky barrier diodes. Samples of the former type represented TiB_x–n-SiC6H($000\bar{1}$) and Ni–n-SiC6H(0001) structures with an ~800-Å-thick TiB_x layer deposited onto the ($000\bar{1}$)SiC crystal face and an ~1000-Å-thick Ni layer, onto the SiC(0001) face. The opposite crystal face was not subjected to metallization. Schottky barrier diode structures with a diameter of 20 and 100 μm were formed in windows preliminarily etched in an SiO_2 layer. Finally, the wafers were cut into chips and the latter were mounted in microwave diode cases.

1063-7850/03/2901-0022$24.00 © 2003 MAIK "Nauka/Interperiodica"

Samples of both types, representing test and device structures on the wafers, were subjected to rapid thermal treatment consisting of annealing at $T = 1000°C$ for 90 s in a vacuum of 1.33×10^{-4} Pa. Before and after this treatment, the depth–composition profiles of elements in the TiB_x–n-SiC6H$(000\bar{1})$ and Ni–n-SiC6H(0001) test structures were determined using Auger electron spectroscopy in combination with layer-by-layer removal by ion etching. In addition, the surface morphology of the TiB_x and Ni films was studied by atomic force microscopy (AFM), and the phase compositions of the barrier and ohmic contacts, by X-ray diffraction.

Direct branches of the current–voltage (I–U) and capacitance–voltage (C–U) characteristics of the Schottky diode structures on the wafer and in the cases were also measured before and after the rapid thermal treatment. The conversion characteristics were measured for the diodes connected to a hybrid-integral detector scheme. The measuring circuit was based on nonsymmetric strip lines with a wave impedance of 50 Ω. The measurements were performed using various bias currents (0–13.8 μA) at a frequency of 300 MHz.

The direct branch of a typical I–U characteristic of the Au–TiB_x–n-SiC6H$(000\bar{1})$ Schottky barrier diode before and after the rapid thermal treatment at T = 1000°C can be described by the formula

$$I = I_s \exp\left(\frac{eV}{nkT} - 1\right),$$

where $I_s = A^* T^2 S \exp(-\varphi_b/kT)$, I_s is the saturation current, $A^* = 194$ A/(cm^2 K^2) is the effective Richardson constant for n-SiC6H, S is the diode area, T is the absolute temperature, e is the electron charge, k is the Boltzmann constant, φ_b is the Schottky barrier height, n is the ideality factor, and V is the applied voltage.

After the rapid thermal treatment, the Schottky barrier parameters did not show a significant change. In the initial state, the barrier height was $\varphi_b = 0.69$ eV and the ideality factor was $n = 1.5$; in the final state, the corresponding values were $\varphi_b = 0.69$ eV and $n \approx 1.6$. Estimates of the barrier height obtained from the cutoff voltage determined using the C–U characteristic plotted as $1/C^2 = f(U)$ also showed that φ_b was virtually unchanged after the thermal treatment and amounted to ~0.7 eV. This fact is indicative of the thermal stability of both the interphase boundary in the contact between TiB_x and n-SiC and the transition layer composition.

The results of investigation of the conversion characteristics of the detector diodes are illustrated in Fig. 1. Below the input power of 10 μW, the characteristic is close to quadratic. The transition from quadratic to quasilinear behavior was observed at an input power of ~10 μW. In the quadratic portion of the characteristic, the detector diodes under consideration exhibited maximum sensitivity for a direct current from 0.5 to 3 μA. The bias currents in these diodes are one order of

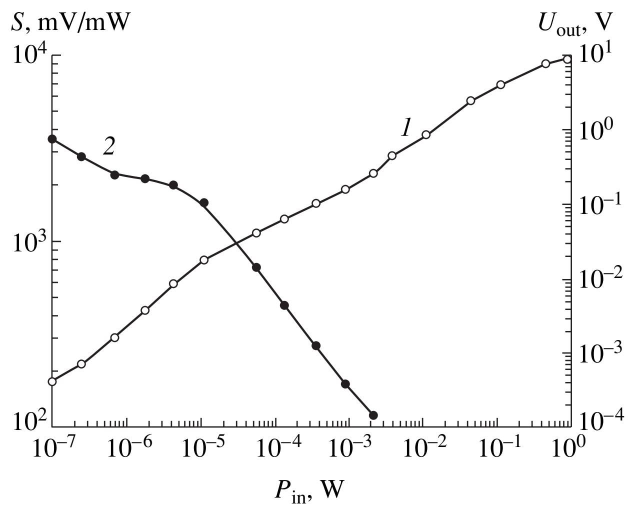

Fig. 1. The plots of (*1*) diode output voltage U_{out} and (*2*) sensitivity S versus the input microwave power P_{in} at a bias current of 3.2 μA.

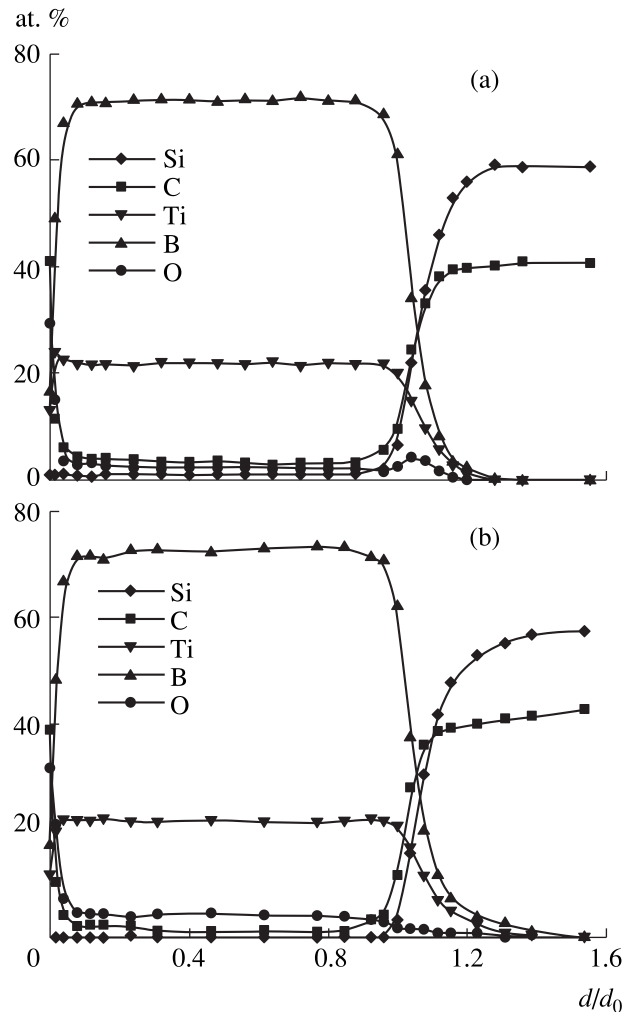

Fig. 2. Elemental depth–composition profiles of a TiB_x–n-SiC6H$(000\bar{1})$ barrier contact (a) before and (b) after rapid thermal annealing at 1000°C.

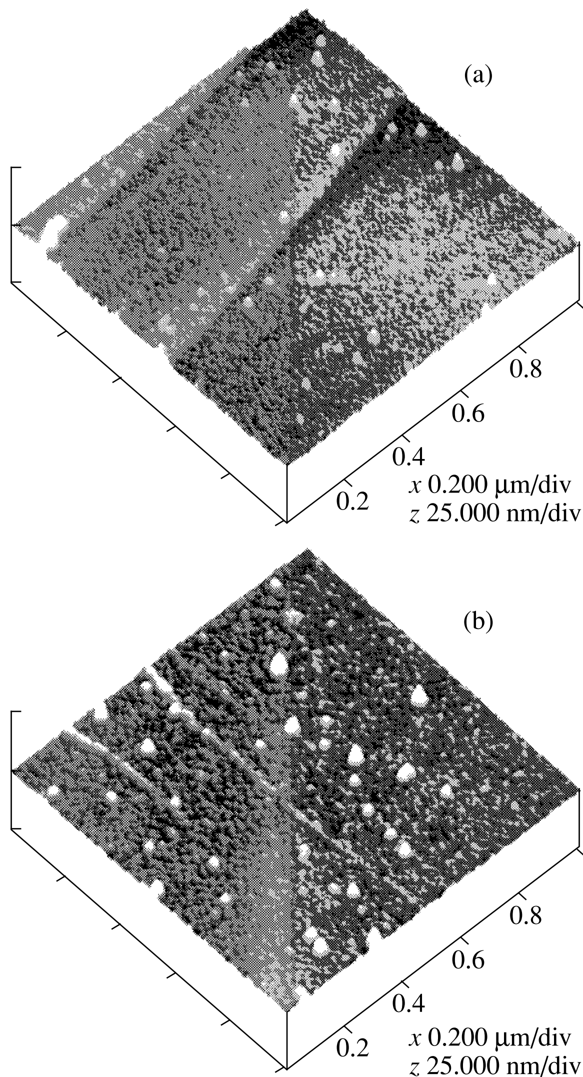

Fig. 3. AFM images showing the surface morphology of a TiB_x–n-SiC6H($000\bar{1}$) barrier contact (a) before and (b) after rapid thermal annealing at 1000°C.

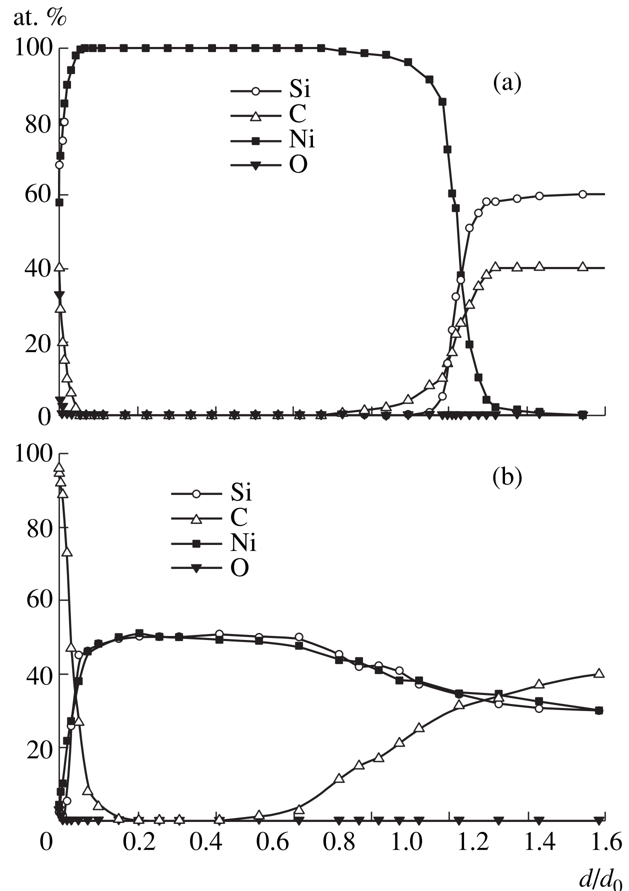

Fig. 4. Elemental depth–composition profiles of an Ni–n-SiC6H(0001) contact (a) before and (b) after rapid thermal annealing at 1000°C.

magnitude lower as compared to analogous values in GaAs-based Schottky diodes.

According to Fig. 1, a special feature of the silicon-carbide-based Schottky barrier detector diodes is the possibility of operating at an input power of up to 1 W. The dynamic range of a linear portion of the conversion characteristic reaches up to 50 dB. The diode sensitivity (with respect to the output voltage) in this region weakly depends on the bias current and decreases with increasing power. The aforementioned dynamic characteristics of the TiB_x–n-SiC6H($000\bar{1}$) Schottky barrier diodes were obtained due to stability of the thermal properties and composition of the interphase boundary in the barrier contact. Indeed, the X-ray diffraction data showed that the initial TiB_x film occurs in a quasiamorphous state and the rapid thermal treatment at 1000°C does not change the phase composition.

These results agree with the AES data presented in Fig. 2, which show no evidence of an annealing-induced increase in the chemical interaction between the TiB_x film and SiC substrate. Both thickness (~200 Å) and composition of the transition layer after rapid thermal annealing are the same as before the treatment, which confirms the conclusion concerning thermal stability of the barrier contact as drawn from an analysis of the *I*–*U* and *C*–*U* curves. Small changes in these characteristics can be attributed to changes in the surface morphology of TiB_x.

As can be seen from the AFM image in Fig. 3, rapid annealing did not significantly change the surface roughness of TiB_x film (which is ~0.5 nm both before and after the treatment). However, the annealed sample surface displays nanoislands of greater density and dimensions (4.0 nm in height and 45.0 nm in diameter in the initial state versus 7.0 and 50.0 nm, respectively, in the annealed state). In addition, the thermal treatment stimulates a certain organization, whereby the small-sized nanoislands form chains that may be evidence of

a redistribution of the fields of mechanical stresses in the TiB_x film.

The nickel film in the Ni–*n*-SiC6H(0001) contact structures in the initial state represents a polycrystalline metal phase. The ohmic contact is formed as a result of rapid thermal treatment. The phase transformations of nickel induced by the thermal treatment result in that the pure nickel phase disappears and the proportion of nickel silicides grows to an amount which is not changed by repeated thermal treatment at 1000°C. Figure 4 shows the elemental depth profiles of the ohmic contact before and after rapid thermal treatment.

Thus, using a quasiamorphous TiB_x alloy as a barrier contact to *n*-SiC6H($000\bar{1}$) and a nickel-silicide-based ohmic contact to the SiC substrate, it is possible to obtain highly sensitive and thermally stable detector diodes that offer good prospects for use in microwave power measurements.

REFERENCES

1. P. A. Ivanov and V. E. Chelnokov, Fiz. Tekh. Poluprovodn. (St. Petersburg) **29** (11), 1921 (1995) [Semiconductors **29**, 1003 (1995)].
2. A. A. Lebedev and V. E. Chelnokov, Fiz. Tekh. Poluprovodn. (St. Petersburg) **33** (9), 1096 (1999) [Semiconductors **33**, 999 (1999)].
3. S. Yu. Davydov, A. A. Lebedev, and S. K. Tikhonov, Fiz. Tekh. Poluprovodn. (St. Petersburg) **31** (5), 597 (1997) [Semiconductors **31**, 506 (1997)].
4. D. Defiver, O. Durand, F. Wyczisk, *et al.*, Microelectron. Eng. **55** (3), 369 (2001).
5. B. Precz, Appl. Surf. Sci. **153** (1), 1 (2001).
6. V. F. Dorfman, *Micrometallurgy in Microelectronics: Principles of Technology in Semiconductor Device Manufacturing Industry* (Metallurgiya, Moscow, 1978).
7. S. P. Murarka, *Silicides for VLSI Application* (Academic, New York, 1983).
8. F. Via La, F. Roccaforte, A. Makhtari, *et al.*, Microelectron. Eng. **60**, 269 (2002).
9. S. Hara, Surf. Sci. **494**, L805 (2001).
10. Sang Youn Han, Ki Hong Kim, Jong Kyn Kim, *et al.*, Appl. Phys. Lett. **79** (12), 1816 (2001).
11. E. F. Venger, V. V. Milenin, I. B. Ermolovich, *et al.*, Fiz. Tekh. Poluprovodn. (St. Petersburg) **33** (8), 948 (1999) [Semiconductors **33**, 865 (1999)].
12. V. V. Milenin and R. V. Konakova, Pis'ma Zh. Tekh. Fiz. **27** (14), 30 (2001) [Tech. Phys. Lett. **27**, 586 (2001)].
13. N. S. Boltovets, N. M. Goncharuk, V. A. Krivutsa, *et al.*, Semicond. Phys., Quantum Electron. Optoelectron. **3** (3), 352 (2000).
14. S. K. Lee, C. M. Zetterling, and M. Ostling, J. Appl. Phys. **87** (11), 8039 (2000).
15. L. M. Porter and R. F. Gavis, Mater. Sci. Eng. B **34** (1), 83 (1995).

Translated by P. Pozdeev

Technical Physics Letters, Vol. 29, No. 1, 2003, pp. 26–28. Translated from Pis'ma v Zhurnal Tekhnicheskoĭ Fiziki, Vol. 29, No. 1, 2003, pp. 56–61.
Original Russian Text Copyright © 2003 by Pochtenny, Misevich.

The Effect of Adsorbed Oxygen on the Conductivity of Lead Phthalocyanine Films

A. E. Pochtenny and A. V. Misevich
Belarussian State Technological University, Minsk, Belarus
e-mail: nanom@ifttp.bas-net.by
Received July 24, 2002

Abstract—The effect of adsorbed oxygen on the conductivity of lead phthalocyanine films obtained by laser deposition in vacuum was studied by the method of cyclic thermodesorption. The results are explained in terms of the hopping conductivity model. It is suggested that the electron transport proceeds by hopping via both intrinsic and impurity centers differing by the radius of electron localization. It is shown that, using the method of cyclic thermodesorption in combination with the hopping conductivity model, it is possible to evaluate the electron transport parameters, such as concentration of the localization centers and the radius of electron localization in the intrinsic and impurity states, and to determine the type of centers (intrinsic versus impurity) involved in the hopping transport. *© 2003 MAIK "Nauka/Interperiodica".*

Phthalocyanine films are widely used in organic electronic devices such as gas sensors [1], solar cells [2], and light-emitting diodes [3]. The operation of all these devices, based on the process of electron transport, is significantly influenced by oxygen adsorbed from the atmosphere. Insufficient knowledge about the mechanism of oxygen influence upon the conductivity of phthalocyanine films hinders prediction and optimization of the properties of electronic devices employing these materials.

Previously [4, 5], we demonstrated that laser-deposited films of copper phthalocyanine and copper phthalocyanine–polystyrene composite feature the hopping conductivity mechanism. However, it was unclear which types of electron localization centers—impurity or intrinsic—are responsible for charge transfer. In the case of lead phthalocyanine films, adsorbed oxygen is bound to the adsorption centers much more weakly than in copper phthalocyanine films. For this reason, more information can be obtained about the former system by methods of thermodesorption. The purpose of this study was to elucidate the mechanism through which adsorbed oxygen influences the conductivity of lead phthalocyanine (PbPc) films and determine contributions of the intrinsic and impurity centers of electron localization to the conductivity.

The experiments were performed with 100-nm-thick PbPc films prepared in vacuum (10^{-2} Pa) by laser sputtering of a stoichiometric powder target followed by deposition of the gaseous products onto polycor (ceramic composite) substrates at room temperature. The substrates bear a preliminarily formed interdigital system of electrodes. According to our previous data obtained by scanning probe microscopy techniques [6], the PbPc films obtained using this technology possess a polycrystalline structure with a characteristic grain size of about 50 nm.

The dc conductivity of PbPc films and the temperature dependence of conductivity were measured in a vacuum of 10^{-2} Pa with the aid of a V7E-42 electrometer (Belvar company, Belarus). The investigation was performed by the method of cyclic thermodesorption [4] based on the fact [1, 2] that the conductivity of phthalocyanine films (including PbPc films) depends on the concentration of adsorbed oxygen, which can be decreased by heating a sample. Upon heating the sample in vacuum to a certain temperature, the adsorbed oxygen concentration is set at a definite controlled level. Subsequent cooling of the sample in vacuum from this temperature allows the temperature dependence of the conductivity to be measured at a constant oxygen concentration. Thus, using the cycles of heating the sample to a stepwise increased temperature followed by measurement of the temperature variation of conductivity in the course of cooling the sample from this temperature in vacuum, it is possible to obtain a series of the temperature dependences of conductivity corresponding to various concentrations of adsorbed oxygen on the same sample.

The specific conductivity σ of phthalocyanine films depends on the absolute temperature T as described by the equation

$$\sigma = \sigma_0 \exp\left(-\frac{E_a}{kT}\right), \quad (1)$$

where σ_0 is the preexponential (tunneling) factor, E_a is the conductivity activation energy, and k is the Boltzmann constant. Using this expression and the aforementioned set of experimental temperature dependences, it is possible to determine the conductivity σ

and the parameters σ_0 and E_a corresponding to various concentrations of adsorbed oxygen.

Figure 1 shows the experimental data obtained as described above using thermal cycles with the temperature of PbPc films gradually increased from 40 to 140°C. As can be seen, the desorption of oxygen is initially accompanied (portion *1–2* of the curve) by an increase both in the conductivity activation energy E_a and in the preexponential factor σ_0 (the probability of nonresonance tunneling of electrons), which corresponds to an increase in the concentration of the electron localization centers involved in the hopping transport of charge carriers. After attaining a certain critical concentration of adsorbed oxygen (Fig. 1, point *2*), further desorption of oxygen leads to a drop in the E_a and σ_0 values (portion *2–3* of the curve), which reflects a decrease in concentration of the electron localization centers.

The above results can be explained by taking into account that the transport of electrons in PbPc films can proceed both via intrinsic states characterized by the electron localization radius a_1 and via impurity states with the localization radius $a_2 < a_1$. This relation between the electron localization radii is due to the fact that such impurity centers are formed upon oxygen binding to phthalocyanine molecules, whereby the resulting impurity state falls out of the set of intrinsic states and goes down by the energy scale.

The specific conductivities σ_1 and σ_2 related to each system of levels can be expressed as

$$\sigma_1 = (\sigma_{03})_1 \exp\left(-\frac{\alpha}{a_1 n_1^{1/3}} - \frac{E_{a1}}{kT}\right),$$
$$\sigma_2 = (\sigma_{03})_2 \exp\left(-\frac{\alpha}{a_2 n_2^{1/3}} - \frac{E_{a2}}{kT}\right), \quad (2)$$

where $(\sigma_{03})_1$ and $(\sigma_{03})_2$ are the constants depending on the electron localization radius; $\alpha = 1.73$ is the percolation constant [7]; n_1 and n_2 are the concentrations of localization centers corresponding to the intrinsic and impurity states, respectively; and E_{a1} and E_{a2} are the activation energies of conductivity via the intrinsic and impurity states, respectively. The latter quantities are determined by the formulas [8]

$$E_{a1} = \frac{0.99 e^2 n_1^{1/3}}{4\pi\varepsilon_0\varepsilon}, \quad E_{a2} = \frac{0.99 e^2 n_2^{1/3}}{4\pi\varepsilon_0\varepsilon}, \quad (3)$$

where ε_0 is the permittivity of vacuum and ε is the relative permittivity.

Since the impurity levels appear as a result of separation from the set of intrinsic levels, the concentration of electron localization centers related to the intrinsic and impurity states must obey the condition

$$n_1 + n_2 = n = \text{const}. \quad (4)$$

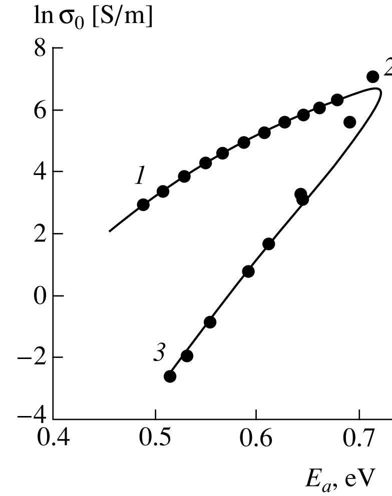

Fig. 1. Relation between the preexponential factor σ_0 and the conductivity activation energy E_a in a PbPc film for various concentrations of adsorbed oxygen. Points present the experimental data, solid curve shows the results of calculations using Eqs. (2)–(8); points *1* and *3* correspond to the maximum and minimum concentrations of oxygen adsorbed on the film; point *2* corresponds to the transition from the intrinsic to impurity type of conductivity.

Then, the specific conductivity of a material containing such impurity centers is

$$\sigma = \sigma_1 + \sigma_2. \quad (5)$$

The temperature dependence of the conductivity is described by Eq. (1), from which the conductivity activation energy can be experimentally determined as

$$E_a = -\frac{\partial(\ln\sigma)}{\partial(1/kT)}. \quad (6)$$

Using expressions (2)–(5), this formula can be transformed into

$$E_a = \frac{E_{a1}\sigma_1 + E_{a2}\sigma_2}{\sigma_1 + \sigma_2}. \quad (7)$$

The corresponding tunneling factor is calculated as

$$\sigma_0 = \sigma \exp\left(\frac{E_a}{kT}\right). \quad (8)$$

The results of calculation of the relation between the E_a and σ_0 values determined using these formulas are presented by the solid curve in Fig. 1. The calculations were performed for the parameters $a_1 = 0.425$ nm, $a_2 = 0.27$ nm, and $n = 2.15 \times 10^{26}$ m^{-3}, which provide the best fit with the experimental data. We used $\varepsilon = 1$ because the characteristic jump length corresponding to this concentration of electron localization centers is about 1 nm.

The experimental data and the results of calculations presented in Fig. 1 can be replotted in a more illustrative manner, as in Fig. 2, where $x = n_2/n$ is the

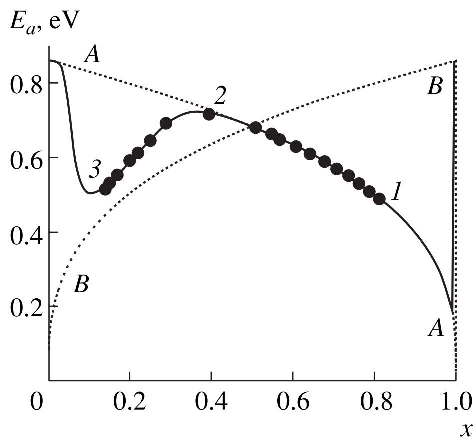

Fig. 2. Relation between the conductivity activation energy E_a and relative concentration x of oxygen adsorbed on a PbPc film. Points represent the experimental data, dotted curves show the results of calculations taking into account only intrinsic (*A–A*) or impurity (*B–B*) states, and solid curve shows the results of calculations using a two-level hopping conductivity model.

relative concentration of adsorbed oxygen molecules. At a high initial concentration of adsorbed oxygen (point *1* in Figs. 1 and 2), the conductivity and its activation energy are determined by the electron transport via intrinsic states. As oxygen is desorbed, the amount of impurity states decreases, while that of the intrinsic states accordingly increases. This leads to an increase in the conductivity activation energy and the preexponential factor (portion *1–2* in Figs. 1 and 2). At a critical oxygen concentration corresponding to point *2*, the Fermi level is trapped at the impurity states and the electron transport via these states becomes dominating in the conductivity of PbPc films with further decrease in the concentration of adsorbed oxygen. Under these conditions, the desorption of oxygen leads to a decrease both in the conductivity activation energy E_a and in the preexponential factor σ_0. Unfortunately, we failed to decrease the concentration of oxygen adsorbed on PbPc films down to a level where the conductivity type would change back from impurity to intrinsic, which must correspond to the $E_a(x)$ branch to the left of the minimum. Such a situation can probably be observed in films of perylene pigments, and the corresponding experiments are now in progress.

Thus, using the method of cyclic thermodesorption in combination with a two-level hopping conductivity model, it is possible to evaluate electron transport parameters (concentration of the localization centers and the radius of electron localization in the intrinsic and impurity states) from the shape, behavior, and parameters of the relation between preexponential factor σ_0 and activation energy E_a in the temperature dependence of conductivity. From these data, it is also possible to determine the type of centers (intrinsic versus impurity) involved in the hopping transport of electrons.

Acknowledgments. This study was supported by the program "Low-dimensional Systems" (project GB21-066).

REFERENCES

1. J. D. Wright, Prog. Surf. Sci. **31**, 1 (1989).
2. J. Simon and J.-J. Andre, *Molecular Semiconductors* (Springer-Verlag, Berlin, 1985; Mir, Moscow, 1988).
3. S. R. Forrest, Chem. Rev. **97**, 1793 (1997).
4. A. E. Pochtennyĭ, D. I. Sagaĭdak, G. G. Fedoruk, *et al.*, Fiz. Tverd. Tela (St. Petersburg) **38** (8), 2592 (1996) [Phys. Solid State **38**, 1422 (1996)].
5. A. V. Misevich and A. E. Pochtenny, Electron Technol. **33** (1/2), 167 (2000).
6. A. E. Pochtenny, O. M. Stukalov, V. L. Mironov, *et al.*, Phys. Low-Dimens. Struct. **3**/**4**, 109 (2001).
7. B. I. Shklovskiĭ and A. L. Efros, *Electronic Properties of Doped Semiconductors* (Nauka, Moscow, 1979; Springer-Verlag, New York, 1984).
8. B. I. Shklovskiĭ, A. L. Éfros, and I. Ya. Yanchev, Pis'ma Zh. Éksp. Teor. Fiz. **14** (5), 348 (1971) [JETP Lett. **14**, 233 (1971)].

Translated by P. Pozdeev

Technical Physics Letters, Vol. 29, No. 1, 2003, pp. 29–31. Translated from Pis'ma v Zhurnal Tekhnicheskoĭ Fiziki, Vol. 29, No. 1, 2003, pp. 62–68.
Original Russian Text Copyright © 2003 by Starostenko, Malishevskiĭ, Taran, Churyumov.

Near Field Zone of an Integrated Circuit Exposed to an Electromagnetic Wave in a Waveguide

V. V. Starostenko, S. V. Malishevskiĭ, E. P. Taran, and G. I. Churyumov

Tauride National University, Simferopol, Crimea, Ukraine
e-mail: taran@tnu.crimea.ua
Kharkov National University of Radioelectronics, Kharkov, Ukraine
e-mail: g.churyumov@ieee.org

Received July 10, 2002

Abstract—The electromagnetic field distribution in the vicinity of an integrated circuit was calculated based on a numerical solution of the problem of electromagnetic wave diffraction on a model metal-dielectric structure in a waveguide tract. Using the obtained field distributions, it is possible to calculate currents in the microstructural elements of integrated circuits and develop a thermoelectric model of degradation processes in such circuits under the action of pulsed electromagnetic fields. © *2003 MAIK "Nauka/Interperiodica".*

Previously [1], we experimentally studied the action of pulsed electromagnetic fields on the integrated circuits (ICs) of 155, 174, 555, and 561 series accommodating 10^3–10^4 elements per chip with 14 or 16 contacts and working crystal areas from 1×1 to 2.5×2.5 mm. The experiments, aimed at determining threshold values of the pulsed electromagnetic fields initiating degradation processes in the microstructural elements of ICs (*p*–*n* junctions, metallization elements, etc.) and resulting in the catastrophic failure of devices, were performed by exposure of the test ICs to electromagnetic waves in a waveguide.

This experimental approach was employed because measurements of the standing wave ratio ($K_{s.w}$) and the attenuation coefficient (A) in a waveguide tract provide for a much simpler determination of the relationship between incident, reflected, absorbed, and transmitted waves as compared to analogous investigations in free space. The experimental curves of $K_{s.w}(f)$ and $A(f)$ plotted in the frequency range of a panoramic meter and, hence, the relationships between the wave components provide an experimental solution of the problem of diffraction of pulsed electromagnetic waves in a waveguide tract in the far field zone of the IC. An analysis of the relationships between the wave components helps towards understanding the mechanism of a wave action upon an IC, but does not explain peculiarities of the interaction determining the local heat evolution in the microstructural elements of ICs. In order to reveal the factors determining the local heat evolution in such elements, it is necessary to develop a model of thermoelectric processes. This, in turn, requires determining the electromagnetic field structure in the vicinity of an IC.

Below, we report the results of calculations of the electromagnetic field distribution in the vicinity of an IC. Calculation was based on a numerical solution of the problem of electromagnetic wave diffraction on an IC model for the most typical cases of sample orientation in a waveguide.

The IC model and a method for solving the diffraction problem. The diffraction problem was solved using a decomposition method [2, 3]. The choice and use of the method were determined by the complexity of the IC model employed. According to the decomposition method, the IC model and the waveguide region in the vicinity of the IC were divided into sets of minimum autonomous blocks having the form of cubic structural elements (Fig. 1). The field inside each autonomous block satisfies the Maxwell equation and the boundary conditions on the cubic faces. In order to take into account the possible dielectric features, the blocks are classified into "homogeneous," "short-circuit" (for conducting regions), and "junction" types [2, 3]. Using the field representation inside a minimum autonomous block and the boundary conditions, we can determine the scattering matrices of the autonomous blocks. The scattering matrix for the whole region con-

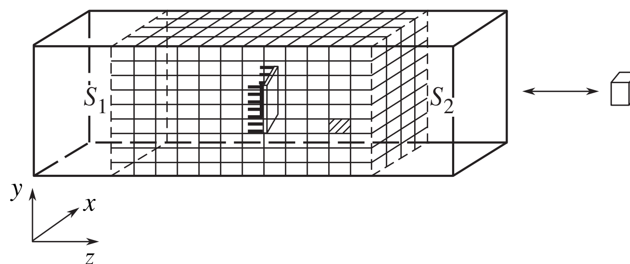

Fig. 1. Modeling a near field zone of an integrated circuit in a waveguide by a system of minimum autonomous blocks (see the text for explanations).

fined between planes S_1 and S_2 is determined using the recomposition operation.

An IC is a complicated metal-dielectric structure comprising a package with contact fingers and a chip. Setting the topology of microstructural elements for a particular IC in solving the diffraction problem seems to be impossible. For this reason, the package, contacts, and the chip in the IC model employed were quite adequate to those of the aforementioned typical IC series, while the chip microstructure was modeled by homogeneous layers of silicon, silicon dioxide, and aluminum (metallization).

The model of the IC chip represented a four-layer structure comprising a silicon substrate, a dielectric layer (silicon dioxide), a metal film (aluminum), and a protective coating (silicon dioxide) [4]. A decomposition scheme of the IC chip model included homogeneous autonomous blocks (of silicon and silicon dioxide), short-circuit blocks representing reaction of the conducting (aluminum) elements with the incident electromagnetic wave, and junction blocks occurring between minimum autonomous blocks with different electrical properties.

The algorithm used to find the differential and integral characteristics (field distributions in various cross sections of the S_1S_2 region and elements of the scattering matrix) in the problem of diffraction of a pulsed electromagnetic field on the IC model can be described as follows [2, 3]:

(i) determine the scattering matrices and identify the short-circuit and junction blocks among all autonomous blocks;

(ii) construct the overall scattering matrix for the field diffraction on the IC model;

(iii) set the incident wave type;

(iv) construct input and output filters;

(v) calculate amplitudes and phases of the waves of all types near the IC and construct a general pattern of the electromagnetic field distribution;

(vi) calculate the standing wave ratio ($K_{s.w}$) and the attenuation coefficient (A); determine the currents induced in the structural elements.

The direct and inverse Fourier transforms are performed by filters. The filters are also used to calculate amplitudes of the waves appearing in the open channels of each autonomous block (S_1 and S_2 planes). Numerical calculations are performed using the filters combining standard filters and commutators [2, 3]. This accelerates the numerical solution of the diffraction problem and the calculation of the electromagnetic field distribution near the IC model with allowance for higher wave modes.

Near field zone of an IC in a waveguide. The diffraction problem was numerically solved using the following geometric and electrical parameters: contact finger dimensions, 5.25 × 0.5 × 0.3 mm; distance between contacts, 2 mm; IC package dimensions 17 × 6.6 × 3.1 mm; crystal (silicon, $\varepsilon = 7$) dimensions, 1 × 1 × 0.1 mm; dielectric (silicon dioxide, $\varepsilon = 13$) layer dimensions, 1 × 1 × 0.0006 mm; metallization (Al film) layer dimensions, 1 × 1 × 0.0012 mm; protective layer (silicon dioxide) identical to dielectric layer. The metal layer and contacts were assumed to possess infinite conductivity.

The adequacy of the IC model employed and correctness of the solution to the problem of electromagnetic wave diffraction on the IC model in a waveguide were checked by comparing the experimental curves of $K_{s.w}(f)$ and $A(f)$, obtained using a panoramic meter of the P2-56 type, to the analogous curves calculated using the decomposition method. The measurements of $K_{s.w}(f)$ and $A(f)$ were performed in the frequency range of f = 2400–4100 MHz using a waveguide with a 34 × 72 mm cross section. The experiments were conducted under the condition of $\lambda \gg l$ (where l is the maximum dimension of the IC), which corresponds to the absence of resonances related to the comparable dimensions of IC (or its elements) and the radiation wavelength. It is possible to distinguish between the six most characteristic IC positions in the waveguide (or IC orientations relative to the electric field vector of the fundamental wave mode H_{10} in the rectangular waveguide [1]). For four of these IC positions, the $K_{s.w}$ values vary from 1.3 to 1.6, while the two other positions (with the long package side parallel to the electric field vector of the H_{10} wave) correspond to $K_{s.w}$ within 2.6–2.8. For all six IC positions in the waveguide, the difference between the integral parameters ($K_{s.w}$ and A) measured in the experiment in the indicated frequency range and those calculated using the decomposition method did not exceed 15%.

In addition, the adequacy of the program package was checked for a test structure representing a set of seven to ten metal rods (with dimensions corresponding to the IC contact fingers) arranged on the wide waveguide wall. The field calculations were performed taking into account up to 60 waveguide modes. The results of these calculations showed that, beginning with the 20–30th mode (according to the critical wavelength diagram), the wave amplitude amounts to no more than 0.5% of the H_{10} wave amplitude. The tangential field component on the rods was equal to zero.

During the electromagnetic wave diffraction on an IC in the waveguide, fields in the near and far field zones form a package with contact fingers and a chip. For ICs of the aforementioned types and the indicated frequency range, the chip dimensions are such that no differences in the near field are observed even for the chip position in which the crystal face bearing microstructural elements is perpendicular to the waveguide axis. This result could be anticipated, since the ratio of the wavelength to the maximum chip size is on the order of 10^3. For the other positions of IC in the waveguide, the chip introduces even smaller perturbations in the field distribution.

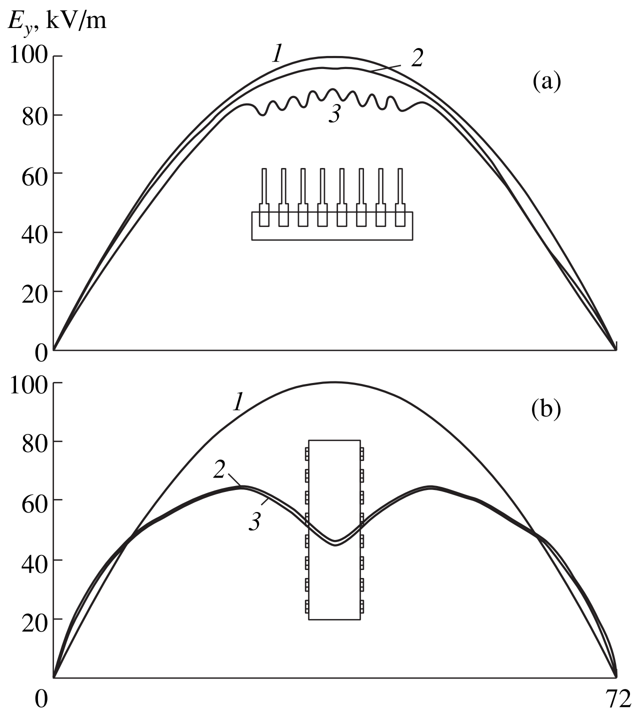

Fig. 2. Electromagnetic field distribution in the cross section of a waveguide in the vicinity of an IC taking different orientations relative to the electric field vector of the H_{10} wave: (*1*) incident wave; (*2*) field strength profile as perturbed by the IC package; (*3*) field strength profile perturbed by the IC package and contact fingers.

Depending on the IC position in the waveguide, a greater perturbation in the near field zone can be introduced by the IC package and contact fingers. Figure 2 shows a distribution of the electromagnetic field in the vicinity of an IC taking two characteristic positions in the waveguide. When the IC contact fingers are oriented along the electric field vector of the H_{10} wave (Fig. 2a), the IC package virtually does not influence the magnitude and structure of the electric field in the waveguide, whereas the contact fingers significantly alter the field distribution and strength (up to 15% as compared to that in the waveguide without IC). If, however, the IC is oriented with its maximum dimension along the electric field vector of the H_{10} wave (Fig. 2b), a maximum contribution to the field perturbation is due to the IC package, while the contact fingers produce virtually no changes in the field structure. The field strength near the IC package differs by more than 20% from the value in the same waveguide without IC.

Thus, the results of our calculations agree with the experimental data for the far field zone. The near field values obtained for the IC model in a waveguide can be used for determining the conduction currents induced in the metallization elements and the displacement currents in the dielectric and semiconductor structures of ICs, in particular, for modeling thermoelectric processes in their microstructural elements. In addition, successful verification of the decomposition method for solving the problem of electromagnetic wave diffraction on an IC in the longwave approximation allows this method and the corresponding program package to be applied to modeling diffraction in free space for an arbitrary ratio of the scattering object dimensions and the electromagnetic radiation wavelength [5].

REFERENCES

1. V. V. Starostenko, E. P. Taran, E. V. Grigor'ev, *et al.*, Izmer. Tekh., No. 4, 65 (1998).
2. V. V. Nikol'skiĭ and T. I. Nikol'skaya, *Decomposition Approach to Problems of Electrodynamics* (Nauka, Moscow, 1983).
3. V. V. Nikol'skiĭ and T. I. Nikol'skaya, *Electrodynamics and Radio-Wave Propagation* (Nauka, Moscow, 1989).
4. E. P. Taran, V. V. Starostenko, and E. V. Grigor'ev, Radiofiz. Élektron. **3** (1), 123 (1998).
5. V. A. Fok, *Problems of Diffraction and Electromagnetic Wave Propagation* (Sov. Radio, Moscow, 1970).

Translated by P. Pozdeev

Technical Physics Letters, Vol. 29, No. 1, 2003, pp. 32–34. Translated from Pis'ma v Zhurnal Tekhnicheskoĭ Fiziki, Vol. 29, No. 1, 2003, pp. 69–74.
Original Russian Text Copyright © 2003 by Maslovski.

On the Possibility of Creating Artificial Media Simultaneously Possessing Negative Permittivity and Permeability

S. I. Maslovski
St. Petersburg State Technical University, St. Petersburg, 195251 Russia
e-mail: stas@cc.hut.fi
Received August 6, 2002

Abstract—Artificial magnetodielectric media are considered which are composed of two subsystems—one, possessing a negative dielectric permittivity and another, possessing a negative magnetic permeability. It is shown that the resulting composite material is characterized by a negative refractive index only under certain special conditions: in the absence of a strong quasistatic coupling between the two subsystems. *© 2003 MAIK "Nauka/Interperiodica".*

In recent years, there has been considerable interest in artificial materials possessing a negative refractive index for visible light (or for microwaves). The phenomenon of negative refraction, while being of independent fundamental interest, can lead to new applications of the so-called photonic crystals on which extensive research has also recently been focused.

The basic work in the theory of media with negative refractivities was made in the 1960s by Veselago [1]. It was pointed out that optical devices of a new type can be created using the laws of negative refraction. At present, the effort of many research groups is concentrated on the development of such devices.

The aim of this study was to show that an arbitrary "mixture" of two materials separately possessing negative ϵ and μ values will by no means necessarily exhibit a negative refractivity. This will be demonstrated for a subsystem of resonant inclusions in the form of double open rings, so-called split-ring resonators (SRRs), incorporated into a crystal composed of straight conductors (this model was considered, e.g., in [2–4]).

It was recently reported [5] that the complex dielectric permittivity dyadic of a crystal composed of thin, straight nonideally conducting metal cylinders of radius r_0, oriented in a direction determined by the unit vector $\mathbf{z}_0$, can be determined in a quasistatic approximation and expressed as

$$\overline{\overline{\epsilon}} = \epsilon_0\left(\overline{\overline{I}} - \frac{2\pi\mathbf{z}_0\mathbf{z}_0}{(ka)^2\log\dfrac{a^2}{4r_0(a-r_0)} - \dfrac{jka^2}{r_0}\dfrac{Z_s}{\eta}}\right), \quad (1)$$

where $\overline{\overline{I}}$ is the unit dyadic, ϵ_0 is the permittivity of vacuum, a is the square lattice constant, $k = 2\pi/\lambda$ is the wavenumber in the free space, $\eta = 377\ \Omega$ is the wave impedance of free space, and Z_s is the effective surface impedance of the metal cylinders describing losses in a thin skin layer of the metal. Formula (1) was obtained assuming that the metal cylinders occur in a medium possessing a dielectric permittivity and magnetic permeability equal to those of the free space. Upon accomplishing the algebraic transformations (analogous to those in [5]) for a medium with a relative dielectric permittivity ϵ and magnetic permeability μ, we obtain the following expression for the complex permittivity of the model crystal under consideration (losses are neglected):

$$\overline{\overline{\epsilon}}_{\rm mix} = \epsilon_0\left(\epsilon\overline{\overline{I}} - \frac{2\pi\mathbf{z}_0\mathbf{z}_0}{\mu(ka)^2\log\dfrac{a^2}{4r_0(a-r_0)}}\right). \quad (2)$$

As can be seen from this expression, the effective permittivity of the crystal obtained in the quasistatic approximation depends on the magnetic permeability of the medium. This unusual result is related to the fact that the dielectric response of the medium (i.e., the macroscopic polarization current) in the crystal composed of conducting cylinders is the average of the usual electric currents passing over the surface of cylinders. The magnitude of the longitudinal current component (parallel to the cylinder axis) is determined (as shown in [5]) by the effective inductance of cylindrical conductors. The latter quantity naturally depends on the magnetic properties of the medium.

It also follows from formula (2) that, with a host medium characterized by a negative magnetic permeability and a positive permittivity ($\epsilon > 0$), it is impossible to obtain a negative effective permittivity $\epsilon_{{\rm mix}\,zz}$. Then, the question arises as to how this conclusion agrees with the results reported in [3, 4], where it was suggested that the material parameters of the mixture

1063-7850/03/2901-0032$24.00 © 2003 MAIK "Nauka/Interperiodica"

are merely represented by the corresponding characteristics of the electric and magnetic components.

An answer is provided by thorough analysis of the structure of samples used in the experiments and simulations described in [3, 4]. Indeed, the double open rings (SRRs) accounting for the negative magnetic permeability of the composite are situated at the points where a quasistatic magnetic field of the subsystem of cylinders is zero. For this reason, the two subsystems are decoupled with respect to the near magnetic field and, hence, the negative magnetic permeability of the SRR subsystem does not influence the effective permittivity of the subsystem of dielectric cylinders (and that of the whole system). By the same token, the negative permittivity of the subsystem of dielectric cylinders does not influence the magnetic permeability of the SRR subsystem: the cylinders are arranged where the longitudinal component of the near electric field (averaged over their surfaces) created by the SRR subsystem is zero.

Figures 1 and 2 present the results of calculations illustrating the main conclusions formulated above. The curves refer to a system formed by SRRs with a resonance frequency of 3.85 GHz incorporated into a crystal composed of conducting cylinders. The plasma frequency of the subsystem of cylinders (determined as the frequency at which the real part of the permittivity changes sign) is selected close to 10 GHz. The resonance frequency and magnetic polarizability of a SRR element were calculated for a simple *LC* circuit model valid in a range of wavelengths significantly greater than the SRR size. The total magnetic permeability of the SRR subsystem was calculated within the framework of the modified Maxwell–Garnett approach ensuring correct allowance of scattering losses in regular systems (see [6]). We have also taken into account the dissipative losses in both metal (cylinders) and dielectric (SRRs) components. The permittivity of the subsystem of conducting cylinders was calculated by formula (1).

In Fig. 1, the dotted curve shows the frequency dependence of the real part of the complex magnetic permeability of the SRR subsystem. This curve exhibits a clearly pronounced resonance character. In a certain region of frequencies above the resonance, the real part of the magnetic permeability is negative. The solid curve in Fig. 1 shows the frequency dependence of the real part of the complex permittivity of the subsystem of dielectric cylinders. The overall system is characterized by the same permittivity in the absence of a quasistatic coupling between the subsystems of cylinders and SRRs. When the interaction between the two subsystems via the near field cannot be ignored, the permittivity of the composite medium has to be calculated by an expression analogous to formula (2). The real part of the permittivity for such a case is depicted by the dashed curve in Fig. 1. As can be seen, the real part of the effective permittivity of the system becomes positive in the vicinity of a strong resonance of the SRR subsystem.

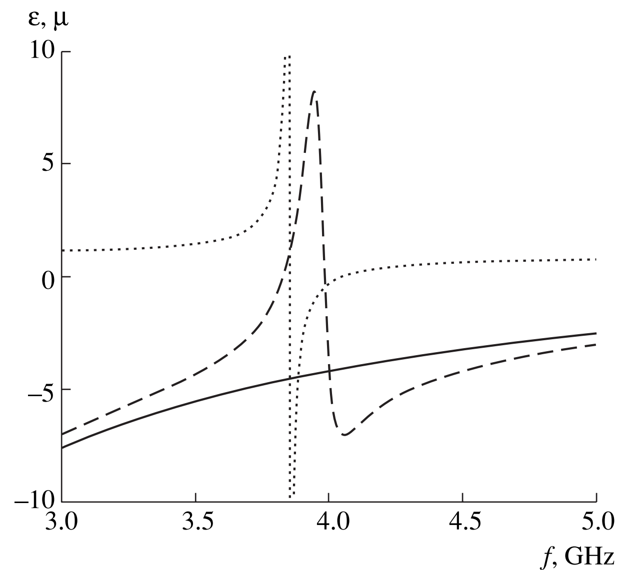

Fig. 1. Frequency dependences of the real parts of the magnetic permeability of the SRR subsystem (dotted curve), the permittivity of the subsystem of conducting cylinders (solid curve), and the effective permittivity of the composite system (dashed curve).

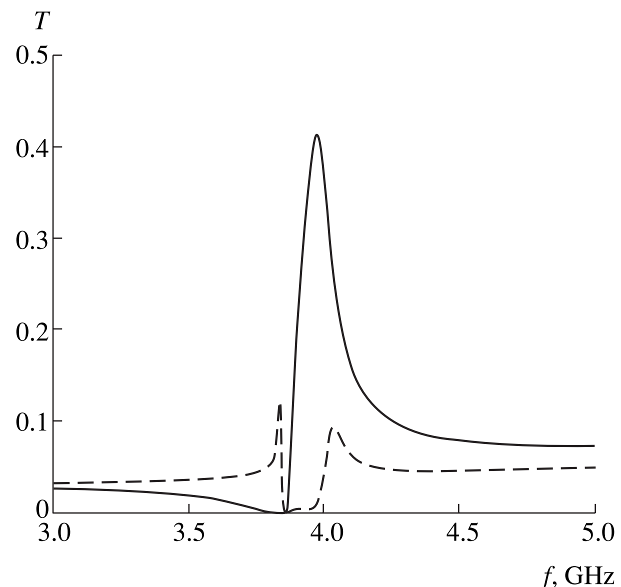

Fig. 2. Frequency dependences of the transmission of a composite material layer in the case of weak (solid curve) and strong (dashed curve) coupling of the subsystems.

Figure 2 shows the frequency dependences of the absolute values of the transmission coefficients calculated for a layer of the composite material under consideration. Here, the solid curve corresponds to the case of a special mutual arrangement of the subsystems of cylinders and SRRs, whereby quasistatic coupling between the two subsystems can be ignored. The

dashed curve represents the opposite case of a strong interaction between the cylinders and SRRs. As can be seen, a transmission peak is present in the former curve and absent in the latter.

Based on the results of this small investigation, it is possible to conclude that simultaneous negativity of the material parameters of an artificial composite medium composed of two subsystems—electric and magnetic—is possible only under certain conditions ensuring a weak coupling between these subsystems.

In the case of a strong interaction between the subsystems, for example, when their characteristic spatial scales are significantly different and one subsystem can be considered as an effective medium containing the other subsystem, it is impossible to obtain simultaneously negative values of the permittivity and permeability of the composite medium.

REFERENCES

1. V. G. Veselago, Usp. Fiz. Nauk **92** (3), 517 (1967) [Sov. Phys. Usp. **10**, 509 (1968)].
2. M. V. Kostin and V. V. Shevchenko, J. Commun. Technol. Electron. **38** (5), 78 (1993).
3. D. R. Smith, W. J. Padilla, D. C. Vier, *et al.*, Phys. Rev. Lett. **84** (18), 4184 (2000).
4. R. A. Shelby, D. R. Smith, and S. Shultz, Science **292**, 77 (2001).
5. S. I. Maslovski, S. A. Tretyakov, and P. A. Belov, Microwave Opt. Technol. Lett. **35** (1), 47 (2002).
6. J. E. Sipe and J. van Kranendonk, Phys. Rev. A **9** (5), 1806 (1974).

Translated by P. Pozdeev

Technical Physics Letters, Vol. 29, No. 1, 2003, pp. 35–38. Translated from Pis'ma v Zhurnal Tekhnicheskoĭ Fiziki, Vol. 29, No. 1, 2003, pp. 75–83.
Original Russian Text Copyright © 2003 by Savkov.

On the Analytical Solution of a Nonstationary Kinetic Equation for a Point Heat Source

S. A. Savkov

Orel State University, Orel, Russia

Received April 22, 2002; in final form, July 15, 2002

Abstract—A nonstationary kinetic equation for a point heat source in a gas is analytically solved. The dependence of the temperature and concentration of gas molecules on the distance from the source is considered. The results are compared to experimental data on the spreading of acoustic oscillations. © *2003 MAIK "Nauka/Interperiodica".*

Investigation into the process of heat and mass transfer are of importance for both basic science and applications. An analysis of such phenomena is necessary, in particular, for the interpretation of thermal effects accompanying the interaction of laser radiation with matter [1]. Important examples are offered by the self-focusing and defocusing of a laser beam propagating in an absorbing medium [2–4]. Another important problem is the behavior of a gas near a heated solid surface [5], including the generation and propagation of thermoacoustic waves [6].

The existing theoretical descriptions of the latter phenomenon are usually given within the framework of the dynamics of continuum. However, in cases where heat evolution takes place in a region with dimensions much smaller compared to the mean free path length of molecules, the state of the gas is determined by a kinetic equation. Moreover, the region of heat evolution can be considered as a point source. Evidently, in the general case, the region in which heat evolution takes place can be considered as a superposition of such point sources.

An analogous situation is observed when a characteristic time of the process of heat evolution is comparable with the mean free flight time of molecules in the gas. For arbitrary time variation of the power source, this quantity can be represented as the Fourier integral

$$W(t) = \int_{-\infty}^{+\infty} W_\omega \exp(i\omega t) d\omega,$$
$$W_\omega = \frac{1}{2\pi}\int_{-\infty}^{+\infty} W(t)\exp(-i\omega t)dt, \quad (1)$$

which implies the expediency of considering the basic case of a point source with the power varying according to the harmonic law

$$W = \exp(i\omega t). \quad (2)$$

An analytical solution to the nonstationary kinetic equation of this model (known as the Bhatnagara–Gross–Crook model) was presented elsewhere [7]. This letter is devoted to an analysis of the physical meaning of this solution.

It was demonstrated [7] that the distribution of any thermodynamic parameter of gas can be represented as a sum of the discrete and continuous spectra and that each spectrum can be considered as a spherical wave. There are two solutions for the discrete spectrum in the range of frequencies $\omega < 0.646$, one discrete solution in the interval $0.646 < \omega < 2.145$, and no such solutions exist for $\omega > 2.145$.

Figure 1 plots the absolute values of relative differences of the temperature and concentration of gas molecules versus the distance from the point source. Here, the time t and distance r are measured in units of

$$\tau = \frac{3\mu}{2nkT} \quad \text{and} \quad l = \tau\sqrt{\frac{2kT}{m}}, \quad (3)$$

corresponding to the mean free path length and flight time of molecules in the gas (μ is the dynamic gas viscosity coefficient). Figure 2 gives an example of the particular contributions from the continuous (dashed curve) and discrete (dash–dot curve) spectra to the total distributions.

In the region of small distances r, the gas temperature and concentration profiles are described

1063-7850/03/2901-0035$24.00 © 2003 MAIK "Nauka/Interperiodica"

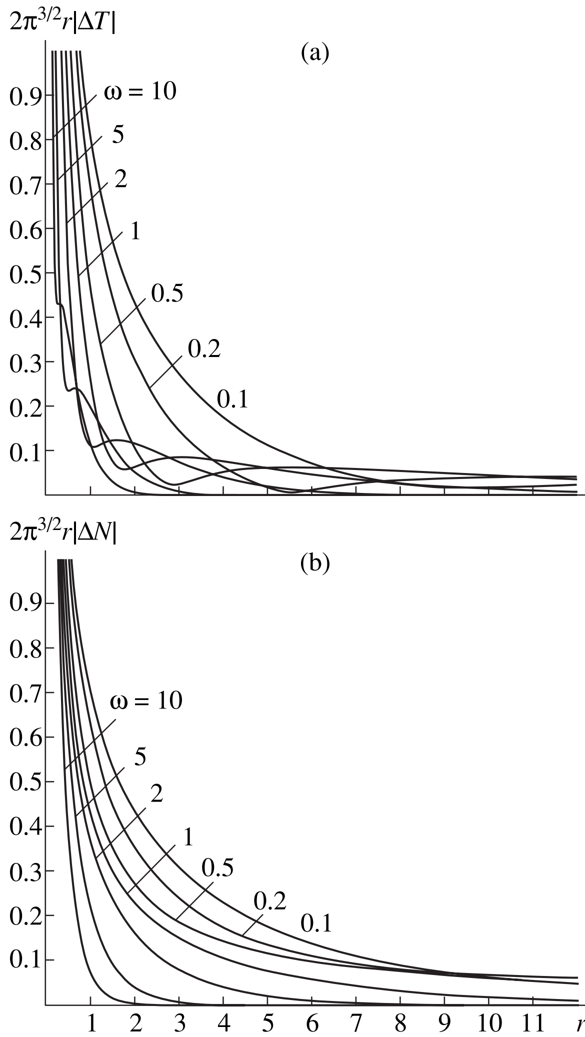

Fig. 1. Variation of the relative (a) temperature and (b) gas concentration differences depending on the distance r from a point source at various fixed frequencies ω.

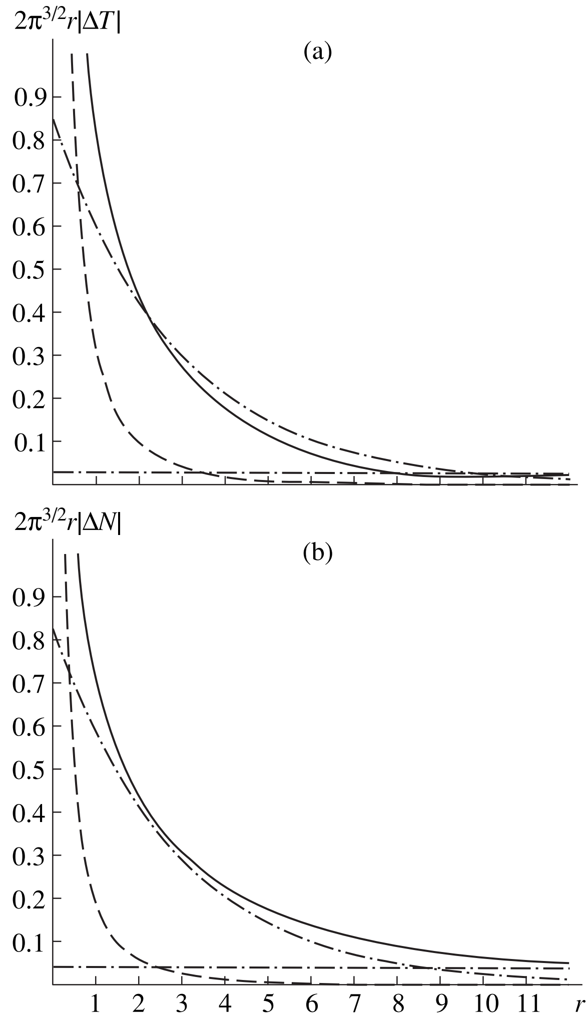

Fig. 2. Contributions from the continuous (dashed curve) and discrete (dash–dot curve) spectra to the total distributions (solid curve) of the gas (a) temperature and (b) concentration differences (for $\omega = 0.1$).

by the expressions

$$\Delta T = \frac{T(r) - T_0}{T_0} = \frac{5}{18\pi^{3/2}r^2},$$
$$\Delta N = \frac{n(r) - n_0}{n_0} = -\frac{1}{6\pi^{3/2}r^2}; \quad (4)$$

that is, they are determined only by the instantaneous source power while being independent of the frequency ω. This character of dependence ($1/r^2$) on the distance is determined by the continuous spectrum.

As the distance from the source increases, the continuous solutions decay more rapidly than do the discrete ones. Among the discrete solutions, the slowest decay is observed for the spectrum which produces a minimum contribution in the immediate vicinity of the source. It is this slowly decaying solution (provided

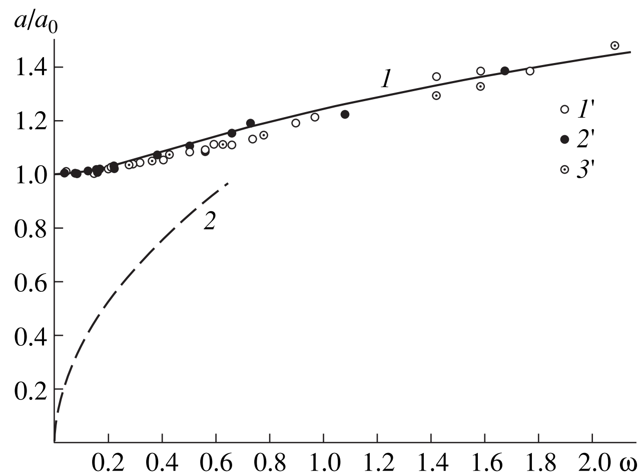

Fig. 3. Plots of the calculated phase velocities of the acoustic (curve *1*) and temperature (curve *2*) waves versus frequency in comparison with the experimental data taken from [8] for helium (*1*'), argon (*2*'), and xenon (*3*').

that it does exist) which determines the variation of the macroscopic parameters for $r \longrightarrow \infty$. Depending on the particular frequency, the discrete solutions may contribute either in phase or with opposite phases, thereby determining the presence or absence of bending points in the profiles under consideration.

In the limit of $\omega \longrightarrow 0$ and $r \longrightarrow \infty$, the gas temperature and concentration profiles are given by the well-known expressions

$$\Delta T = -\Delta N = \frac{1}{5\pi r}. \quad (5)$$

It is also of interest to study the relative gas pressure drop

$$\Delta P = \frac{P - P_0}{P_0} = \Delta T + \Delta N. \quad (6)$$

In contrast to the gas temperature and concentration, the behavior of the ΔP value in the limit of $\omega \longrightarrow 0$ is determined only by solutions for the continuous spectrum, while the total contribution of the discrete spectrum is zero. As the frequency increases, the contribution of the discrete solutions increases and, eventually, the differential pressure profile is described by the expression

$$\Delta P = \sum_{i=1}^{\kappa} \frac{A_i}{2\pi r}(i(\omega t - k_i) - d_i r + \delta_i), \quad (7)$$

which can be considered as a superposition of spherical waves. The coefficients of this expression for a gas with a heat source at various frequencies are given in Tables 1 and 2.

The phase velocity of these wave processes is determined by the relation between a_i and ω/k_i. In the limit of $\omega \longrightarrow 0$, we obtain $a_1 = \sqrt{5/6}$ and $a_2 = \sqrt{\omega}$. On return to dimensional variables, this yields $a_1 = a_0 = \sqrt{5kT/3m}$, which coincides with the velocity of sound calculated within the framework of the dynamics of continuum. The value of $a_2 = \sqrt{3\mu\omega/mn}$ corresponds to the velocity of propagation of the temperature wave.

Figure 3 shows the calculated curves of phase velocities of the acoustic (curve *1*) and temperature (curve *2*) waves versus frequency in comparison with the experimental data for helium (*1*'), argon (*2*'), and xenon (*3*') [8].

As can be seen from the data presented in Figs. 1–3 and Tables 1 and 2, an increase in the frequency is accompanied by a growth in the amplitude and phase velocity of each wave, as well as in the wave decay rate. As the frequency approaches the boundary of the interval of existence of the discrete solutions, the decay rate of the acoustic wave becomes close to that of the continuous spectrum. Thus, the range of frequencies in

Table 1. Acoustic wave parameters

ω	A_1	k_1	d_1	δ_1
0.001	0.00126	0.00110	0.00000	0.49955π
0.01	0.01256	0.01095	0.00007	0.49555π
0.1	0.12386	0.10865	0.00637	0.45694π
0.2	0.23983	0.21291	0.02357	0.42058π
0.3	0.34759	0.31117	0.04809	0.39166π
0.4	0.45005	0.40373	0.07724	0.36835π
0.5	0.54975	0.49141	0.10941	0.34897π
0.6	0.64837	0.57501	0.14361	0.33240π
0.646	0.69368	0.61227	0.15986	0.32551π
0.647	0.69467	0.61308	0.16022	0.32537π
0.7	0.74697	0.65517	0.17928	0.31792π
0.8	0.84618	0.73242	0.21602	0.30505π
0.9	0.94645	0.80718	0.25360	0.29347π
1.0	1.04803	0.87977	0.29182	0.28294π
1.1	1.15111	0.95045	0.33057	0.27328π
1.2	1.25582	1.01944	0.36974	0.26438π
1.3	1.36224	1.08692	0.40927	0.25611π
1.4	1.47043	1.15303	0.44910	0.24840π
1.5	1.58043	1.21791	0.48918	0.24118π
1.6	1.69226	1.28165	0.52947	0.23440π
1.7	1.80593	1.34436	0.56996	0.22800π
1.8	1.92147	1.40612	0.61060	0.22194π
1.9	2.03886	1.46699	0.65138	0.21620π
2.0	2.15812	1.52703	0.69228	0.21075π
2.1	2.27924	1.58631	0.73329	0.20555π
2.145	2.33435	1.61274	0.75178	0.20329π

Table 2. Temperature wave parameters

ω	A_2	k_2	d_2	δ_2
0.001	0.00126	0.03159	0.03165	–0.50045π
0.01	0.01258	0.09914	0.10093	–0.50439π
0.1	0.13291	0.29910	0.34715	–0.52315π
0.2	0.27382	0.41505	0.52699	–0.52665π
0.3	0.41484	0.50408	0.68102	–0.53079π
0.4	0.55637	0.57945	0.82129	–0.53651π
0.5	0.69967	0.64612	0.95265	–0.54300π
0.6	0.84561	0.70661	1.07764	–0.54970π
0.646	0.91379	0.73281	1.13343	–0.55277π

which it is possible to separate pure acoustic oscillations is restricted to $\omega \sim 2$.

Acknowledgments. The author is grateful to Prof. A.I. Osipov and Prof. A.V. Uvarov for fruitful discussions and valuable advice.

REFERENCES

1. A. I. Osipov and V. Ya. Panchenko, *Thermal Effects under Interaction of Laser Emission with Molecular Gases* (Mosk. Gos. Univ., Moscow, 1983).
2. S. A. Akhmanov, A. P. Sukhorukov, and R. V. Khokhlov, Usp. Fiz. Nauk **93** (1), 19 (1967) [Sov. Phys. Usp. **10**, 609 (1968)].
3. A. D. Wood, M. Camac, and E. T. Gerry, Appl. Opt. **10** (8), 1877 (1971).
4. E. L. Breig, J. Opt. Soc. Am. **62** (4), 518 (1972).
5. D. C. Wadsworth, D. A. Erwin, and E. P. Muntz, J. Fluid Mech. **248**, 219 (1993).
6. Yu. Huang and H. Ban Haim, Int. J. Heat Mass Transf. **38** (8), 1329 (1995).
7. S. A. Savkov and A. A. Yushkanov, Teor. Mat. Fiz. **113** (1), 139 (1997).
8. M. Greenspan, J. Acoust. Soc. Am. **28** (8), 644 (1956).

Translated by P. Pozdeev

Technical Physics Letters, Vol. 29, No. 1, 2003, pp. 39–40. Translated from Pis'ma v Zhurnal Tekhnicheskoĭ Fiziki, Vol. 29, No. 1, 2003, pp. 84–87.
Original Russian Text Copyright © 2003 by Emel'yanov.

Electron Work Function Estimated from the Delay Time of Breakdown in Vacuum

A. A. Emel'yanov

Orel State Technical University, Orel, Russia

e-mail: orelrce@ostu.ru

Received June 11, 2002; in final form, August 7, 2002

Abstract—The delay time of an interelectrode gap breakdown in vacuum was studied. A method for estimating the electron work function of a cathode with an extended working surface is proposed based on the breakdown delay measurements using applied voltage in the form of rectangular pulses or a sawtooth wave. *© 2003 MAIK "Nauka/Interperiodica".*

In monitoring the state of a cathode surface in a vacuum gap formed by electrodes with extended working surfaces, the electron work function (φ) is usually assumed to be known, despite the fact that the values determined from the results of electron emission measurements usually exhibit considerable scatter. Indeed, the electron work function of pure aluminum has not been determined in experiments with cold emission, while the oxidized surface is characterized by φ_{Al} = 3.8–4.7 eV; the corresponding value for pure copper is φ_{Cu} = 4.55 eV, while the electron work function of the oxidized metal varies from 2 to 5.15 eV [1].

For determining the electron work function from cold emission measurements, a high dc voltage is applied to a vacuum discharge gap with a cathode having the shape of a filament or point and the electric field strength at the cathode surface is determined. Then, the current–voltage characteristic is plotted in the Fowler–Nordheim equation coordinates and the φ value is determined from the slope of this plot. This method, stipulating the use of a cathode of known geometry for calculating the microscopic electric field strength, is inapplicable to cathodes possessing extended working surfaces on which a microroughnesses of unknown shape can be present.

In order to develop a method for estimating the electron work function of a cathode with an extended working surface, the breakdown delay time of a discharge gap in vacuum was studied using applied voltage in the form of rectangular pulses and a sawtooth wave.

Analytical expressions for the breakdown delay time were derived for a microemitter possessing an arbitrary shape, with the vacuum discharge initiated by high-voltage pulses of different shapes with a duration t_p within the interval [2]

$$t_r \ll t_p \ll h^2\rho c\lambda^{-1}, \tag{1}$$

where t_r is the thermal relaxation time; h is the microemitter height; and ρ, c, and λ are the density, specific heat, and thermal conductivity of the emitter material, respectively. Provided that the microemitter is heated according to the Joule mechanism, the breakdown delay time for rectangular voltage pulses with a negligibly small front width is

$$t_{d0} = 4.22\times10^{11}\frac{a\rho c\varphi^2}{\kappa_0}\exp\{-21.6\varphi^{-1/2}\} \times\frac{\exp\{1.32\times10^{10}\varphi^{3/2}E^{-1}\}}{E^4} \tag{2}$$

and that for a sawtooth voltage wave is

$$t_{d2} = 1.32\times10^{10}\varphi^{3/2}E^{-1}t_{d0}, \tag{3}$$

where κ_0 is a proportionality factor in the temperature dependence of resistivity $\kappa(T) = \kappa_0 T$, E is the electric field strength, and a is a coefficient slowly varying with the E value.

Once the emitter geometry is known, it is possible to estimate the electron work function using formulas (2) and (3) upon measuring the breakdown delay times t_1 and t_2 for the applied electric field strengths E_1 and E_2, respectively. The resulting expression is

$$\varphi = 1.79\times10^{-7}\left(\frac{E_1E_2}{E_2-E_1}\ln\frac{t_1E_1^4}{t_2E_2^4}\right)^{2/3} \tag{4}$$

for the rectangular high-voltage pulses and

$$\varphi = 1.79\times10^{-7}\left(\frac{E_1E_2}{E_2-E_1}\ln\frac{t_1E_1^5}{t_2E_2^5}\right)^{2/3} \tag{5}$$

for the sawtooth voltage wave. From the experimental curve of $t_d = f(E)$ measured using rectangular voltage pulses ($t_f = 10^{-9}$ s) for a single crystal tungsten point

cathode [3], it follows that $t_1 = 10^{-6}$ s for $E_1 = 7.2 \times 10^9$ V/m and $t_2 = 10^{-8}$ s for $E_2 = 9 \times 10^9$ V/m. According to formula (4), these values correspond to $\varphi_W = 4.7$ eV, which differs by less than 4% from the well-known reference value of 4.54 eV [4].

Investigations of the process of high-voltage conditioning of electrodes in vacuum [5] showed that the treatment with pulses of a duration equal to the breakdown delay time ($t_p = t_d$) leads to the formation of a cathode surface microrelief characterized by the field enhancement coefficient

$$\beta = 1.28 \times 10^9 E_0^{-0.9}, \qquad (6)$$

where E_0 is the macroscopic electric field strength initiating the breakdown. Using formulas (2), (3), and (6), we obtain the following expressions for estimating the electron work function upon measuring the breakdown delay times t_1 and t_2 at the macroscopic electric field strengths E_1 and E_2, respectively:

$$\varphi = 0.21\left(\frac{(E_1E_2)^{0.1}}{E_2^{0.1} - E_1^{0.1}} \ln\frac{t_1E_1^{0.4}}{t_2E_2^{0.4}}\right)^{2/3} \qquad (7)$$

for the rectangular high-voltage pulses and

$$\varphi = 0.21\left(\frac{(E_1E_2)^{0.1}}{E_2^{0.1} - E_1^{0.1}} \ln\frac{t_1E_1^{0.5}}{t_2E_2^{0.5}}\right)^{2/3} \qquad (8)$$

for the sawtooth voltage wave.

Thus, using formulas (7) and (8), one can estimate the φ value of a cathode with an extended working surface from experimental data on the breakdown delay time obtained using high-voltage pulses with $t_p = t_d$. Measurements of the breakdown delay time in a vacuum discharge [6] for a homogeneous field between chromium electrodes (with an area of $S = 500$ mm^2) generated by rectangular high-voltage pulses ($t_f = 4 \times 10^{-9}$ s) gave $t_1 = 1.3 \times 10^{-7}$ s and $t_2 = 10^{-8}$ s for $E_1 = 2.1 \times 10^7$ V/m and $E_2 = 6.4 \times 10^7$ V/m, respectively. According to formula (7), these values correspond to the electron work function of chromium $\varphi_{Cr} = 4.6$ eV, which virtually coincides with the well-known reference value of 4.58 eV [4].

The electron work function of electrodes with an extended working surface treated by high-voltage pulses with $t_p = t_d$ can also be estimated by comparing the values of the breakdown delay times obtained at $E_0 =$ const using voltage pulses of different shapes. Using formulas (2), (3), and (6), we obtain the following expression for estimating the electron work function from the results of such measurements employing rectangular pulses and sawtooth voltage wave:

$$\varphi = 0.21 E_0^{1/15}(t_{d2}/t_{d0})^{2/3}. \qquad (9)$$

According to the results of experiments in a setup with aluminum electrodes (a spherical cathode with a radius of 75 mm and a disk anode with a radius of 100 mm) [7], the breakdown delay times at $E_0 = 9 \times 10^{-7}$ V/m were $t_{d2} = 1.3 \times 10^{-5}$ s and $t_{d0} = 7.4 \times 10^{-7}$ s for a sawtooth voltage wave and a rectangular pulse ($t_f = 4 \times 10^{-9}$ s), respectively. For these values, formula (9) yields $\varphi_{Al} = 4.4$ eV, which agrees well with the well-known reference value of 4.25 eV [4].

Thus, a technique was suggested for estimating the electron work function from experimental data on the breakdown delay time in a vacuum discharge. This method allows φ values to be determined for cathodes with extended working surfaces and can be useful for the study of electrical phenomena in vacuum.

REFERENCES

1. I. N. Slivkov, *Processes under High Voltage in Vacuum* (Énergoatomizdat, Moscow, 1986).
2. A. A. Emel'yanov and G. M. Kassirov, Izv. Vyssh. Uchebn. Zaved., Fiz., No. 9, 105 (1976).
3. G. K. Kartsev, G. A. Mesyats, D. I. Proskurovskiĭ, *et al.*, Dokl. Akad. Nauk SSSR **192** (2), 309 (1970) [Sov. Phys. Dokl. **15**, 475 (1970)].
4. *Handbook of Physical Quantities*, Ed. by I. S. Grigoriev and E. Z. Meilikhov (Énergoatomizdat, Moscow, 1991; CRC Press, Boca Raton, 1997).
5. A. A. Emel'yanov, Prib. Tekh. Éksp., No. 5, 68 (1997).
6. A. A. Emel'yanov, Prib. Tekh. Éksp., No. 2, 109 (1996).
7. I. I. Kalyatskiĭ, G. M. Kassirov, and G. V. Smirnov, Prib. Tekh. Éksp., No. 4, 84 (1974).

Translated by P. Pozdeev

Technical Physics Letters, Vol. 29, No. 1, 2003, pp. 41–42. Translated from Pis'ma v Zhurnal Tekhnicheskoĭ Fiziki, Vol. 29, No. 2, 2003, pp. 1–5.
Original Russian Text Copyright © 2003 by Samsonov.

Experimental Determination of the Energy of a Gas Vortex Motion during Autooscillations in a Free Convective Flow

V. P. Samsonov

Surgut State University, Surgut, Russia
e-mail: samsonov@surgu.wsnet.ru
Received July 26, 2002

Abstract—Free convective gas flow in a "singing" flame and in a Rijke tube was studied in the case of small Reynolds numbers (Re < 1000). A method for determining the dissipated gas flow energy is proposed, which is based on the measurement of displacements of a resonator tube from the position of mechanical equilibrium upon a change from stationary to autooscillatory flow regime, which is accompanied by the spontaneous formation of vortex structures. It is shown that the vortex motion in the gas leads to a decrease in thermal flux in the tube cross section. The energy of rotational motion as a function of the heat-source power exhibits a hysteresis behavior. *© 2003 MAIK "Nauka/Interperiodica".*

The formation of vortices in a gas flow in some heat exchangers and combustion chambers leads to oscillations in the intensity of the heat and mass transfer and in the combustion rate. A classical example of such autooscillatory systems is offered by the "singing" flame and the Rijke tube [1]. Afanas'ev *et al.* [2, 3] showed, by using interference and holographic methods of flow visualization, that the excitation of acoustic oscillations in the singing flame is related to the self-organization of vortex structures. However, the lack of data on the energy of rotational motions in a gas flow hinders elucidation of the role played by vortex structures in the mechanism of feedback between oscillations in the flow velocity and the heat evolution rate.

As follows from the results obtained in [3], the vortex structure represents a sequence of toroidal vortices arranged downstream from the heat source to the upper tube end. According to the Richardson annular effect [4], a maximum of the rotational motion velocity occurs near the tube wall. The vortex motion gives rise to a viscous friction force (periodically changing direction) at the internal surface of the wall.

A product of the average friction force by the velocity of rotational motion of the gas is the kinetic energy dissipated per unit time [5]:

$$\pi R^2 L\nu\sqrt{\omega\nu/2} = W/T. \quad (1)$$

Here, R and L are the internal diameter and length of the resonator tube, respectively; ν and ω are the linear velocity and circular frequency of the rotational motion, respectively; W is the kinetic energy of rotational motion; and T is the period of oscillations. Upon excitation of oscillations in the gas and the formation of vortices, the resulting force of viscous friction applied to the tube wall surface will decrease. If the resonator tube is fixed in an immobile base and occurs in a mechanical equilibrium under the action of an external elastic force, friction force, and force of gravity, a change in the regime of gas glow in the tube will lead to a shift of the position of equilibrium. In this case, a decrease in the potential energy of the resonator tube in the gravitational field is equal to the energy of rotational motion of the gas in the vortex structure.

The experimental setup comprised a base on which an immobile cylindrical tube with an internal diameter of 0.085 m and a length of 1.8 m was vertically mounted. A mobile cylindrical sleeve with a length of 2 m and an external diameter of 0.08 m was suspended on a spring inside the tube. The external corrugated walls of the sleeve were made of paper with glue. The internal sleeve surface was made of aluminum foil. The corrugated wall thickness was 5×10^{-3} m. The sleeve design ensured sufficient thermal stability and strength at a total mass of 0.137 kg. At one-quarter of the sleeve length from its lower edge was a heat source representing either a diffuse propane torch or an electrical heater coil. The heat-source power could be varied from 10 to 120 W. The torch had an internal nozzle diameter of 4×10^{-3} m; the propane flow velocity at the nozzle edge was varied from 0.1 to 0.3 m/s. The voltage applied to the electrical heater coil was varied from 20 to 40 V, whereby the current changed from 0.5 to 3 A. Propane was supplied through a displacement gas meter and the flow rate was determined from the pressure drop across a calibrated capillary, while the velocity of combustion products at the upper edge of the sleeve was measured by a rotameter. The temperature of the combustion products was measured to within 10°C using a thermo-

1063-7850/03/2901-0041$24.00 © 2003 MAIK "Nauka/Interperiodica"

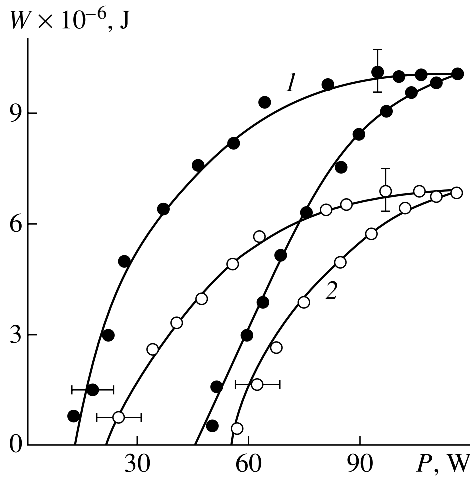

Hysteresis in the plots of the energy W of rotational motion of the gas versus the power P of a heat source representing a (*1*) propane torch flame and (*2*) electrical heater coil.

couple mounted at the center of the sleeve, at a distance of 0.1m from its upper edge.

At a heat-source power of $P < 30$ W, the gas flow caused by free convection inside the sleeve was stationary and laminar. The sleeve shifted upward inside the outer tube under the action of the elastic force of the spring and the force of viscous friction. The upward shift of the sleeve relative to the equilibrium position (occupied in the absence of the gas flow) changed, depending on the heat source power, in the range from $h_1 \approx 3.0 \times 10^{-3}$ to 30.0×10^{-3} m. The excitation of autooscillations in the gas resulted in a downward shift of the sleeve by $\Delta h = h_1 - h_2 \approx 3.0 \times 10^{-3}$–$20.0 \times 10^{-3}$ m. In order to increase the accuracy of measurement of the h_1 and h_2 shifts, the sleeve was suspended on a spring with a rigidity coefficient of $k \leq 0.14$ N/m.

The intrinsic frequency of the gas column in the sleeve was 90 Hz. As the heat source power increased, an increment in the gas velocity oscillation amplitude exceeded the constant component, which resulted in the flame breaking and quenching. However, even in this case no oscillations in the sleeve shift were observed as a result of its inertia. The gas in the adjacent vortex cells rotates in opposite directions, and hence, the energy of the rotational motion equals the work of the viscous friction force spent to change the potential energy of the sleeve: $W = k\Delta h^2$.

The results of determining the energy W of rotational motion of the gas as a function of the heat source power P are presented in the figure, where curves *1* and *2* correspond to the cases of singing flame and Rijke tube, respectively. The autooscillations are excited at a heat source power of 45 and 55 W. In both cases, the maximum energy of autooscillations is achieved at a heat source power of ≈120 W. As can be seen in the figure, a decrease in the power leads to a hysteresis in $W(P)$. This behavior is probably related to the fact that the vortex flow is more stable than translational motion. The average linear gas velocity in the vortex, as estimated from relation (1) using the measured values of W, exceeds the average translational velocity by a factor of 10–15.

It was established that the vortex structure formation is accompanied by a decrease in the average temperature of the gas at the resonator tube output by $\Delta t = 45°$C. This estimate was obtained from the energy balance $c_P \rho \nu S \Delta t = W/T$, where c_P and ρ are the specific heat and density of the gas, respectively, and S is the sleeve cross section. The results of calculations showed that the estimate obtained for Δt agrees in order of magnitude with the experimentally measured value. Therefore, the gas motion in the vortex structure observed increases the rate of heat exchange at the sleeve walls. The laws of temperature and energy variation are the same in the cases of singing flame and Rijke tube. This result suggests that the main mechanism maintaining the oscillations is of a hydrodynamic nature.

REFERENCES

1. *Nonsteady Flame Propagation*, Ed. by G. H. Markstein *et al*. (Pergamon, Oxford, 1964; Mir, Moscow, 1968).
2. V. V. Afanas'ev, S. A. Abrukov, N. I. Kidin, *et al.*, Fiz. Goreniya Vzryva **31** (4), 34 (1995).
3. V. V. Afanas'ev, Fiz. Goreniya Vzryva **35** (4), 43 (1999).
4. H. Schlichting, *Boundary Layer Theory* (McGraw-Hill, New York, 1968; Nauka, Moscow, 1974).
5. L. D. Landau and E. M. Lifshitz, *Fluid Mechanics* (Nauka, Moscow, 1986; Pergamon Press, Oxford, 1987).

Translated by P. Pozdeev

Technical Physics Letters, Vol. 29, No. 1, 2003, pp. 43–46. Translated from Pis'ma v Zhurnal Tekhnicheskoĭ Fiziki, Vol. 29, No. 2, 2003, pp. 6–13.
Original Russian Text Copyright © 2003 by Stognij, Novitskii, Stukalov.

Separate Cobalt–Copper Interface Smoothening under the Action of Low-Energy Argon Ion Bombardment

A. I. Stognij, N. N. Novitskii, and O. M. Stukalov

"Zavod Transistor" State Unitary Enterprise, "Integral" Corporation, Minsk, Belarus

Institute of Solid State and Semiconductor Physics, National Academy of Sciences of Belarus, Minsk, Belarus

e-mail: stognij@ifttp.bas-net.by

Received August 9, 2002

Abstract—Multilayer film structures of the types "buffer gold layer (20 nm)–copper (x nm)–cobalt (y nm)–protective gold layer (10 nm)" and "buffer gold layer (20 nm)–cobalt (y nm)–copper (x nm)–protective gold layer (10 nm)" with $x + y \approx 6$ nm obtained by ion beam deposition in vacuum were studied. It was established that the smoothest surface is obtained for a structure of the second type in which the cobalt layer prior to copper deposition was additionally irradiated with a beam of argon ions at an energy below the threshold energy of sputtering in the common vacuum deposition cycle. Additional irradiation with a mixture of argon and helium ions under analogous conditions leads to the formation of a less smooth structure. It is concluded that the cobalt–copper interface is smoothened as a result of multiple collisions of the low-energy argon ion with cobalt atoms during the former ion stopping within two to three of uppermost atomic layers of the target.
© 2003 MAIK "Nauka/Interperiodica".

Multilayer film structures comprising alternating nanodimensional layers of ferromagnetic and nonmagnetic metals are extensively studied since these systems have been found to possess some properties (e.g., giant magnetoresistance) not typical of films composed of a single metal [1, 2]. Of special importance for multilayer structures are problems related to the formation and properties of interfaces between adjacent metal layers. In particular, considerable attention in recent years has been paid to the influence of interface roughness on the properties of multilayer structures [3–5]. However, the investigations were mostly performed under ultrahigh vacuum (UHV) conditions. This circumstance restricts the possibilities of searching for the methods of action upon an interface in the course of layer deposition in order to obtain atomically smooth interfaces. Indeed, any additional equipment mounted inside a UHV chamber leads to increased gas evolution and/or introduces impurities into the system studied. As is known, metal films of sufficiently high quality can be obtained even under technological vacuum conditions ($p \leq 10^{-2}$ Pa), whereby the possibilities of using additional treatments in a common vacuum deposition cycle are significantly increased (to include ion implantation, irradiation with ion, electron, and laser beams, etc.).

Below we present the results of investigation of Au/Co/Cu/Au and Au/Cu/Co/Au structures in which Co/Cu and Cu/Co interfaces were modified by irradiation with a beam of helium and/or argon ions with energies below 30 eV.

The sample film structures were prepared using an ion beam deposition system described previously [6]. Arrangement of the main system units is schematically depicted in Fig. 1. Ion source *1* produced a beam of argon ions used for the sputtering of gold, cobalt, and copper targets mounted on a rotary holder *2*. The sputtered material was deposited onto BK-7 glass plates with dimensions of 10 × 20 mm, which were preliminarily polished by the method of sequential ion beam

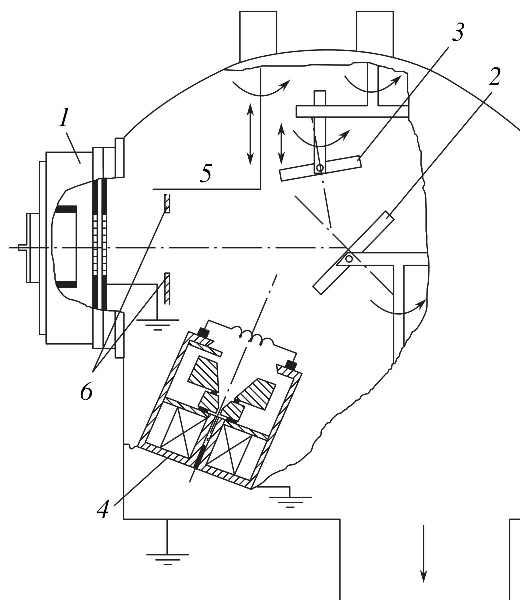

Fig. 1. A schematic diagram of the ion beam deposition setup: (*1*) sputter ion beam source; (*2*) target; (*3*) substrate holder; (*4*) low-energy ion beam source; (*5*) shutter; (*6*) diaphragm.

1063-7850/03/2901-0043$24.00 © 2003 MAIK "Nauka/Interperiodica"

sputter–deposition [6] to a subnanometer level of roughness. The substrates were mounted in a multipositional rotary holder *3.* Ion source *4* produced a low-energy beam of argon or argon and helium ions for the irradiation of Co/Cu and Cu/Co interfaces. Shutter *5* protected the substrate surface during preparation of the ion sources and targets. Diaphragm *6* limited the ion beam from source *1* to the target surface and provided for the autonomous operation of ion sources *1* and *4*.

The working chamber was evacuated with a turbomolecular pump to a residual pressure not exceeding 10^{-3} Pa. The working pressure did not exceed 3×10^{-2} Pa. The low-energy ion beam current density was below 0.2 mA/cm^2 and the ion energy did not exceed 100 eV, while more than 80% of ions possessed energies below 30 eV. According to [7], this circumstance allows us to suggest that the sample surface sputtering by the low-energy ion beam is negligibly small. When helium ions were admitted into ion source *4*, it was assumed (based on estimates of the partial pressures of argon and helium and known peculiarities of the ionization process in these gases) that the fraction of helium ions in the assisting beam does not exceed 80%, while that in the sputtering beam is below 20%. Average velocities of deposition for gold, copper, and cobalt were 25, 15, and 10 nm/min, respectively.

The sample surface morphology was studied and the film thicknesses evaluated with the aid of a Femtoskan-001 atomic-force microscope (AFM) (Advanced Technology Center, Moscow State University) with a 5 × 5 μm scanned field area. The AFM was operated in a contact regime using silicon cantilevers (MicroMash, www.spmtips.com, Estonia). The surface resistance of the films was measured using the four-point-probe technique.

Figure 2a shows an AFM image of the surface of a gold film with a thickness of 20 nm, as estimated by the depth of a scratch made by a cotton fiber. The surface resistance of this film was $R \leq 5$ Ω/□. Multilayer film structures of the type gold (buffer layer, 20 nm)–copper (x nm)–cobalt (y nm)–gold (protective layer, 10 nm) with $x + y \approx 6$ nm possessed a surface resistance above 7 Ω/□. It was established that the maximum increment in the resistance was related to deposition of the cobalt layer. Film structures of the type gold (20 nm)–cobalt (y nm)–copper (x nm)–gold layer (10 nm) with $x + y \approx$ 6 nm possessed a surface resistance between 4.5 and 7 Ω/□ for the copper layer thickness varied from 4 to 2 mm.

These results do not contradict the existing notions about the peculiarities of the deposition of thin metal films. In particular, it was pointed out [8] that using gold as a buffer material prevents the formation of a natural oxide layer on the bottom surface of the next metal layer; in preparing multilayer systems on gold, it is recommended to deposit the most active metal (in our case, cobalt) as the first layer. Taking into account these recommendations, the subsequent investigation was performed for the samples with cobalt underlying copper, in which lower surface resistance and more perfect structure were achieved under the given experimental conditions.

It was found that the surface resistance of samples of the type gold (20 nm)–cobalt (y nm)–copper (x nm)–gold layer (10 nm) with $x + y \approx 6$ nm, in which the cobalt layer prior to copper deposition was additionally irradiated for 20–30 s with a beam of argon ions, was somewhat lower as compared to the resistance of analogous samples prepared without this additional treatment under otherwise equal conditions. Figures 2b–2d show the AFM images of the structures gold (20 nm)–cobalt (2 nm)–copper (4 nm)–gold (10 nm) prepared without additional ion irradiation (Fig. 2b) and with such irradiation for 20 s using argon ions (Fig. 2c) and a mixed beam of argon and helium ions (Fig. 2d). As can be seen, the surface morphology changes depending on the conditions of additional irradiation. The sample image in Fig. 2b reveals relatively coarse inhomogeneities. The structure prepared using irradiation with low-energy argon ions (Fig. 2c) exhibits the smoothest appearance. The surface morphology of a structure involving the cobalt/copper interface irradiated with a mixture of argon and helium (Fig. 2d) seems to be intermediate between the previous two. The surface inhomogeneities observed in Fig. 2d are characterized by more rounded shapes and smeared boundaries as compared to those in Fig. 2b. Since the deposition conditions differed only in the part of the cobalt/copper interface formation, all other conditions being identical, the distinct features of the surface morphology reflect peculiarities of the state of the cobalt/copper interface.

The above results allow us to conclude that additional irradiation of the cobalt surface with a beam of low-energy argon ions result in smoothening of the cobalt/copper interface. In explaining this experimental fact, one must take into account that we used the substrates with especially smooth surfaces and that the gold films possessed a smooth and chemically inert surface (Fig. 2a). Consider the model of close-packed balls [9] for the structure with a 2-nm-thick cobalt layer below copper. Let this cobalt layer be structurally ordered and contain more than six monoatomic layers. Let the copper overlayer also be structurally ordered and contain more that ten monoatomic layers. A mismatch of the structures of these layers at the interface is the main factor determining the surface morphology of the whole multilayer structure, which exhibits inhomogeneities of a regular oval shape with an average transverse size on the order of 20 nm and a height of about 3 nm, at an rms surface roughness below 1.1 nm (Fig. 2b).

Irradiation of the cobalt layer surface with a dense beam of argon ions possessing an energy below the sputter threshold results in that each cobalt atom in the two or three uppermost monoatomic layers experiences multiple collisions with argon atoms, with the energy

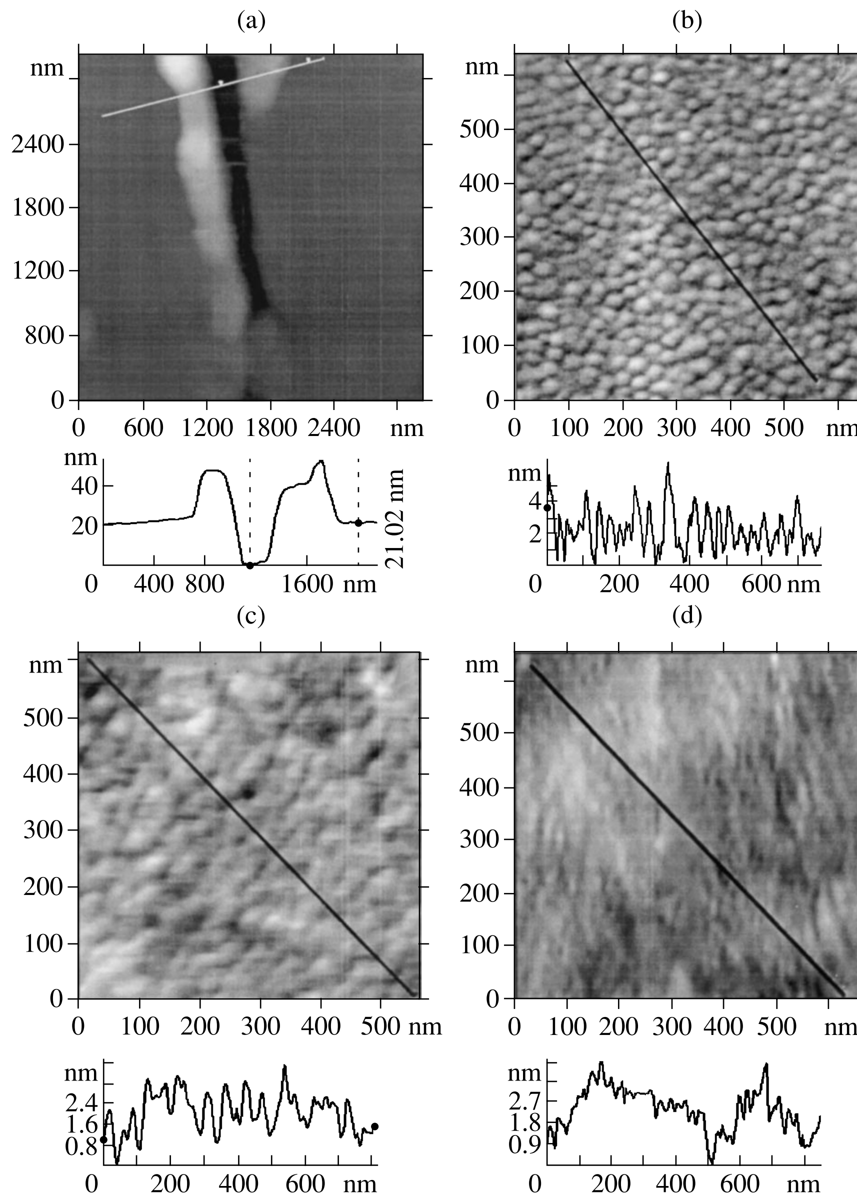

Fig. 2. AFM images of the surface of gold (20 nm)–cobalt (2 nm)–copper (4 nm)–gold (10 nm) structures and the surface profiles measured along the lines indicated on the former images: (a) gold surface with a scratch used for calibration of the deposition rate; (b) Au/Co/Cu/Au structure prepared without additional irradiation; (c) Au/Co/Cu/Au structure prepared with the Co surface irradiated by argon ions; (d) Au/Co/Cu/Au structure prepared with the Co surface irradiated by a mixture of helium (above 80%) and argon (below 20%) ions.

transferred in each collision exceeding the cobalt–cobalt bond energy. According to estimates obtained using the SRIM [www.srim.org] program, the mean projected range of argon ions with an energy below 30 eV in cobalt does not exceed 0.4 nm. Therefore, the structural disordering can take place only on the surface of the cobalt layer. The subsequent matching of the structurally disordered cobalt surface to the deposited copper layer leads to the formation of a multilayer structure possessing a smoother surface (Fig. 2c). Indeed, the surface of the whole structure obtained after irradiation of the cobalt layer became more homogeneous and smooth, the rms surface roughness decreasing to less than 0.64 nm.

Irradiation of the cobalt layer with helium ions, in contrast to the case of argon, does not produce disordering of the surface layer of cobalt because the range of helium ions according to the SRIM estimate is 1.2 nm (i.e., comparable to the monolayer thickness) and the energy lost as a result of stopping light, low-energy helium ions is distributed approximately uniformly in the depth of the layer. The energy transferred in each collision from a helium to a cobalt atom does not exceed the cobalt–cobalt binding energy. In connection

with this, the surface of the multilayer structure in Fig. 2d is characterized by an rms surface roughness of 0.96 nm, which is close to the value for the initial film structure. The intermediate appearance of this surface in comparison with those in Figs. 2b and 2c is probably related to the fact that the beam of helium ions contained about 20% of argon ions.

Thus, the results of out experiments suggest that additional irradiation of the uppermost atomic layers of a preceding metal layer with low-energy ions prior to deposition of the subsequent metal in the course of the formation of a multilayer structure is a promising method for obtaining structures with atomically smooth interfaces.

REFERENCES

1. M. N. Baibich, J. M. Broto, F. Fert, *et al.*, Phys. Rev. Lett. **61**, 2472 (1988).
2. B. Dieny, J. Magn. Magn. Mater. **136**, 335 (1994).
3. G. Palasantzas, Y.-P. Zhao, J. Th. M. Hosson, and G.-C. Wang, Physica B **283**, 199 (2000).
4. X. W. Zhou and H. N. G. Wadley, Surf. Sci. **487**, 159 (2001).
5. A. I. Stognij, N. N. Novitskii, and O. M. Stukalov, in *New Magnetic Materials for Microelectronics. A Collection of Papers of XVIIIth Int. Seminar-Workshop (24–28 June, 2002)* (Moscow, 2002), pp. 303–305.
6. A. I. Stognii, N. N. Novitskii, and O. M. Stukalov, Pis'ma Zh. Tekh. Fiz. **28** (1), 39 (2002) [Tech. Phys. Lett. **28**, 17 (2002)].
7. V. S. Smentkowski, Prog. Surf. Sci. **64**, 1 (2000).
8. *Thin Films: Interdiffusion and Reactions*, Ed. by J. M. Poate, K. N. Tu, and J. V. Mayer (Wiley, New York, 1978; Mir, Moscow, 1982).
9. C. Kittel, *Introduction to Solid State Physics* (Wiley, New York, 1976; Nauka, Moscow, 1978).

Translated by P. Pozdeev

Technical Physics Letters, Vol. 29, No. 1, 2003, pp. 47–50. Translated from Pis'ma v Zhurnal Tekhnicheskoĭ Fiziki, Vol. 29, No. 2, 2003, pp. 14–22.
Original Russian Text Copyright © 2003 by Bormontov, Bryazgunov, Lezhenin.

An Analytical Model of the Diffusion Redistribution of Ion-Implanted Impurity in the Gate Region of a MOS Transistor

E. N. Bormontov, Yu. I. Bryazgunov, and V. P. Lezhenin
Voronezh State University, Voronezh, Russia
e-mail: phme22-1@main.vsu.ru
Received July 29, 2002

Abstract—The problem of a diffusion redistribution of an ion-implanted impurity in the silicon dioxide–silicon system in the course of thermal annealing is solved with allowance for the difference in the parameters of the two media and for the impurity segregation at the interface. *© 2003 MAIK "Nauka/Interperiodica".*

The wide use of ion implantation in microelectronic technology determines the need for developing theoretical models of metal–oxide–semiconductor (MOS) elements of integrated circuits with allowance for an inhomogeneous distribution of the implanted impurity—a factor significantly influencing the electric parameters of MOS structures. Using analytical models such as that presented in [1], it is possible to obtain explicit expressions for the working characteristics of MOS devices. However, the accuracy of such models is insufficient because of rough approximations used for describing a real impurity profile (typically, in the form of a steplike or barrier function). On the other hand, numerical models employing more realistic profiles involve a large number of poorly determined parameters and, hence, are inapplicable for selecting technological regimes for the formation of ion-doped MOS elements of integrated circuits.

The "technological transparency" of a model can be retained and the computation time reduced using the approach based on the semianalytical modeling of ion-doped MOS transistors [2–4]. This method usually employs a Gauss approximation, which is known to provide for a good description of the impurity distribution immediately upon implantation [5]. However, use of this approximation in semianalytical models requires physical justification because the postimplantation thermal treatments (required for spreading and activating the impurity) lead to a diffusion redistribution of the implant. Below, we will analyze such a redistribution taking place in a SiO_2–Si system with allowance for the difference in parameters of the two media and for the impurity segregation at the interface. This analysis allows one to establish the conditions under which the resulting impurity profile can be approximated by a superposition of modified Gauss distributions.

The MOS transistor technology usually employs ion doping with boron, phosphorus, and arsenic. In order to eliminate the channeling effects and control the ion range, the implantation is typically performed through a thin amorphous oxide layer, the function of which is usually performed by the gate insulator. Since the SiO_2–Si system represents a two-layer target with close atomic numbers and masses of the components, we can use the simple Ishivara model [6], according to which the ion-implanted impurity concentration profile $N_0(x)$ immediately after the ion bombardment is described by the Gauss function

$$N_0(x) = N_b + \frac{D_i}{\sqrt{2\pi}\Delta R_{PSi}} \exp\left[-\frac{(x_c - x)^2}{2\Delta R_{PSi}^2}\right], \quad (1)$$

where N_b is the base impurity concentration in the semiconductor substrate, D_i is the implanted ion dose, ΔR_{PSi} is the rms deviation of the projected ion range in silicon, $x_c = (R_{PSiO_2} - d_{SiO_2})\Delta R_{PSi}/\Delta R_{PSiO_2}$ is the centroid of the implanted impurity, R_{PSiO_2} is the mean projected ion range in silicon oxide, d_{SiO_2} is the gate oxide thickness, and ΔR_{PSiO_2} is the rms deviation of the projected ion range in silicon oxide.

In order to determine the resulting depth-concentration profile of the implanted impurity with allowance for the diffusion and segregation phenomena at the oxide–silicon interface, it is necessary to solve the equation of diffusion (Fick's equation),

$$\frac{\partial N}{\partial t} = D\frac{\partial^2 N}{\partial x^2}, \quad (2)$$

where N is the impurity concentration and D is the diffusion coefficient.

Since ion implantation into the gate regions of MOS devices is performed through the oxide layer with

1063-7850/03/2901-0047$24.00 © 2003 MAIK "Nauka/Interperiodica"

a thickness on the order of R_{PSiO_2}, a maximum in the implant distribution (x_c) occurs near the oxide–semiconductor interface. The exact profile is determined by solving Eq. (2) in two regions: semiconductor and oxide. However, since the bandgap width of SiO_2 is about 8 eV, the dopants typically used for implantation (boron, phosphorus, arsenic, and antimony) are inactive at a normal working temperature of MOS devices (~300 K) and, hence, the corresponding charge is zero and does not enter the Poisson equation. Therefore, modeling the MOS devices requires only knowledge of the impurity distribution profile in the semiconductor.

In the case of short-time low-temperature annealing used in the final stage of MOSIC technology for the activation of impurities implanted at small doses (for correcting the threshold voltage of an enhancement-mode MOS transistor), the impurity profile changes rather insignificantly. In this case, the impurity diffusion length is $L = \sqrt{D_{Si}t} \ll \Delta R_{PSi}$ (D_{Si} is the impurity diffusion coefficient in silicon and t is the annealing duration) and, hence, the diffusion redistribution can be considered as proceeding in a homogeneous and infinite medium. The solution to Fick's equation (2) with an initial condition in the form of the Gauss distribution (1) also represents a Gauss function with the modified standard deviation $\sigma = \sqrt{\Delta R_{PSi}^2 + 2Dt}$ [4]:

$$N(x, t) = N_b + \frac{D_i}{\sqrt{2\pi}\sigma}\exp\left[-\frac{(x_c - x)^2}{2\sigma^2}\right]. \quad (3)$$

The embedded channel formation in a depletion-mode transistor is provided by long-time high-temperature diffusion annealing. In this case, the diffusion length L of the impurity can exceed ΔR_{PSi} and, therefore, the resulting profile has to be determined with allowance for inhomogeneity of the medium.

Since the gate insulator thickness (20–50 nm) is significantly greater than the diffusion lengths of implants encountered in modern MOS technology ($L = \sqrt{D_{SiO_2}t} < 10$ nm, where D_{SiO_2} is the impurity diffusion coefficient in silicon oxide), the solution to Fick's equation can be found assuming the insulator to be semiinfinite; the same assumption is valid for a semiconductor region with a thickness on the order of several hundred microns. As a result, Fick's equation with the corresponding boundary conditions for the system under consideration takes the following form:

$$\begin{cases} \dfrac{\partial N_i}{\partial t} = D_i\dfrac{\partial^2 N_i}{\partial x^2}, & x \le 0; \\ \dfrac{\partial N_s}{\partial t} = D_s\dfrac{\partial^2 N_s}{\partial x^2}, & x \ge 0. \end{cases} \quad (4)$$

$$\begin{cases} D_i\dfrac{\partial N_i}{\partial x} = D_s\dfrac{\partial N_s}{\partial x}, & x = 0, \quad t > 0; \\ \mu N_i = N_s, & x = 0, \quad t > 0; \\ N_i = 0, & x \longrightarrow -\infty, \quad t \ge 0; \\ N_s = 0, & x \longrightarrow +\infty, \quad t \ge 0. \end{cases} \quad (5)$$

Here, μ is the coefficient of impurity segregation at the oxide–semiconductor interface and subscripts "i" and "s" indicate the quantities referred to the insulator (oxide) and semiconductor, respectively.

The initial condition to Eqs. (4) and (5) is selected in the form of the Gauss impurity distribution (1) according to the Ishivara model. As noted above, the gate insulator thickness in modern MOS devices does not exceed 50 nm. The characteristic energies of implanted ions are 40–60 keV for boron and about 100 keV for phosphorus. For these energies, a maximum in the impurity profile (x_c) occurs at a depth exceeding $1.5\Delta R_{PSi}$ and, hence, almost the entire implant (>95%) falls into silicon. Since the oxide contains less than 5% of the implant, we may neglect the initial distribution of impurity in this region and find the resulting profile by solving the system of Eqs. (1), (4), and (5) only in a semiconductor.

Equations (4) and (5) represent a boundary-value problem of the third kind for a parabolic equation. The solution to this problem can be represented as the sum of a solution $N_1(x, t)$ to the initial value problem and a solution $N_2(x, t)$ to the boundary value problem:

$$N(x, t) = N_1(x, t) + \gamma N_2(x, t), \quad (6)$$

where $\gamma = (\mu - \sqrt{D_{SiO_2}/D_{Si}})/(\mu + \sqrt{D_{SiO_2}/D_{Si}})$ is the coefficient describing the "interface effect."

The problem under consideration can be solved by the method of source function [7], which yields

$$N_1(x, t) = \frac{1}{2\sqrt{\pi Dt}}\int_0^\infty N_0(\xi)\exp\left[-\frac{(x-\xi)^2}{4Dt}\right]d\xi, \quad (7)$$

$$N_2(x, t) = \frac{1}{2\sqrt{\pi Dt}}\int_0^\infty N_0(\xi)\exp\left[-\frac{(x+\xi)^2}{4Dt}\right]d\xi. \quad (8)$$

Substituting the initial distribution $N_0(\xi)$ in the form of Eq. (1) into expressions (7) and (8), we obtain

$$N(x, t) = \frac{N_b}{2}\left[1 + \mathrm{erf}\left(\frac{x}{2\sqrt{Dt}}\right)\right] + \frac{D_i}{\sqrt{2\pi}\sigma}\exp\left[-\frac{(x_c - x)^2}{2\sigma^2}\right]$$

$$\times\left\{\frac{1}{2}+\frac{1}{2}\mathrm{erf}\left(\frac{\frac{x_c}{\Delta R_{PSi}^2}+\frac{x}{2Dt}}{2\sqrt{\frac{1}{2\Delta R_{PSi}^2}+\frac{1}{4Dt}}}\right)\right\}$$

$$+\gamma\left[\frac{N_b}{2}\left[1-\mathrm{erf}\left(\frac{x}{2\sqrt{Dt}}\right)\right]+\frac{D_i}{\sqrt{2\pi}\sigma}\exp\left[-\frac{(x_c+x)^2}{2\sigma^2}\right]\right. \tag{9}$$

$$\left.\times\left\{\frac{1}{2}+\frac{1}{2}\mathrm{erf}\left(\frac{\frac{x_c}{\Delta R_{PSi}^2}-\frac{x}{2Dt}}{2\sqrt{\frac{1}{2\Delta R_{PSi}^2}+\frac{1}{4Dt}}}\right)\right\}\right],$$

where $\sigma = \sqrt{DR_{PSi}^2 + 2Dt}$ is the "modified" standard deviation.

Let us analyze the relationship obtained. The solution represents the sum of two functions, $N_1(x, t)$ and $N_2(x, t)$, both being symmetric relative to the oxide–silicon interface. Note that the second function enters (9) with a coefficient γ that falls within the interval [–1; 1]. Since the profile peaks in the region of the semiconductor ($x_c > 0$), we may conclude that $N_1(x, t) > N_2(x, t)$ for $x > 0$ and $N_1(x, t) = N_2(x, t)$ at $x = 0$ (Fig. 1). Let us denote the first and second factors in braces in Eq. (9) by $f_1(x, t)$ and $f_2(x, t)$ and the corresponding Gauss functions by $N_1^*(x)$ and $N_2^*(x)$, respectively. Note that the pairs of functions $N_1^*(x, t)$ and $N_2^*(x, t)$, as well as $f_1(x, t)$ and $f_2(x, t)$, are symmetric relative to the oxide–silicon interface.

The functions $f_1(x, t)$ and $f_2(x, t)$ depend on the initial distribution parameters x_c and ΔR_{PSi} and on the impurity diffusion length $L = \sqrt{D_{Si}t}$ in silicon. For the embedded channel formation, the implanted impurity is usually subjected to two-stage annealing under the following conditions. For boron (p-channel): first anneal, $T_1 = 950°C$, $t_1 = 70$ min; second anneal, $T_2 = 1000°C$, $t_2 = 20$ min; for phosphorus (n-channel): $T_1 = 950°C$, $t_1 = 100$ min; $T_2 = 1000°C$, $t_2 = 30$ min. The diffusion lengths of both boron and phosphorus in silicon is $L = \sqrt{D_1t_1 + D_2t_2} \approx 0.065$ µm. The typical values of x_c and ΔR_{PSi} for these dopants are 0.1 and 0.05 µm, respectively. The function $f_1(x)$ asymptotically tends to 1 as x increases and is greater than 0.93 for $x > 0$. Therefore, this quantity can be approximately taken equal to unity with an error of not greater than 7%. The function $N_2(x)$

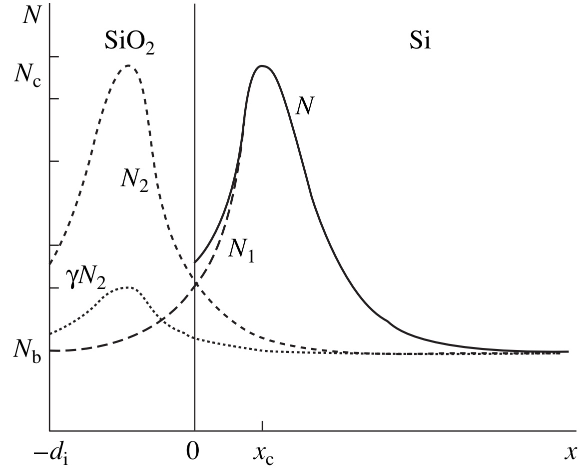

Fig. 1. Plots of the functions $N(x)$, $N_1(x)$, $N_2(x)$, and $\gamma N_2(x)$ for ion implantation and thermal treatment parameters typical of boron ($x_c = 0.1$ µm; $\Delta R_P = 0.05$ µm; $L = 0.065$ µm; $\gamma = 0.1$).

represents a product of the function $f_2(x)$ and the Gauss function $N_2^*(x)$ rapidly decaying with increasing x (Fig. 1). Therefore, the contribution of $N_2(x)$ to the total concentration $N(x)$ rapidly decreases in depth of the semiconductor and, hence, we can take this function also equal to unity without large loss of accuracy. A change in the base impurity concentration N_b as a result of segregation is significant only in the vicinity of the interface, to within a distance on the order of the diffusion length L. However, we may neglect this effect because the concentration of the impurity implanted in this region exceeds N_b by at least one order of magnitude.

The resulting dopant profile after the thermal treatment of an ion-implanted silicon is as follows:

$$N(x,t) = N_b + \frac{D_i}{\sqrt{2\pi}\sigma}\exp\left[-\frac{(x_c-x)^2}{2\sigma^2}\right] + \gamma\frac{D_i}{\sqrt{2\pi}\sigma}\exp\left[-\frac{(x_c+x)^2}{2\sigma^2}\right]. \tag{10}$$

Expression (10) already represents a double integrable function, but it can be further simplified by taking into account the values of the coefficient γ for real thermal treatments. According to the formula $\gamma = (\mu - \sqrt{D_{SiO_2}/D_{Si}})/(\mu + \sqrt{D_{SiO_2}/D_{Si}})$, the value of γ falls within the interval from –1 to 1 (the limits corresponding to completely open and closed interfaces) [5]. It is commonly accepted [8] that the Si–SiO_2 interface is open for boron ($\gamma = -1$) and closed for phosphorus ($\gamma = 1$). However, since the diffusion and segregation coefficients depend on temperature, the value of γ is also temperature-dependent [9]. The temperature

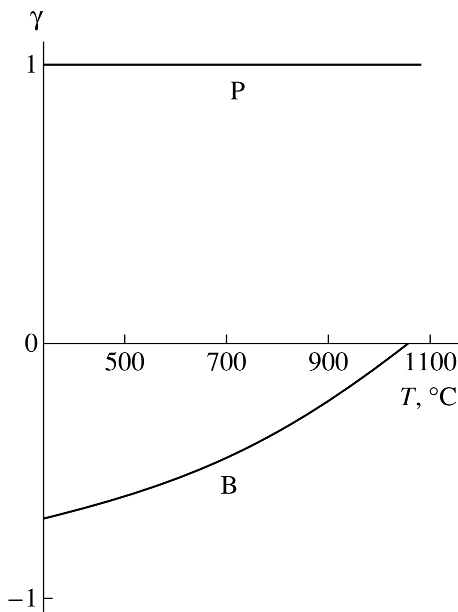

Fig. 2. Temperature dependence of the coefficient γ ("interface effect") for boron and phosphorus in silicon.

dependence of the coefficient γ for boron is presented in Fig. 2, from which it is seen that $\gamma \le 0.1$ at temperatures above 950°C.

Thus, taking into account that $\gamma \le 0.1$, we obtain the following final expression describing the distribution of boron in silicon after a prolonged thermal treatment (which is accurate to within an error not exceeding 10%) [10]:

$$N(x, t) = N_b + \frac{D_i}{\sqrt{2\pi}\sigma}\exp\left[-\frac{(x_c - x)^2}{2\sigma^2}\right]. \qquad (11)$$

This expression looks exactly like Eq. (3), but the standard deviation σ in the case of a prolonged thermal treatment is determined by the treatment parameters (annealing temperature and duration determining the diffusion length of boron in silicon), rather than by the ΔR_{PSi} value.

In contrast to the case of boron, the coefficient of phosphorus segregation at the oxide–silicon interface $Si–SiO_2$ – $\mu \gg \sqrt{D_{SiO_2}/D_{Si}}$ at any temperature [8]. Therefore, the interface effect coefficient is virtually independent of temperature and approximately equal to unity, so that approximate formula (11) is inapplicable for describing the phosphorus distribution near the interface and has to be replaced by expression (10).

Thus, in most practically important cases, the dopant profile after annealing is described by a doubly integrable function convenient for the modeling of MOS devices. It should be emphasized that selection of the Gauss distribution to approximate the dopant profile in our model is not accidental. Although the real implant profiles are somewhat asymmetric and more adequately described by the functions with moments above second-order (e.g., by the Pearson-IV function), the use of such approximations in semianalytical models is hindered by the impossibility of integrating the Poisson equation in terms of analytical and special functions. At the same time, the level of accuracy provided by the Gauss function approximating the implant profile is quite sufficient for modeling the electrical characteristics of MOS devices as confirmed by our experimental data [3, 4].

REFERENCES

1. S. Sze, *Physics of Semiconductor Devices* (Wiley, New York, 1981; Mir, Moscow, 1984).
2. T. Yu. Krupkina, Izv. Vyssh. Uchebn. Zaved., Radioélektron. **28** (12), 31 (1985).
3. E. N. Bormontov and V. P. Lezhenin, Mikroélektronika **24** (5), 343 (1995).
4. E. N. Bormontov, V. P. Lezhenin, and I. V. Sai, Mikroélektronika **26** (1), 38 (1997).
5. H. Ryssel and I. Ruge, *Ionenimplantation* (Teubner, Stuttgart, 1978; Nauka, Moscow, 1983).
6. *Ion Implantation in Semiconductors*, Ed. by H. Ishivara *et al.* (Plenum Press, New York, 1975).
7. N. N. Tikhonov, *Equations of Mathematical Physics* (Dover, New York, 1963; Gostekhizdat, Moscow, 1953).
8. A. N. Bubennikov, *Modeling Integrated Microtechnologies, Devices, and Circuits* (Vysshaya Shkola, Moscow, 1989).
9. E. N. Bormontov and V. P. Lezhenin, *Proceedings of 1997 MRS Spring Meeting* (San Francisco, 1997), Symposium E, Abstract No. 10425.
10. E. N. Bormontov, V. P. Lezhenin, and V. V. Lukashkov, in *Proceedings of the 5th Int. Conf. on Simulation of Devices and Technologies* (Obninsk, 1996), p. 103.

Translated by P. Pozdeev

Technical Physics Letters, Vol. 29, No. 1, 2003, pp. 5–7. Translated from Pis'ma v Zhurnal Tekhnicheskoĭ Fiziki, Vol. 29, No. 1, 2003, pp. 13–17.
Original Russian Text Copyright © 2003 by Oganesyan.

A Radiation Generator Based on the Induced Transition Effect

S. G. Oganesyan
Laser Technology, Closed Joint-Stock Corporation, Yerevan, Armenia
Received July 2, 2002

Abstract—The possibility of generating electromagnetic radiation using a beam of free electrons in an empty resonator with ideally conducting walls is examined. It is shown that a regime can exist in which the number of photons in the resonator exhibits exponential growth, provided that the electron bunch length is sufficiently large. © *2003 MAIK "Nauka/Interperiodica".*

The phenomenon of radiation generated by a charged particle crossing an interface between two media, called transition radiation, was originally predicted by Ginzburg and Frank [1] and then studied in detail both theoretically and experimentally [2]. In the case of a particle moving in the field of an external monochromatic wave crossing the same interface, this effect acquires an induced character [3]. In an inhomogeneous medium, the external monochromatic field represents a combination of plane waves with the same frequency and arbitrary wave vectors. Among these waves, there always is a wave propagating at a velocity equal to that of the electron (similarly to the Vavilov–Cherenkov effect). This component can provide for an energy exchange between a particle and a field. A quantum-mechanical analysis showed that the radiation emission and absorption processes involve photons with different wave vectors. Based on this asymmetry, it is possible to amplify the electric signal by means of a dense electron beam [4]. It should be noted that the optimum amplification regime corresponds to the case when the effective electron bunch length is comparable with the size of the region of radiation formation [5].

In the case when an external signal source is absent, radiation emitted from a dense electron bunch can form due to a spontaneous noise [6]. In order to provide conditions for frequency selection, multiple amplification, and radiation energy accumulation, it is possible to introduce a resonator, that is, to use a free electron oscillator scheme. In this study, physical processes in such a transition radiation generator will be considered for the simplest case of an open planar resonator with ideally conducting walls (analysis of mirrors of more complicated shapes with allowance of the diffraction losses can be performed using the schemes proposed by Anan'ev [7]). Note that the resonator walls not only confine the radiation, but simultaneously serve as an inhomogeneity due to which the electrons generate radiation. Therefore, with a laser scheme of this type, there is no need for complicated elements such as an undulator [8].

A correct analysis of the radiation generated from spontaneous noise can be performed only within the framework of the quantum-mechanical approach. With neglect of the losses at the resonator walls, a field in the resonator can be represented as a combination of standing waves. The vector and scalar potentials of the rth mode polarized along the x axis are given by the expressions

$$A_x = \sqrt{\frac{4\pi\hbar c^2}{\omega_r V}}(c_r e^{-i\omega_r t} + c_r^* e^{i\omega_r t})\sin(k_r z), \quad \varphi = 0, \quad (1)$$

where

$$k_r = k_z = r\frac{\pi}{L}, \quad k_x = k_y = 0, \quad \omega_r = ck_r = r\frac{c\pi}{L}$$

are the wave vector components and frequency of the field; $r = 1, 2, \ldots$ is the mode number, L is the distance between resonator walls, and V is the resonator volume. In order to pass to the secondary quantization pattern, the c_r and c_r^* quantities have to be replaced by the photon production and annihilation operators $\hat{c}_r$ and $\hat{c}_r^+$, respectively. In what follows, consideration is restricted to a single (rth) mode corresponding to a frequency of $\hbar\omega_r \ll mc^2$. In this case, we can neglect the positron part in the free electron–positron field operator and write the latter as $\hat{\psi} = \hat{a}\psi_{p\sigma}$, where $\hat{a}$ is the electron annihilation operator and $\psi_{p\sigma}$ is a solution to the Dirac equation with a certain 4-moment p^μ and helicity σ [9]. Upon introducing the wave function of vacuum $|0\rangle$, we obtain the whole set of definitions necessary for an analysis of the evolution of the average number of photons $\overline{N}(t)$ in the resonator in terms of the Schrödinger equation.

1063-7850/03/2901-0005$24.00 © 2003 MAIK "Nauka/Interperiodica"

Upon solving the Schrödinger equation within the framework of the perturbation theory, we determine the amplitudes (and probabilities) of the photon emission and absorption for a mode with an arbitrary number of photons (N). By averaging these probabilities over the initial spin states of electrons and summing over the final states, we may construct an equation describing the rate of variation of the average number of photons in the given mode:

$$\frac{d\bar{N}}{dt} = Q + G\bar{N} - \alpha\bar{N}. \quad (2)$$

Here, the first term on the right-hand side describes spontaneous noise in the rth mode, the second term reflects the spontaneous emission and absorption processes, and the third term accounts for the resonator losses. For the losses in mirrors, $\alpha = -c\ln(r_1r_2)/2L$ (where r_1 and r_2 are the reflection coefficients of the corresponding mirrors). The quantities Q and G in Eq. (2) are given by the expressions

$$Q = \frac{32\pi^2}{3}\frac{c}{L}\rho_0 r_0 \frac{mc^2}{\hbar\omega_r}\frac{1-\beta_z^2}{\beta_z}|F(q)|^2\Big|_{q = \omega_r/v_z}, \quad (3)$$

$$G = \frac{32\pi}{3\sqrt{3}}\frac{c}{L}\frac{1}{r^2}\rho_0 r_0 L^2 \frac{(1-\beta_z^2)^{3/2}}{\beta_z^2}$$
$$\times\left[2k_r q|F(q)|^2 + k_r\left(q^2 - \frac{\omega_r^2}{c^2}\right)\frac{d|F|^2}{dq}\right]\Bigg|_{q = \omega_r/v_z}, \quad (4)$$

where $F(q)$ is the Fourier image of the field (1), ρ_0 is the electron density, r_0 is the classical electron density; and β_z and $\beta_x = \sqrt{2(1-\beta_z^2)/3}$ are the dimensionless electron velocity components. In calculating these quantities, it was assumed that the field scatter with respect to the wave vector q is large, which allows the angular and energy scatter of electrons in the beam to be ignored. It should be noted that the above expression for β_x was obtained as a result of optimization of Eq. (4).

If a system starts from the photon vacuum, then $N(t = 0) = 0$ and the solution to Eq. (2) takes the form of

$$\bar{N}(t) = \frac{Q}{G-\alpha}[\exp(G-\alpha)t - 1]. \quad (5)$$

Let us introduce a characteristic time of the rth resonator mode as

$$\tau_{ch} = \frac{1}{|G-\alpha|}. \quad (6)$$

If the electron density is low and $G - \alpha < 0$, the system attains an equilibrium state with the number of photons $\bar{N}^{(s)} = Q/|G - \alpha|$ during a time period of $t \geq \tau_{ch}$. Now assume, on the contrary, that the electron density is high and the system occurs above the threshold $G > \alpha > 0$. In addition, let the electron bunch length be sufficiently large (so that $l_b\beta_z/\beta \gg L$). Under these conditions, the generator features a linear (with respect to time) growth in the number of photons produced from spontaneous noise during the time period $0 < t \ll \tau_{ch}$, whereby $\bar{N} = Qt$. For $t \geq \tau_{ch}$, radiation is mostly generated due to the aforementioned induced processes. As a result, the system passes to a regime of exponential growth in the average photon number,

$$\bar{N} = \frac{Q}{G-\alpha}\exp(G-\alpha)t, \quad (7)$$

which lasts during the time period $\tau_b > t > \tau_{ch}$, where τ_b is the electron bunch lifetime.

If a field in the resonator is not very strong, the nonlinear effects are insignificant and formula (5) is sufficient to describe operation of the generator. When the field is strong, a correct description of the electron dynamics must take into account the field corrections. This will lead to a saturation of the amplification, the mechanism of which can be related to a nonlinear shift of the electron velocity $\beta_z(\bar{N})$ toward the region where $G(\beta_z) - \alpha = 0$. Description of the generator operation with allowance of both spontaneous and nonlinear effects presents a complicated problem, the solution of which is beyond the scope of this study.

The above results can be illustrated by a numerical example. According to formula (4), the amplification coefficient is a function of both the resonator mode number and the z component of the electron velocity: $G = G(r; \beta_z)$. Let us consider the first resonator mode ($r = 1$). The results of numerical modeling show that $G(\beta_z)$ is an oscillating function of the electron velocity, with the first maximum at $\beta_z = 0.7$ (where $\beta_x = 0.6$ and the average electron beam energy is $E = 1.3$ MeV). For an electron beam current of $I = 1$ kA and a resonator length of $L = 5$ mm, the amplification coefficient at a wavelength of 1 cm is $g = c^{-1}G(1; 0.7) = 0.02$ cm^{-1}. The characteristic time of the first mode is $\tau_{ch} = 1.76$ ns. Therefore, exponential growth in the number of photons given by formula (7) is possible for electron bunches with a duration above 2 ns. In conclusion, it should also be noted that the radiation frequency ω_r can be tuned either discretely (by changing the mode number r) or continuously (by varying the resonator length L).

Acknowledgments. This study was supported by the International Scientific-Technological Center, grant no. A-87.

REFERENCES

1. V. L. Ginzburg and I. M. Frank, Zh. Éksp. Teor. Fiz. **16**, 15 (1946).
2. V. L. Ginzburg and V. N. Tsytovich, *Transition Radiation and Transition Scattering* (Nauka, Moscow, 1984; A. Hilger, Bristol, 1990).
3. V. M. Arutyunyan and S. G. Oganesyan, Zh. Éksp. Teor. Fiz. **72**, 465 (1977) [Sov. Phys. JETP **45**, 244 (1977)].
4. S. G. Oganesyan and V. A. Engibaryan, Kvantovaya Élektron. (Moscow) **7**, 2213 (1980).
5. S. G. Oganesyan, Phys. Rev. E **59**, 4573 (1999).
6. S. G. Oganesyan, Phys. Rev. E **56**, 4683 (1997).
7. Yu. A. Anan'ev, *Optical Resonators and Problem of Divergence of Laser Emission* (Nauka, Moscow, 1979).
8. D. A. G. Deacon, L. R. Elias, J. M. J. Madey, *et al.*, Phys. Rev. Lett. **38**, 892 (1977).
9. V. B. Berestetskii, E. M. Lifshitz, and L. P. Pitaevskii, *Relativistic Quantum Theory* (Nauka, Moscow, 1968; Pergamon, Oxford, 1971), Part 1.

Translated by P. Pozdeev

Technical Physics Letters, Vol. 29, No. 1, 2003, pp. 51–53. Translated from Pis'ma v Zhurnal Tekhnicheskoĭ Fiziki, Vol. 29, No. 2, 2003, pp. 23–29.
Original Russian Text Copyright © 2003 by Rokakh, Stetsyura, Zhukov, Serdobintsev.

Peculiarities in the Ion Etching of Heterophase Semiconductors under Illumination with White Light

A. G. Rokakh, S. V. Stetsyura, A. G. Zhukov, and A. A. Serdobintsev

Saratov State University, Saratov, Russia

e-mail: semiconductor@sgu.ssu.runnet.ru

Received July 4, 2002

Abstract—The distribution of impurities in photoconducting heterophase CdS–PbS films was studied by secondary-ion mass spectrometry. It was established that illumination with white light influences the yield of cadmium and lead ions: the former yield decreases and the latter increases. The higher yield of lead ions is related to the fact that lead is predominantly contained in narrow-bandgap parts of the photoconductor, which act as a sink for nonequilibrium electrons and holes. *© 2003 MAIK "Nauka/Interperiodica".*

Previously [1, 2], we established that the use of substances characterized by a limited mutual solubility provides for a significant increase in the stability of wide-bandgap photoresistors with respect to degradation. Owing to the limited mutual solubility of CdS and PbS [3], a heterophase material (referred to below as CdS–PbS) can be obtained under certain conditions [4], which represents a wide-bandgap matrix (a solid solution of PbS in CdS) with narrow-bandgap low-ohmic inclusions (a solid solution of CdS in PbS). The content of Pb in the wide-bandgap matrix does not exceed 2% [5]. The carrier generation process takes place predominantly in the matrix, while recombination is determined to a considerable extent by the narrow-bandgap inclusions. This is confirmed by data on the IR luminescence [6].

Since the stability of this heterophase material with respect to degradation is related to the presence of narrow-bandgap inclusions, it was of interest to study the distribution of lead over the film thickness. The problem was solved by the method of secondary-ion mass spectrometry (SIMS). The results of our SIMS measurements revealed the influence of illumination on the yield of secondary ions. To our knowledge, this effect was never reported in the literature.

The purpose of this work was to study the distribution of lead and cadmium in CdS–PbS films and the effect of illumination on the rate of ion etching of this heterophase semiconductor.

The experiments were performed in a setup based on an MI-1305 mass spectrometer (Russia). A beam of positively charged oxygen ions with an energy of 5–10 keV was incident on a sample at an angle of 60° to the sample surface normal. Using a focusing system, it was possible to obtain an ion beam with a diameter of about 1 mm. The primary ion beam current was within 10–15 μA, which makes the substrate heating insignificant. The secondary ion current was amplified by an electron multiplier (VEU-1a) and by an electrometric amplifier (U5-11), after which the amplified signal was recorded. The mass spectra were measured in a range from 1 to 240 amu. Simultaneously, the amplified signals were processed by an analog-to-digital converter (L-1450) and stored in a computer file for subsequent processing. The current strength at the secondary electron multiplier output is proportional to the content of a given element in the sample studied.

In the initial stage of investigation, we modified the experimental setup so as to implement the procedure of etching high-ohmic samples with neutral atoms in order to minimize the target surface charging known to influence the results of SIMS measurements [7]. Another measure taken in order to eliminate this influence was the use of a grounded tantalum diaphragm in contact with the sample surface. In addition, the magnetic field strength of the ion detector was periodically adjusted so as to fit to the maximum signal intensity for each element measured.

We obtained the mass spectra of various elements, the most interesting of which refer to Cd and Pb (Fig. 1). In calculating the percentage content of these metals, we also took into account the peaks corresponding to cadmium and lead oxides. Figure 2 shows the variation of the peak intensities in the mass spectra with the time of sample etching, from which it is possible to judge the distribution of elements across the film thickness. Note that a high yield of elements in the initial stage of etching is related to defectness of the surface and the presence of oxides characterized by a higher etching rate. With an allowance for this circumstance, the relative percentage content of Cd and Pb in the sample was estimated as 87.27 and 12.73% in the upper layers of the film, which changed to 94.33 and 5.67% (reflecting a higher cadmium content) in the near-substrate layers (for a 1 : 9 weight ratio of CdS to PbS in

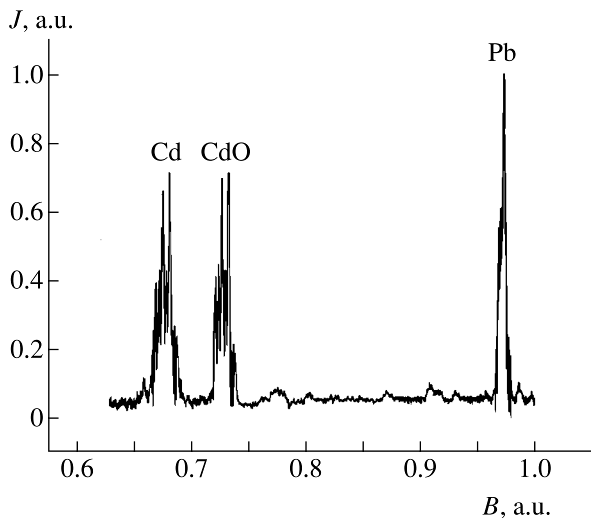

Fig. 1. A fragment of the secondary-ion mass spectrum of a CdS–PbS film sample.

the initial component mixture used for the sample synthesis).

The depth profiles of Cd and Pb measured in the dark (Fig. 2) showed that, after etching off the defective and oxidized surface layer, the samples contain no regions with pronounced gradients of concentration of these elements. During short-time (15–30 s) exposure of the sample to white light, we observed a sharp decrease in the yield of Cd ions (Fig. 3a). Immediately after switching off the illumination, the signal intensity was restored on the initial level. A relative change in the signal intensity during each exposure amounted on the average to 30%. In the Pb profile (Fig. 3b), a relative change in the signal intensity amounted on the average to 10% and, in contrast to Cd, the Pb ion yield increased (rather than decreased) under illumination. Since the content of Pb in the wide-bandgap matrix is negligibly small, this result indicates that the sputtering yield increases (as compared to the dark level) in the region of narrow-bandgap inclusions.

According to published data, suppression of the yield of positively charged ions from a semiconductor is usually related to a decrease in the electron work function of the sample surface. This phenomenon is described by the empirical formula [8]

$$\frac{Y^+}{Y_0^+} = \exp\left(\frac{\Delta A}{\varepsilon_p}\right), \quad (1)$$

where Y_0^+ and Y^+ are the yields of positively charged ions in the dark and under illumination, respectively; ΔA is a change in the electron work function; and ε_p = 0.1 eV is the characteristic parameter of the system (depending on the ion energy and emission angle).

Since the duration of measurements with the light switched on did not exceed one second, we may suggest that processes responsible for the observed phenomenon in the semiconductor are of electronic, rather than ionic, nature. Therefore, by analyzing changes in the ion yield during a short-time illumination, we may ignore the long-term processes, for example, related to

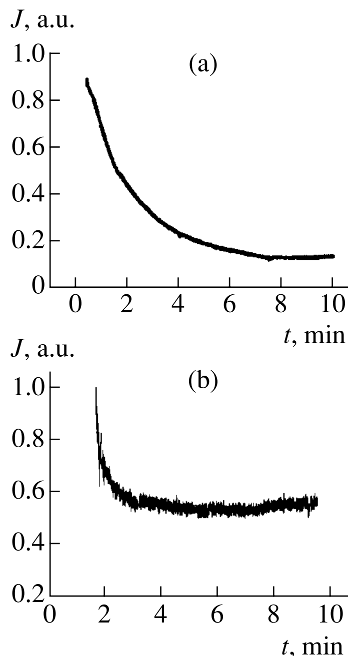

Fig. 2. Time variation of the yield of secondary ions of (a) lead and (b) cadmium from a CdS–PbS sample etched in the dark.

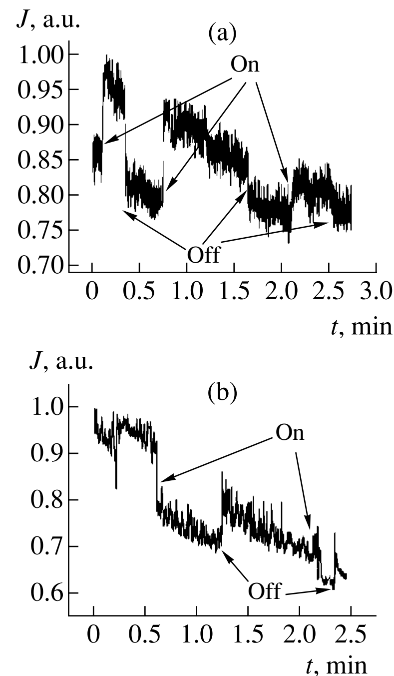

Fig. 3. Time variation of the secondary ion yield from a CdS–PbS sample etched in the dark with short-time exposures to white light: (a) lead ions; (b) cadmium ions.

the adsorption of oxygen from the primary ion beam. Then, a change in the electron work function determining the secondary yield upon illumination is caused by an increase in the density of free electrons and, hence, by the corresponding change in the Fermi quasilevel $\Delta E_{\rm Fn}$ [9].

Estimates obtained using formula (1) showed that the experimentally observed decrease in the yield of Cd ions corresponds to a change in the Fermi quasilevel approximately by 0.05 eV. The same variation of the Fermi quasilevel follows from the experimentally observed change in the photoconductivity by six orders of magnitude. This estimate is obtained by substituting the parameters typical of CdS–PbS into the formula

$$\Delta\sigma = N_c q\mu\left(\exp\left(\frac{\Delta E_{\rm Fn}}{kT}\right) - 1\right), \quad (2)$$

where $N_c = 10^{18}$ cm^{-3} is the density of states in the conduction band, q is the electron charge, $\mu = 50$ cm^2/(V s) is the mobility of electrons, k is the Boltzmann constant, and $T = 300$ K is the temperature.

At the same time, the increase in the charge carrier density Δn corresponding to this change in position of the Fermi quasilevel is

$$\Delta n = n_0\left(\exp\left(\frac{\Delta E_{\rm Fn}}{kT}\right) - 1\right), \quad (3)$$

which agrees well with the value calculated as

$$\Delta n = \alpha\beta\Delta\Phi\tau, \quad (4)$$

where $n_0 = 10^{12}$ cm^{-3} is the equilibrium electron density, $\alpha = 10^4$ cm^{-1} is the optical absorption coefficient, $\beta = 1$ is the quantum yield, $\Delta\Phi = 10^5$ cm^{-2} s^{-1} is the illumination jump, and $\tau = 10^{-4}$ s is the carrier lifetime.

The above considerations explain the decrease in the yield of Cd ions during illumination. As for Pb, which is characterized by a virtually constant position of the Fermi quasilevel in the narrow-bandgap inclusions (related to high values of the initial electron density and the rate of recombination of the nonequilibrium charge carriers), the aforementioned effect is very weak. Moreover, this effect cannot principally explain the increase in the Pb ion yield.

We suggest the following explanation based on the model of a heterophase semiconductor stable with respect to degradation [10]. The nonequilibrium charge carriers generated by illumination are concentrated in the potential wells (the sites of localization of the narrow-bandgap inclusions) and exhibit recombination at these sites. The liberated energy is transferred to atoms in the crystal lattice, whereby atoms in the narrow-bandgap inclusions are excited. This leads to an increase in the ion etching rate, in agreement with the growth in the Pb ion yield observed upon illumination.

Thus, the mass-spectrometric investigation of polycrystalline CdS–PbS films revealed an unusual response of the secondary ion yield to light-induced excitation of the electron subsystem of the semiconductor. In our opinion, this effect is explained by the fact that the narrow-bandgap phase (in which lead atoms are predominantly concentrated) acts as a sink for nonequilibrium charge carriers and, hence, for the light-induced excitations in the photoconducting heterophase semiconductor studied.

REFERENCES

1. V. E. Bukharov, A. G. Rokakh, and S. V. Stetsyura, Pis'ma Zh. Tekh. Fiz. **25** (3), 66 (1999) [Tech. Phys. Lett. **25**, 111 (1999)].
2. V. E. Bukharov and A. G. Rokakh, Pis'ma Zh. Tekh. Fiz. **25** (24), 55 (1999) [Tech. Phys. Lett. **25**, 994 (1999)].
3. G. S. Oleinik, P. A. Mizetskiĭ, A. I. Nizkova, *et al.*, Izv. Akad. Nauk SSSR, Neorg. Mater. **19**, 1799 (1983).
4. RF Patent No. 845685, MKI H 01 L 21/30/; A. G. Rokakh, A. V. Kumakov, and N. V. Elagina, RF Patent No. 2880165/18-25; Byull. Izobret., No. 25 (1993).
5. A. G. Rokakh, S. V. Stetsyura, N. B. Trofimova, and N. V. Elagina, Izv. Ross. Akad. Nauk, Neorg. Mater. **35**, 552 (1999).
6. A. G. Rokakh and N. B. Trofimova, Zh. Tekh. Fiz. **71** (7), 122 (2001) [Tech. Phys. **46**, 926 (2001)].
7. S. N. Belyaev, A. G. Zhukov, and A. A. Serdobintsev, *Abstracts of Papers. The VIIIth Int. Workshop: Beam Dynamics and Optimization* (Saratov, 2001), p. 17.
8. *Sputtering by Particle Bombardment*, Ed. by R. Behrisch (Springer-Verlag, New York, 1981, 1983; Mir, Moscow, 1984, 1986), Vols. I and II.
9. A. Rose, *Concepts in Photoconductivity and Allied Problems* (Interscience, New York, 1963; Mir, Moscow, 1966).
10. A. G. Rokakh, Pis'ma Zh. Tekh. Fiz. **10**, 820 (1984) [Sov. Tech. Phys. Lett. **10**, 344 (1984)].

Translated by P. Pozdeev

Technical Physics Letters, Vol. 29, No. 1, 2003, pp. 54–56. Translated from Pis'ma v Zhurnal Tekhnicheskoĭ Fiziki, Vol. 29, No. 2, 2003, pp. 30–34.
Original Russian Text Copyright © 2003 by Obolensky, Skupov.

Peculiarities of the Long-Range Effects in GaAs-Based Transistor Structures upon Combined Irradiation with Ions of Various Masses

S. V. Obolensky and V. D. Skupov
Nizhni Novgorod State University, Nizhni Novgorod, Russia
e-mail: obolensk@rf.unn.runnet.ru
Received July 15, 2002

Abstract—Anomalous distinctions in the depth profiles of charge carrier density in the active regions of GaAs-based structures were observed for samples irradiated from the rear side (through substrate) with molecular hydrogen and argon ions either separately or in a certain combined sequence. The maximum effect of ion irradiation was observed in the structures characterized by increased density of defects in the buffer layer. The experimental results are explained by reconstruction of the impurity–defect complexes at the layer interfaces under the action of elastic waves arising both as a result of relaxation of the atomic displacement peaks in the ion stopping zone and due to the reverse piezoelectric effect. © *2003 MAIK "Nauka/Interperiodica".*

Previously [1, 2], we demonstrated that irradiation of epitaxial GaAs structures with medium-energy ions through substrate (i.e., under conditions where a long-range effect is manifested) improves the parameters of Schottky barrier field effect transistors (SBFETs). However, it remained unclear how the results of irradiation depend on the degree of defectness of the initial GaAs structure and on the type of bombarding ions. Moreover, in the context of results reported by Demidov *et al.* [3], it was also of interest to study the effect of combined irradiation with ions of different masses that might enhance the gettering capacity of the implanted material. Our study aimed at elucidating these aspects of the long-range effects of ion irradiation.

The experiments were performed with n^+nn^--GaAs structures of three types: a high-quality structure after a short storage (structure 1), a high-quality structure stored for 10 years under normal conditions (structure 2), and a structure containing defects at the epilayer–substrate interface (structure 3). The structures of each type were used to fabricate SBFETs with a gate thickness of 0.5 μm. The transistor design and preparation technology are described elsewhere [1]. The total thickness of the sample structures was about 200 μm.

The wafers with transistor structures were irradiated from the rear side (through substrate) with 90-keV H_2^+ and Ar^+ ions to a total dose of 10^{14} cm^{-2}. The irradiation was performed either by ions of one type or by sequential exposures in a combination of $H_2^+ + Ar^+$ or $Ar^+ + H_2^+$. Each treatment was effected within a certain region of the wafer, so that five samples (including an unirradiated control) were prepared from each wafer. Before and after irradiation, the structures were characterized by standard current–voltage, capacitance–voltage, and high-frequency characteristics of the transistors. In addition, the parameters of technological defects in the epitaxial layers were determined using the total current spectroscopy.

Experimental depth profiles of the relative carrier density $\delta n = (n - n_0)/n_0$ (where n_0 and n are the electron densities before and after ion irradiation, respectively) are presented in the figure. As can be seen, the most pronounced irradiation-induced changes in the carrier density profiles in the active region took place in structure 3, while a minimum effect was found in structure 1. The extrema observed in the curves are explained by the influence of the interphase boundaries between active (n-GaAs) and buffer (n^--GaAs) layers (situated at a depth of 0.1–0.2 μm) and between the epitaxial layer and the substrate (at a depth of 0.6 μm).

Irradiation with hydrogen ions leads to a local increase in the charge carrier density at the active layer–buffer interface. In contrast, irradiation with argon ions or with both ions in the $Ar^+ + H_2^+$ sequence decreases the carrier density in this region. It is interesting to note that the profiles obtained after Ar^+ and $H_2^+ + Ar^+$ treatments in all cases show an increase in the electron density with depth.

Effects of the ion irradiation in various regimes on the concentration of defects in the epilayer were also different. The relative concentrations of defects corresponding to levels with an energy of ~0.4 eV (presumably, E3 type traps) and ~0.8 eV (presumably, EL2 type centers) determined by deep-level transient spectroscopy (I-DLTS technique) in the samples of structure 3

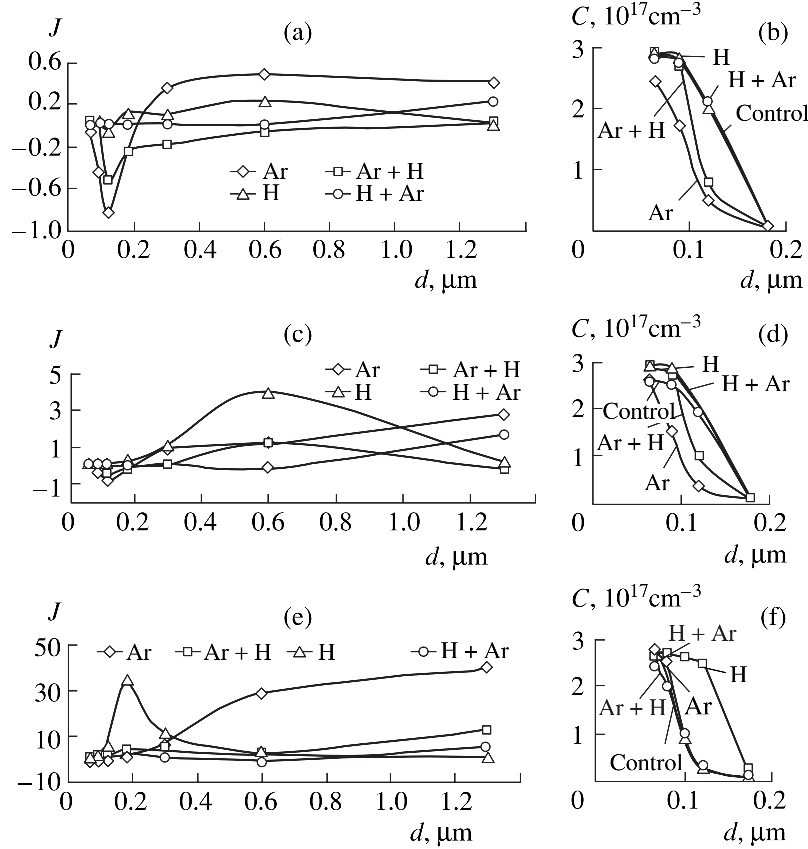

The profiles of the relative (a, c, e) and absolute (b, d, f) electron density variation in depth of GaAs structures of various types after gettering induced by irradiation with ions possessing different masses: (a, b) structure 1; (c, d) structure 2; (e, f) structure 3.

are given in the table. As can be seen from these data, irradiation with argon and hydrogen ions produces opposite effects on the concentration of defects corresponding to shallow traps of the E3 type. This result, together with data on the carrier density profiles, is indicative of a different nature of the long-range effects induced by these ions in epitaxial GaAs structures.

According to the existing notions, the long-range effects are explained by modification of the impurity–defect subsystem of an ion-irradiated material under the action of nonequilibrium point defects and elastic waves arising within the ion stopping range. Estimates (based on the results reported in [4]) of the pressure amplitudes in the elastic waves reaching the active regions of the epitaxial structures studied gave 2×10^3 and 1×10^5 Pa for irradiation with hydrogen and argon ions, respectively. Therefore, only the bulk elastic waves generated in the displacement peaks induced by the argon ion bombardment can be effective.

In our opinion, hydrogen ions can excite elastic waves at the heterostructure surface due to the reverse piezoelectric effect related to the formation of ionization peaks along the stopping tracks of hydrogen ions. To a first approximation, the amplitude of these waves can be estimated from the relation

$$P = \frac{EQ}{fRh},$$

where E is the elastic modulus of the target material,

Variation of the defects density in structure 3 after ion-induced gettering (I-DLTS data)

Energy of levels, eV	Relative density of defects				
	before gettering	after Ar^+ treatment	after H_2^+ treatment	$H_2^+ + Ar^+$ treatment	$Ar^+ + H_2^+$ treatment
≈0.4	1	0.7 ± 0.25	1.86 ± 0.5	0.3 ± 0.12	0.95 ± 0.3
≈0.8	1	Unchanged to within experimental error			

Q is the charge arising at the particle stopping track, f is the piezoelectric constant (we assume that f_{GaAs} = 0.154 C/m^2), h is the epitaxial structure thickness or the Debye length (minimum of the two vales), and R is the ion range in the target material.

According to published data, the carrier density in GaAs (AGChP-10 grade) does not exceed 10^{13}–10^{14} cm^{-3}. Substituting numerical values into the above formula, we obtain $P \sim 10^7$ Pa for $h = 200$ μm and $P \sim 10^8$ Pa for $h = 20$ μm. The former case corresponds to excitation of a surface elastic wave (on the transistor side of the structure), while the latter case corresponds to a bulk wave (which also reaches the surface of the device structure). Pressure waves of such amplitudes are capable of stimulating reconstruction of the impurity–defect complexes, especially at the surface representing an effective source and sink of point defects [4]. As was noted previously [5, 6], elastic waves can be amplified on their passage through a crystal containing technological or other defects. This can account for an additional enhancement of the long-range effects in GaAs, which is characterized by a much higher density of defects as compared to silicon. We are planning subsequent experiments so as to elucidate the processes responsible for the differences observed in the GaAs response to irradiation with ions possessing different masses.

Acknowledgments. The authors are grateful to A.G. Fefelov for his help in conducting experiments.

This study was partly supported by the NATO Science for Peace Program (grant no. SFP-973797).

REFERENCES

1. S. V. Obolenskiĭ, V. D. Skupov, and A. G. Fefelov, Pis'ma Zh. Tekh. Fiz. **25** (16), 50 (1999) [Tech. Phys. Lett. **25**, 655 (1999)].
2. S. V. Obolenskiĭ and V. D. Skupov, Pis'ma Zh. Tekh. Fiz. **26** (15), 1 (2000) [Tech. Phys. Lett. **26**, 645 (2000)].
3. E. S. Demidov, V. V. Karzanov, K. A. Markov, *et al.*, Zh. Éksp. Teor. Fiz. **120** (3), 637 (2001) [JETP **93**, 558 (2001)].
4. P. V. Pavlov, Yu. A. Semin, V. D. Skupov, *et al.*, Fiz. Tekh. Poluprovodn. (Leningrad) **20**, 503 (1986) [Sov. Phys. Semicond. **20**, 315 (1986)].
5. Yu. A. Semin, V. D. Skupov, and D. I. Tetelbaum, Pis'ma Zh. Tekh. Fiz. **14**, 273 (1988) [Sov. Tech. Phys. Lett. **14**, 121 (1988)].
6. V. D. Skupov, D. I. Tetelbaum, and G. V. Shengurov, Pis'ma Zh. Tekh. Fiz. **15** (22), 44 (1989) [Sov. Tech. Phys. Lett. **15**, 890 (1989)].

Translated by P. Pozdeev

Technical Physics Letters, Vol. 29, No. 1, 2003, pp. 57–59. Translated from Pis'ma v Zhurnal Tekhnicheskoĭ Fiziki, Vol. 29, No. 2, 2003, pp. 35–41.
Original Russian Text Copyright © 2003 by Tetelbaum, Azov, Golyakov.

The Effect of Irradiation on the Mechanical Properties of Metals

D. I. Tetelbaum, A. Yu. Azov, and P. I. Golyakov
Physicotechnical Research Institute, Nizhni Novgorod State University, Nizhni Novgorod, Russia
e-mail: Tetelbaum@phys.unn.runnet.ru
Received August 7, 2002

Abstract—The results of experiments with irradiated permalloy-79 foils show that a necessary condition for a change in the alloy microhardness to take place on the rear (unirradiated) side of the foil is the presence of a natural oxide film on the exposed side of the sample. It is established that the observed phenomenon is not related to heating of the samples and the magnitude of the effect depends in a nonmonotonic manner on the irradiation dose. A possible mechanism of this phenomenon is discussed. © *2003 MAIK "Nauka/Interperiodica".*

Previously [1], we reported on a new effect whereby irradiation of a permalloy-79 foil resulted in a change in the alloy microhardness both on the exposed and on the opposite (unirradiated) side of the sample. Later [2, 3], it was established that this phenomenon is observed not only in permalloy, but in other metals as well. Recently [4], an analogous effect was also observed in silicon.

Below we present experimental data unambiguously evidencing that (i) the observed phenomenon is not related to heating of a sample, (ii) the effect is observed only in a limited energy (irradiation dose) interval, and (iii) a necessary condition for this effect is the presence of an oxide layer (at least a natural oxide film) on the irradiated sample surface.

The experiments were performed with samples made of a 20-μm-thick foil of permalloy-79. The radiation source was a 300-W halogen lamp. The microhardness (H) was measured using a PMT-3 instrument. Upon a thorough analysis of the statistical and systematic errors, we have established that the average variations in H exceeding 3–4% can be reliably determined with a confidence probability better than 0.9. Selection of the load at 20 g, on the one hand, ensured acceptable accuracy of the microhardness measurements and, on the other hand, met the requirement of a sufficiently small ratio of indentation depth to sample thickness.

Upon irradiation of a sample, comparable changes in the H value are observed on both sides of the foil. Since the long-range character is the most interesting feature of the observed phenomenon, the data presented below refer only to the rear side of the samples.

In order to reliably establish that the changes in microhardness H as a result of irradiation are not caused by trivial heating, the direct temperature measurements using a thermocouple were supplemented by irradiation under the following conditions.

(1) The samples during exposure were mounted on a massive metal block, with a reliable thermal contact provided by using an indium-gallium paste. This was the base measurement regime.

(2) In order to provide for a still more effective heat removal, we performed a special series of experiments in which the samples were placed into a cell with deionized water. This medium both screened the sample from thermal (IR) radiation and ensured better heat removal.

(3) The samples were irradiated at various temperatures in the range from 0 to 150°C.

In all these cases, provided the same irradiation power and duration, the observed changes in microhardness H were the same. Even more convicting results were obtained in the experiment with the foil surface covered with a thin layer of black dye. The dye film completely absorbed the light, while virtually not increasing the total heat capacity of the sample. In this test, the radiation-induced heating can differ from that in the base experiment only toward increase. However, it was found that the H value did not change (to within the usual experimental accuracy). Thus, we may conclude that the increase in H upon irradiation is caused by a factor of more fundamental nature rather than by trivial heating.

In the next stage of the investigation, we have established the energy conditions necessary for the observation of changes in H. As was already pointed out in [1], the relative change in microhardness ($\Delta H/H$) depends in a nonmonotonic manner on the duration of exposure. In this study, we conducted a series of systematic experiments to determine the dependence of $\Delta H/H$ (i) on the irradiation time at a fixed distance (R) from a sample to the light source and (ii) on the distance R at a fixed irradiation time. It was found that the $\Delta H/H$ versus D plots (D is the radiant energy per unit area, called the radiant exposure or dose) represent rather closely spaced curves possessing a dome shape with a maximum at an almost constant position on the abscissa axis (Fig. 1). It is a remarkable fact that, as the D value exceeds a cer-

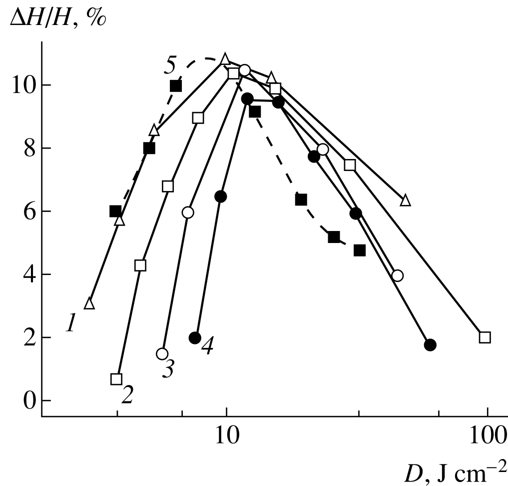

Fig. 1. Plots of the relative change in microhardness versus energy density (dose) for a permalloy-79 foil (rear side) irradiated with the light of a halogen lamp for 2, 4, 6, and 8 s (solid curves *1–4*, respectively) and with 40-keV Ar^+ ions (dashed curve *5*, $\Delta H/H$ values reduced by a factor of 2.5).

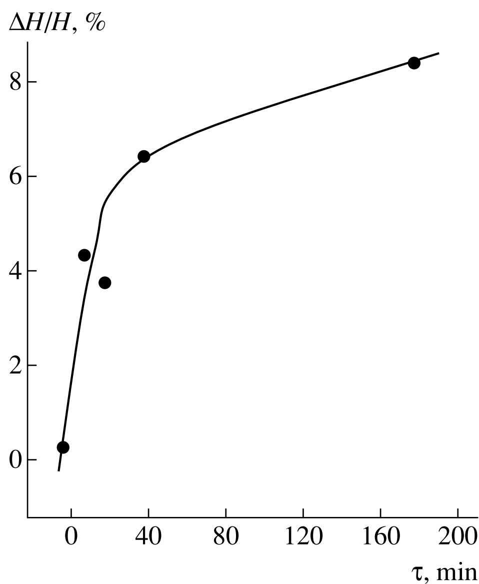

Fig. 2. Effect of oxide removal, followed by exposure in air for time period τ, on the relative change in microhardness of a permalloy-79 foil (rear side) irradiated with the light of a halogen lamp for 4 s at a distance of 2.5 cm.

tain threshold, the $\Delta H/H$ value tends to zero. This fact partly explains why this phenomenon was not discovered previously: to observe the effect, it is necessary to fall within a certain dose interval (another reason is the presence of relaxation: upon switching off the light, the irradiation-induced change in H in most cases decays to zero during a time period on the order of one day).

It was interesting to compare the dependences of $\Delta H/H$ on D to the nonmonotonic dependence of $\Delta H/H$ on the dose observed for the ion-irradiated metal foils (low-dose long-range effect, LDLRE) [5]. The latter dependence, recalculated to the same energy units as above, is also plotted in Fig. 1. As can be seen, both the shape of this curve and the position of the maximum on the D scale for the two kinds of radiation are close.

We believe that the analogy between the cases of ion and optical radiation is by no means accidental, suggesting the need in searching for deep common reasons accounting for a change in the properties of materials observed far from the zone of energy deposition. The LDLRE mechanisms have been repeatedly discussed (see, e.g., [5] and references therein). It was demonstrated that the most probable mechanism of this effect is related to the ion-excited elastic (or, more precisely, deformation) waves and their interaction with the initial structural imperfections. The latter factor plays a key role not only in LDLRE [5], but also in the long-range effect observed in ion-irradiated semiconductors [6]. Pavlov *et al.* [6] gave theoretical estimates for the deformation wave model in materials with extended defects. These estimates are also applicable (with certain corrections) to metals. However, the initial premise concerning the possibility of deformation wave generation under the action of "soft" radiation such as light is the most difficult point of this model. The absence of any significant thermal action excludes the possibility of explanations involving temperature gradients. Nor can we adopt the possibility of processes related to electron subsystem excitation localized inside a metal (possible in the case of high-power laser irradiation).

Previously [2, 3], we put forward a hypothesis that a deformation wave can arise as a result of trapping of photoelectrons in a natural oxide film. We have undertaken experimental verification of this hypothesis concerning the role of a natural oxide. For this purpose, a series of experiments were performed under the conditions when irradiation takes place in the absence of the natural oxide. The foil was irradiated when immersed in a hydrochloric acid solution, which dissolves the oxide but not the metal. In complete agreement with the above hypothesis, it was found that the irradiation under these conditions does not lead to a change in the microhardness. In another series of experiments, the samples were irradiated in air, with various time intervals (τ) between the oxide removal and the exposure. As can be seen from the data in Fig. 2, the value of $\Delta H/H$ increase with τ (i.e., with the growing oxide thickness) and eventually exhibits saturation. This result shows that the presence of a natural oxide layer during irradiation is a necessary condition for the effect to be observed. It should be emphasized that the oxide has to be present on the exposed side: removal of the oxide from the rear (unirradiated) side did not change the results of experiments. Note that the oxide only acts as a mediator, since the change in mechanical properties is observed in the metal proper. Removal of the natural oxide after irradiation of the sample does not change the H value as compared to that for the sample with oxide.

How can the natural oxide mediate in the observed phenomenon? We propose the following model. Irradiation of a sample leads to the emission of photoelectrons from the metal, followed by trapping of these electrons on traps in the oxide. In permalloy, where the main alloy component is nickel, the base oxide component is nickel oxide—a dielectric with a large degree of ion bonding [7]. The trapping of electrons in the oxide gives rise to Coulomb forces and breaks the local atomic equilibrium, while the resulting atomic displacements give rise to deformation waves.

We have simulated this process by methods of molecular dynamics (as briefly mentioned in [3]). A cubic block composed of Ni and O ions modeled a region of the natural oxide on permalloy. At the initial time instant, ions were at rest, but then the charge of one ion was changed by unity in a jumplike manner to model the electron trapping. Because of the charge-induced disbalance of the interatomic forces, atoms (ions) in the block began to move. The program traced the velocities and momenta of all atoms in the sample. The pressure that developed in the system was determined with preset steps in time and space as the resulting force (per unit area) with which all moving atoms acted upon a selected atom occurring at a certain distance from the perturbation focus. The dependence on this distance was extrapolated outside the model block. It was found that pressures arising in this system are comparable with those developed in thermal spikes during ion irradiation [6]. When the deformation wave enters the metal, the process can develop according to the same scenario as in the case of the long-range effect in ion-irradiated semiconductors [5, 6]. Eventually, a change in the microhardness is caused by the deformation wave action upon the defect subsystem of the metal, resulting in a transformation of this subsystem. The difference from the case of semiconductors [6], featuring the quasi-spherical defect clusters, consists in that the major role in metals is played by the defect–impurity pileups localized at the extended defects of the dislocation type (Cottrell atmosphere). Evidence for the participation of deformation waves is that the microhardness H changes not only in the irradiated foil, but also in the foil put under the exposed sample (as in the LDLRE case [5]).

Of course, the above model does not explain all peculiarities of the complicated and rather unusual phenomenon observed and can be considered only as a "seed" for the subsequent theoretical and experimental investigations. The problem of a nonmonotonic dose dependence of $\Delta H/H$ will be considered separately, within the framework of an analysis of the result of our recent detailed investigations and the data on the post-irradiation relaxation. In the following, it is necessary to study in more detail the role of the surface films and the radiation spectrum, to employ different methods, and to the study the effect in other metals.

Acknowledgments. This study was supported by the Ministry of Education of the Russian Federation ("Basic Investigations of High School into Priority Directions in Science and Technology" Program, Subprogram 205).

REFERENCES

1. D. I. Tetelbaum, A. A. Trofimov, A. Yu. Azov, *et al.,* Pis'ma Zh. Tekh. Fiz. **24** (23), 9 (1998) [Tech. Phys. Lett. **24**, 910 (1998)].
2. D. I. Tetelbaum, A. A. Trofimov, E. V. Kuril'chik, *et al.,* Vestnik Nizhn. Novg. Gos. Univ. im. N.I. Lobachevskogo, Ser. Fiz. Tverd. Tela **2**, 157 (1998).
3. D. I. Tetelbaum, Yu. A. Semin, V. V. Khabibulov, *et al.,* Proc. SPIE **368**, 264 (1999).
4. D. I. Tetelbaum, V. A. Panteleev, A. Yu. Azov, and M. V. Gutkin, Poverkhnost, No. 5, 87 (2000).
5. D. I. Tetelbaum, E. V. Kurilchic, and N. D. Latisheva, Nucl. Instrum. Methods Phys. Res. B **127**/**128**, 153 (1997).
6. P. V. Pavlov, Yu. A. Semin, V. D. Skupov, *et al.*, Fiz. Tekh. Poluprovodn. (Leningrad) **20**, 503 (1986) [Sov. Phys. Semicond. **20**, 315 (1986)].
7. V. B. Lazarev, V. V. Sobolev, and I. S. Shaplygin, *Chemical and Physical Properties of Simple Oxides* (Nauka, Moscow, 1983).

Translated by P. Pozdeev

Technical Physics Letters, Vol. 29, No. 1, 2003, pp. 60–61. Translated from Pis'ma v Zhurnal Tekhnicheskoĭ Fiziki, Vol. 29, No. 2, 2003, pp. 42–44.
Original Russian Text Copyright © 2003 by Vasil'ev.

Low-Temperature Diffusion in Polycrystalline Pd–Ag Thin Film System

A. D. Vasil'ev

Samara State Technical University, Samara, Russia

e-mail: physics@sstu.edu.ru

Received May 13, 2002; in final form, September 5, 2002

Abstract—Mutual diffusion in a polycrystalline Pd–Ag thin film system with an average grain size of 0.1 μm was studied in the temperature interval from 373 to 523 K. The effective diffusion coefficient D was determined by the X-ray diffraction technique in a region with a palladium content of 90–95%. The experimental D values are one to two orders of magnitude greater than the average coefficients of diffusion by grain boundaries in the same temperature interval. © *2003 MAIK "Nauka/Interperiodica".*

It is commonly accepted that diffusion in thin polycrystalline films with a grain size on the order of 0.1 μm proceeds predominantly by the grain boundaries [1], so that the effective diffusion coefficient cannot exceed an average value for the grain boundary diffusion. However, dominating grain boundaries in polycrystalline materials frequently represent the boundaries of minimum energy [2]. The coefficient of diffusion by these grain boundaries is smaller than that of diffusion via perfect (undissociated) edge dislocations [3]. Therefore, should the diffusion via edge dislocations predominate, the effective diffusion coefficient will exceed an average value for the grain boundary diffusion. This paper considers such a situation.

The experiments were performed with silver and palladium films deposited by evaporation from a tungsten boat onto a glass substrate in vacuum on the order of 10^{-3} Pa. The silver film was deposited first and then covered with a palladium film, both layers being approximately the same thickness of 0.1 μm (X-ray diffraction data).

The thin film system was subjected to vacuum annealing at various temperatures in the interval from 373 to 523 K. The duration of annealing was selected so as to provide that silver would diffuse into tungsten film to about one-third of the film thickness. This time depended on the temperature of annealing: as the temperature decreased from 523 to 373 K, the necessary diffusion annealing time increased from 0.3 to 10 h, respectively.

The effective diffusion coefficient was determined based on analysis of the profile of the (111) X-ray diffraction peak of a solid solution formed in the diffusion zone [4]. The accuracy of this method of determining the effective diffusion coefficient was maximum in the regions of maximum diffusion coefficient. In the samples studied, these were the regions with a palladium content of 80–95%. Here, the uncertainty of determining the effective diffusion coefficient, related to nonsystematic diffractometer errors, does not exceed 10% [5]. Under the action of various factors (stress, nonequilibrium distribution of misfit dislocations in the diffusion done, etc.), this uncertainty can increase up to 50%. The X-ray diffraction measurements were performed on a DRON-3 diffractometer using FeK_α radiation.

As can be seen from the data presented in the figure, the effective diffusion coefficients D experimentally determined in the temperature interval from 373 to 523 K in the region with a palladium content of 90–95% are one to two orders of magnitude greater than the average coefficients of diffusion by grain boundaries known for the same homologous temperatures T/T_1 (T_1 is the melting temperature of palladium) [6–8].

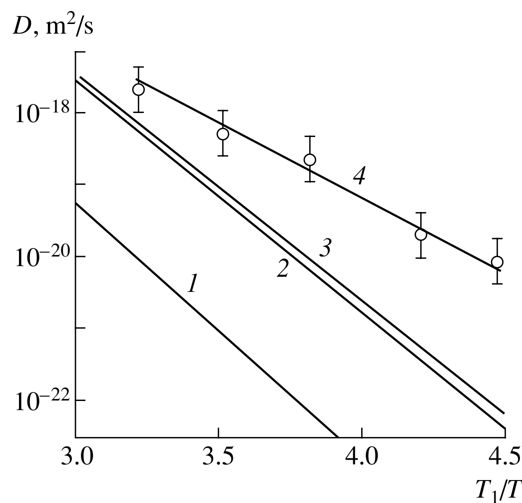

Temperature dependence of the diffusion coefficient D: (*1–3*) average grain-boundary diffusion coefficients in fcc metals [6–8]; (*4*) data for the Pd–Ag system reported in this paper.

I believe that this result is related to the fact that diffusion in the thin film system studied proceeds predominantly via perfect edge dislocations [9]. It should be noted, however, that the average grain-boundary diffusion coefficients reported in [6–8] refer to different fcc metals rather than to palladium (for which no such experimental data are available). Should analogous values in palladium be two orders of magnitude greater than those in other fcc metals, the effective diffusion coefficient in the former case would not exceed the grain-boundary diffusion coefficients. Detailed interpretation of these results requires additional investigations.

REFERENCES

1. J. Beglin and J. Poate, in *Thin Films: Interdiffusion and Reactions*, Ed. by J. M. Poate, K. N. Tu, and J. V. Mayer (Wiley, New York, 1978; Mir, Moscow, 1982).
2. O. A. Kaibyshev and R. Z. Valiev, *Grain Boundaries and the Properties of Metals* (Metallurgiya, Moscow, 1987).
3. I. Kaur and W. Gust, *Fundamentals of Grain and Interphase Boundary Diffusion* (Stuttgart, 1989; Mashinostroenie, Moscow, 1991).
4. B. Ya. Pines and E. F. Chaikovskii, Dokl. Akad. Nauk SSSR **111**, 1234 (1956).
5. A. N. Bekrenev and B. N. Fedorov, Appar. Metod. Rentgenovskogo Anal. **32**, 36 (1984).
6. A. M. Brown and M. F. Ashby, Acta Met. **28**, 1085 (1980).
7. W. Gust, S. Mayr, A. Bogel, *et al.,* J. Phys. C4 **46**, 537 (1985).
8. N. A. Gjostein, in *Diffusion* (American Society for Metals, Metals Park, Ohio, 1974), pp. 241–245.
9. A. N. Bekrenev and A. D. Vasil'ev, Metallofizika **14** (3), 91 (1992).

Translated by P. Pozdeev

Technical Physics Letters, Vol. 29, No. 1, 2003, pp. 62–63. Translated from Pis'ma v Zhurnal Tekhnicheskoĭ Fiziki, Vol. 29, No. 2, 2003, pp. 45–49.
Original Russian Text Copyright © 2003 by Flerova, Kraĭnik, Bots'va, Popov.

The Effect of Magnetic Field on Domain Electroluminescence in Barium Titanate Crystals near the Ferroelectric Phase Transition

S. A. Flerova, N. N. Kraĭnik, N. P. Bots'va, and S. A. Popov

Dnepropetrovsk National University, Dnepropetrovsk, Ukraine

Ioffe Physicotechnical Institute, Russian Academy of Sciences, St. Petersburg, 194021 Russia

Received September 9, 2002

Abstract—By measuring electroluminescence (EL) in barium titanate crystals exposed to a pulsed electric field in combination with a magnetic field, we have studied the dependence of a shift in the temperature of maximum EL on the magnetic field strength and on the mutual orientation of the electric and magnetic fields. The possible mechanisms of the observed effects are discussed. *© 2003 MAIK "Nauka/Interperiodica".*

The dynamics of domain reorientation in ferroelectrics is one of the most important basic problems in the physics of ferroelectric phenomena, the study of which has considerably contributed to the solution of many applied problems. Establishing the laws of the dynamics of domain processes in ferroelectric crystals under the combined action of electric and magnetic fields (see, e.g., [1, 2] and references therein), as well as an analysis of the mechanisms of such processes, increases our basic knowledge about the domain processes in ferroelectrics, in particular, about the role of mechanical stresses in the motion of ferroelectric domain boundaries in a magnetic field.

As is known, the domain electroluminescence (EL) in wide-bandgap ferroelectrics represents a special kind of luminescence which is extremely sensitive with respect to the domain motions of various types [2]. Below we present data on the dependence of the EL intensity in barium titanate ($BaTiO_3$) crystals exposed to a pulsed electric field in combination with a constant (or quasi-constant) magnetic field.

The experiments were performed with $BaTiO_3$ crystals of high optical quality, in the form of plates featuring a developed (001) plane, grown from a solution of components (special purity grade) in a KF melt. The measurements were conducted at various temperatures, including the region of the ferroelectric phase transition in $BaTiO_3$. The sample temperature was measured to within ± 0.025 K. The electric field E was applied in the [001] direction, while the magnetic field was applied parallel or perpendicular to the electric field. The EL was excited by bipolar rectangular pulses of the electric field with a pulse duration of 100 μs and a repetition frequency of 100 Hz.

The constant magnetic field was produced by an electric magnet of the FL-1 type with a stabilized power source, which allowed a magnetic field strength of up to 25 kOe to be obtained in a 15-mm-wide gap. Some experiments were performed in a strong pulsed magnetic field. A specially designed setup, employing discharge of a capacitor bank to a solenoid, generated a magnetic field pulse with a strength of up to 200 kOe and a duration of ~400 μs. It should be noted that the measurements in strong magnetic field are characterized by certain important distinctions from those in a constant magnetic field. In particular, it is possible to use only repolarization processes the duration of which is shorter than the time of existence of a quasilinear portion of the magnetic field pulse (restricted to 40 μs for the given setup). The $BaTiO_3$ crystals studied meet satisfy this condition.

The EL from the samples was measured using a FEU-79 photomultiplier. In order to eliminate the spurious signals induced by magnetic field in the measuring equipment and to provide for the focusing of radiation, we employed an optical fiber.

Figure 1 schematically shows the temperature dependences of the EL intensity from a $BaTiO_3$ crystal measured in the absence (curve *1*) and in the presence (curve *2*) of magnetic field. The general character of these curves is similar to that of the temperature dependence of the initial permittivity $\varepsilon(T)$. A clear difference between the temperatures of the maximum observed under various experimental conditions allowed us to measure the peak shift ΔT_m. Note that the temperature T_m at which the EL intensity maximum is observed in the absence of magnetic field (curve *1*) is stable for each particular crystal at a fixed value of the repolarizing electric field strength (~3–4 kV/cm); the T_m value is slightly (by 2–3 K for various samples) lower than the Curie temperature T_C. The maximum EL intensity in the magnetic field (curve *2*) was observed at higher temperatures.

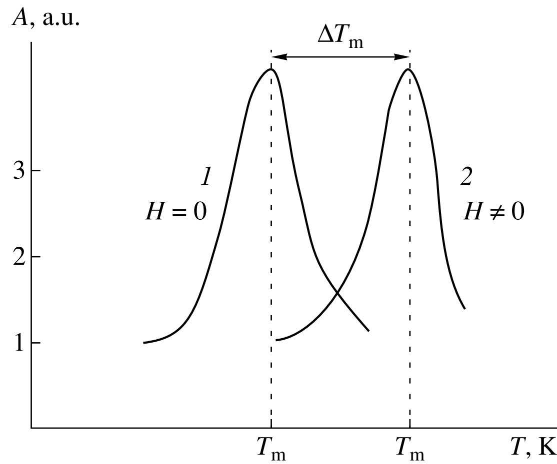

Fig. 1. Schematic temperature dependences of the EL from a $BaTiO_3$ crystal measured in the vicinity of the Curie temperature (*1*) in the absence ($H = 0$) and (*2*) in the presence ($H \neq 0$) of a magnetic field.

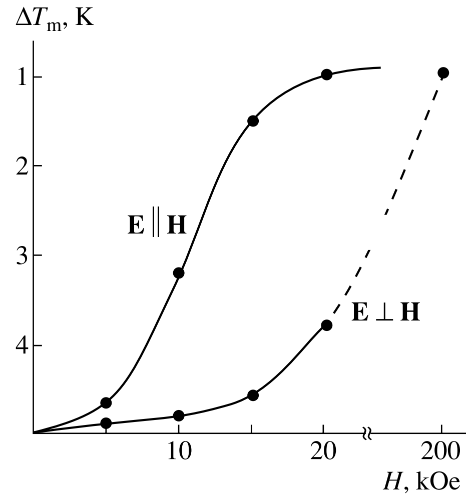

Fig. 2. Plots of the temperature shift of the EL peak versus magnetic field strength for an 0.3-mm-thick $BaTiO_3$ crystal ($E = 3.7$ kV/cm).

The results of our experiments showed that the shift ΔT_m of the EL peak depends on the magnetic field strength and the mutual orientation of the electric (**E**) and magnetic (**H**) field vectors. These results are illustrated in Fig. 2. For the parallel orientation (**E** || **H**), an increase in the field strength H led to an S-shaped growth in the peak shift ΔT_m with saturation at $H \sim 20$ kOe. For the mutually perpendicular orientation (**E** ⊥ **H**), the ΔT_m value initially varied somewhat more weakly as compared to the preceding case, but at $H \sim 200$ kOe this value also reached the level characteristic of the saturation observed for **E** || **H**.

In explaining the observed increase in the shift of T_m under the action of magnetic field, it is necessary to take into account the nature of the EL maximum and the sensitivity of this peak to the internal stresses in a ferroelectric crystal and to the character and velocity of motion of the domain boundaries. It is most probable that the observed behavior is manifestation of the effects of mechanical stresses and of the magnetic-field-induced changes in the conditions of spontaneous polarization screening and in the state of the crystal lattice defects. A certain role in the shift of the domain EL peak in the external magnetic field is played by interaction between the magnetic moments of the moving domain walls and the additional mechanical stresses developed in the vicinity of the moving domains.

The magnetic-field-induced shift of the EL maximum in a $BaTiO_3$ crystal to the temperature region of a possible heterophase structure suggests that important additional information on the dynamics of domain and interphase boundaries can be obtained from the measurements in inhomogeneous ferroelectric media characterized by smeared phase transitions. Experiments of this kind with lead magnesium niobate (a model ferroelectric relaxor) are now in progress. Preliminary results of these experiments indicate that the most interesting data can be obtained in the case of a combined action of electric and magnetic fields upon the relaxor under conditions where EL is excited as described in [3].

Acknowledgments. The authors are grateful to O.E. Kvyatkovskiĭ for fruitful discussions of results.

This study was supported by the Russian Foundation for Basic Research, project no. 01-02-17801.

REFERENCES

1. S. A. Gridnev, K. S. Drozhdin, and V. V. Shmykov, Fiz. Tverd. Tela (St. Petersburg) **42**, 318 (2000) [Phys. Solid State **42**, 326 (2000)].
2. S. A. Flerova, *Author's Abstract of Doctoral Dissertation* (Kiev, 1994).
3. S. A. Flerova and N. N. Kraĭnik, Izv. Ross. Akad. Nauk, Ser. Fiz. **64**, 1203 (2000).

Translated by P. Pozdeev

Technical Physics Letters, Vol. 29, No. 1, 2003, pp. 64–65. Translated from Pis'ma v Zhurnal Tekhnicheskoĭ Fiziki, Vol. 29, No. 2, 2003, pp. 50–54.
Original Russian Text Copyright © 2003 by Vettegren, Bashkarev, Danchukov, Morozov.

The Kinetics of Steel Corrosion in Sea Water

V. I. Vettegren[a]*, A. Ya. Bashkarev[b], K. G. Danchukov[b], and G. I. Morozov[a]

[a] *Ioffe Physicotechnical Institute, Russian Academy of Sciences, St. Petersburg, 194021 Russia*

** e-mail: Victor. Vettegren@pop.ioffe.rssi.ru*

[b] *St. Petersburg State Technical University, St. Petersburg, Russia*

Received July 5, 2002

Abstract—The kinetics of corrosion damage accumulation in stainless steels of various systems was studied using samples exposed in a model aqueous NaCl solution and in sea water. The time variation of the degree of corrosion damage corresponds to a reaction of the first order. The values of the corrosion activation energy and a parameter characterizing protective properties of a protective film on the metal surface are determined.
© 2003 MAIK "Nauka/Interperiodica".

Despite much experience gained in investigations of the corrosion of steels and alloys [1–4], no properly justified methods for the description of metal corrosion have been developed so far. The existing approaches are essentially empirical, based on the choice of interpolation functions providing for the best fit to experimental data [3]. The main reason for this situation is the complexity of corrosion mechanisms.

The aim of our study was to determine the kinetics of corrosion of various steels in a NaCl solution and in sea water. We have established that this process is well described by an equation of the first-order reaction kinetics.

The experiments were performed with samples of steels belonging to the following systems: Cr–Ni–Mo–Ti, Cr–Ni–Mn–N–V, Cr–Ni–N–Mn–Mo, Cr–Ni–Nb, Cr–Ni–Ti, Cr–Mn–Ni, Mn–Al–Nb–Si, Mn–Cr–Al–Si, and Mn–Al–Si. The degree of corrosion damage was evaluated using characteristics taking into account the form, extent, and scale of the defects [4].

We have performed two series of corrosion tests. In the first series, the samples of steels with differently finished surfaces were exposed in a 3% NaCl solution, while samples of the second series were tested in water taken from the Black Sea.

The curves reflecting time variation of the corrosion damage were of the two main types. Most frequently, the corrosion rate exhibited a tendency to decrease with time (Fig. 1). This shape of the kinetics was frequently reported previously for the corrosion of steels tested in humid air or in liquid corrosive media [1–4]. In a smaller number of cases, the rate of corrosion increased with time according to an approximately linear law (Fig. 2).

As is known, the corrosion of steels leads to the formation of a surface layer of iron oxides hindering the access of oxygen to the metal [1–4]. As a result, the rate of corrosion gradually decreases. Under the conditions of deficit in one of the reagents, the time variation of the concentration of corrosion products can be approximately described by an expression corresponding to the first-order reaction kinetics [6],

$$B(t) = B_\infty(1 - \exp(-k_c t)), \qquad (1)$$

where B_∞ is the product concentration in the limit as $t \longrightarrow \infty$ and k_c is the reaction rate constant. The latter quantity is related to the corrosion activation energy U_{0C} and temperature T by the well-known Arrhenius law

$$k_c = k_0 \exp\left(-\frac{U_{0C}}{k_B T}\right), \qquad (2)$$

where $k_0 \approx 10^{-2}$ s^{-1} [1, 5] is a preexponential factor and k_B is the Boltzmann constant.

In cases when the oxide layer only slightly decreases oxygen supply to the surface (i.e., the B_∞

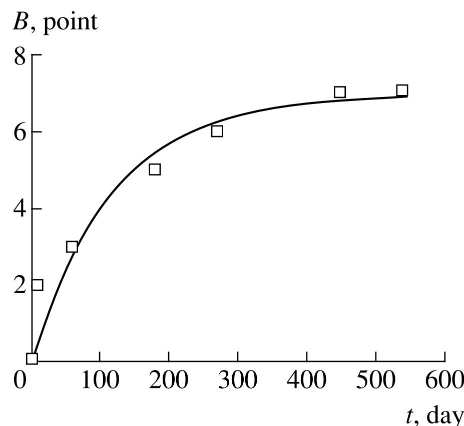

Fig. 1. The plot of corrosion rate of a Cr–Ni–Mn–N steel versus time of exposure in the water of Black Sea.

1063-7850/03/2901-0064$24.00 © 2003 MAIK "Nauka/Interperiodica"

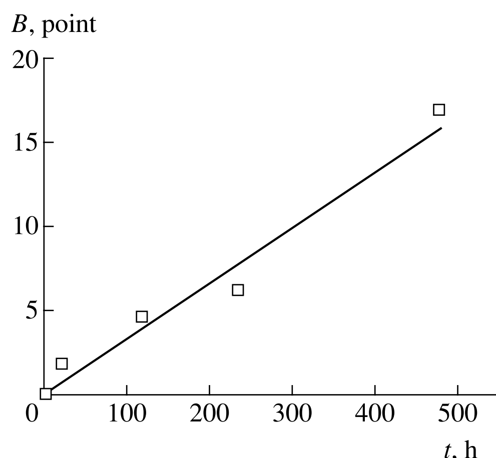

Fig. 2. The plot of corrosion rate of a Cr–Ni–Ti steel versus time of exposure in a 3% NaCl solution.

value is large), the concentration of reaction products increases approximately in proportion to time:

$$B(t) = B_\infty k_c t. \quad (3)$$

Expressions (1) and (3) well describe the experimental corrosion damage kinetics. This is illustrated in Figs. 1 and 2, where solid curves show the $B(t)$ values calculated using these formulas. Therefore, the corrosion resistance of steels is characterized by the two main values: activation energy U_{0C} and constant parameter B_∞. The former quantity depends on the mechanism of corrosion and is related to the anodic current in the corrosion cell, while the latter quantity reflects protective properties of the film of corrosion products formed on the metal surface.

Table 1. The values of activation energies U_{0C} and limiting damage B_∞ for steel samples with different surface finish tested in a 3% NaCl solution

Steel system	Surface treatment	U_0, kJ/mol	B_∞, point
Cr–Ni–Nb	Sandblasting	48 ± 2	100 ± 23
Cr–Ni–Ti		63 ± 2	92.5 ± 9
Cr–Ni–Ti	Electropolishing	55 ± 1	20 ± 6
Cr–Mn–Nb		55 ± 2	33 ± 1.8
Mn–Al–Si		54 ± 1	81 ± 2.4
Mn–Al–Ni–Si		59 ± 1	>100

Table 2. The values of activation energies U_{0C} and limiting damage B_∞ for steel samples with different surface states tested in the water of Black Sea

Steel system	U_0, kJ/mol	B_∞, point
Mn–Cr–Al–Si	59 ± 1	8.5 ± 0.1
Cr–Bi–Mn–Ti	60 ± 2	7.5 ± 0.4
Cr–Ni–Mn–N–V	62 ± 2	7 ± 0.6
Cr–Ni–Mn–Mo	66 ± 1	3.5 ± 0.4
Cr–Ni–N–Mn–Mo (with SMT-11 lubricant)	66 ± 2	2 ± 0.1

The values of U_{0C} and B_∞ for the steels studied are given in Tables 1 and 2. As can be seen from these data, electropolishing of the samples increases the corrosion activation energy, probably due to modification of the steel surface composition. Replacing Nb by Ti in the steel composition does not affect the rate of corrosion damage (U_{0C} and B_∞ values remain unchanged to within the experimental error). Apparently, this substitution changes neither the anodic current nor the properties of the protective oxide film. At the same time, the corrosion activation energy decreases when Ni is replaced by Nb (Table 1).

Steels of the Cr–Mn–Nb and Mn–Al–Si systems possess like activation energies U_{0C}, which implies that the anodic corrosion currents are approximately the same. However, the oxide film formed on the former steel is considerably more compact as compared to that on the latter, as reflected by the B_∞ value (the latter case being five times smaller than in the former). A lubricant applied onto the surface of samples of Cr–Ni–N–Mn–Mo did not change the corrosion activation energy, but decreased the B_∞ value approximately by half (Table 2) because the lubricant layer creates an additional barrier to the diffusion of oxygen molecules.

Thus, the degree of corrosion damage for high-alloy steels exposed in sea water and NaCl solutions varies with time as described by Eq. (1) for the first-order reaction kinetics. The rate of corrosion depends on the two parameters: activation energy U_{0C} and limiting product concentration B_∞.

Acknowledgments. This study was supported by the Ministry of Education of the Russian Federation (project no. E00-4.0-21).

REFERENCES

1. H. H. Uhlig and R. W. Revie, *Corrosion and Corrosion Control. An Introduction to Corrosion Science and Engineering* (Wiley, New York, 1985).
2. M. O. Speidel and M. W. Hitt, in *Advances in Corrosion Science and Technology: Corrosion Cracking of Metals* (Metallurgiya, Moscow, 1985).
3. L. Ya. Tsikerman, *Long-Term Ground Corrosion Forecast for Metals* (Nedra, Moscow, 1966).
4. *Protection of Apparatuses, Equipment, and Structures against Corrosion, Aging, and Biological Damage: A Handbook*, Ed. by A. A. Gerasimenko (Mir, Moscow, 1987).
5. V. A. Bershteĭn, *Mechanohydrolytic Processes and Strength of Solids* (Nauka, Leningrad, 1987).
6. N. M. Emanuel' and D. G. Knorre, *Chemical Kinetics: Homogeneous Reactions* (Vysshaya Shkola, Moscow, 1969; Wiley, New York, 1973).

Translated by P. Pozdeev

Technical Physics Letters, Vol. 29, No. 1, 2003, pp. 66–68. Translated from Pis'ma v Zhurnal Tekhnicheskoĭ Fiziki, Vol. 29, No. 2, 2003, pp. 55–61.
Original Russian Text Copyright © 2003 by Gall', Rut'kov, Tontegode.

Thermal Transformation of C_{60} Molecules Adsorbed on a Silicon Film on $(10\bar{1}0)$ Rhenium Surface

N. R. Gall', E. V. Rut'kov, and A. Ya. Tontegode

Ioffe Physicotechnical Institute, Russian Academy of Sciences, St. Petersburg, 194021 Russia

e-mail: gall@ms.ioffe.rssi.ru

Received June 18, 2002

Abstract—The thermal transformation of a layer of fullerene C_{60} molecules adsorbed on a silicon film deposited onto a $(10\bar{1}0)$Re surface was studied in a temperature range from 300 to 1400 K. It is shown that this temperature interval can be divided into four regions, each being characterized by its own dominating process in the adlayer. © *2003 MAIK "Nauka/Interperiodica".*

Investigations into the interaction of fullerenes with various substances, in particular, with solid surfaces, are important from the standpoint of both practical applications and basic science. The interactions of fullerenes with clean solid surfaces was studied in sufficient detail (e.g., for silicon [1–5], noble metals [6–8], and refractory metals [9–15]), but thin-film systems as substrates for fullerenes have remained virtually uninvestigated. However, such systems can be promising in various applications, for the most part, owing to a variety of physicochemical properties.

Previously, it was established that adsorbed C_{60} molecules retain the fullerene structure on the surfaces of Si, Ir, Re, and Mo heated up to a certain temperature depending on the particular substrate (e.g., ~800 K for Re [12] and ~1000 K for IR [10]). At higher temperatures, the adsorbed fullerene molecules decompose and the carbon atoms liberated in the adlayer dissolve in the bulk substrate (e.g., in Re and Mo) or exhibit graphitization (on Ir).

The aim of this work was to study the temperature-induced transformations in a layer of C_{60} fullerene molecules adsorbed on a complex structure representing a thin silicon film on a $(10\bar{1}0)$Re substrate and to determine the sequence of processes taking place in the system.

Experimental methods. The experiments were performed under ultrahigh vacuum (UHV) conditions ($p \sim 1 \times 10^{-10}$ Torr) in a high-resolution Auger electron spectrometer [16]. The instrumental facilities allowed the Auger electron spectra to be measured immediately on a sample heated to any temperature in the range from 300 to 2100 K. The samples were based on dc-heated thin rhenium ribbons with dimensions of $0.02 \times 1 \times 40$ mm and a $(10\bar{1}0)$ surface orientation, which were thoroughly cleaned from impurities by high-temperature annealing (~2500 K) for several hours under UHV conditions. The Auger electron spectra of samples measured after this treatment displayed only the characteristic peaks of rhenium.

A silicon layer was deposited onto the rhenium substrate by sublimation from a silicon ribbon as described in [17]. During deposition, it was possible to control the absolute value of the flux of silicon atoms. Subsequently, C_{60} fullerene molecules were deposited onto the entire sample surface from a Knudsen cell as described in [14]. After training, the cell provided for a stable and readily controlled flux of fullerene molecules with a density of $\nu = 10^{10}$–10^{13} cm^{-2} s^{-1}. The absolute amount of adsorbed fullerene was also determined as described in [14]. The fullerene adsorbed on the sample surface was distinguished from the other possible forms of carbon by using the specific shape of the C*KVV* Auger peak. This peak also allowed the chemical state of adsorbed C_{60} molecules to be characterized as proposed in [10].

Interaction of silicon with a $(10\bar{1}0)$Re surface. This interaction was described in detail previously [17]. The room-temperature deposition of Si atoms leads to an almost layer-by-layer growth of a silicon film. The resulting multilayer (5- to 10-monolayer-thick) silicon films on the rhenium surface are thermally stable on heating up to a temperature of 800–900 K. On heating above these temperatures, there begins an intense reactive diffusion with the formation of bulk silicides. The silicide composition depends on the annealing temperature and changes from $ReSi_2$ ($T \sim 900$ K) to Re_2Si ($T \sim 1250$ K). At still higher temperatures, the bulk silicides are unstable: all the excess silicon tends to enter a solid solution with a very small concentration, leaving only a surface silicide layer with a concentration of $N_{Si} = 1.3 \times 10^{15}$ cm^{-2}. This surface silicide decomposes only as a result of the silicon thermodesorption at 1500–2000 K.

1063-7850/03/2901-0066$24.00 © 2003 MAIK "Nauka/Interperiodica"

Results and discussion. As is known, the deposition of C_{60} molecules onto a single crystal silicon surface leads to the growth of crystallites above the first monolayer of fullerene molecules. Apparently, an analogous growth mechanism is operative in a layer of C_{60} molecules adsorbed on a silicon film deposited onto a metal substrate. The assumption is confirmed by the kinetics (characteristic of this mechanism) of the Auger signals of carbon and silicon observed upon fullerene adsorption. The corresponding film structure is schematically depicted in Fig. 1*A*.

Figure 2 shows the temperature-induced variation of the intensity of Auger signals of carbon and silicon observed in the course of annealing of a thick film of fullerite deposited at room temperature onto a multilayer ($N_{Si} \sim 7 \times 10^{15}$ cm^{-2}) silicon film. According to our estimates, the average surface concentration of fullerene in this film is $\sim 4 \times 10^{14}$ cm^{-2}. The time of annealing at each temperature was 30 s (longer anneals did not produce significant changes in the Auger signals). As can be seen, heating the samples up to a temperature of about 750 K (region *A* in Fig. 2) does not lead to any change in intensities of the Auger signals from adsorbate and substrate. The energy position (269 eV) of the Auger peak of carbon confirms that the sample surface is covered with C_{60} molecules.

In the temperature interval from 750 to 800 K (region *B* in Fig. 2), the intensity of the carbon signal decreases to 20%; the signal of silicon also slightly drops in intensity. This temperature interval corresponds to the onset of thermodesorption of fullerene molecules from the second and subsequent monolayers. Apparently, such thermodesorption also takes place in our samples, while C_{60} molecules of the first monolayer are not desorbed and remain on the surface. A decrease in the signal of silicon is probably related to the onset of the reactive diffusion of Si atoms inward the bulk metal substrate with a silicide formation. Thus, the temperature of the onset of silicide formation coincides with that in the pure Re–Si system, which indicates that this process is independent of the presence of fullerenes on the surface. These processes are schematically illustrated in Fig. 1*B*.

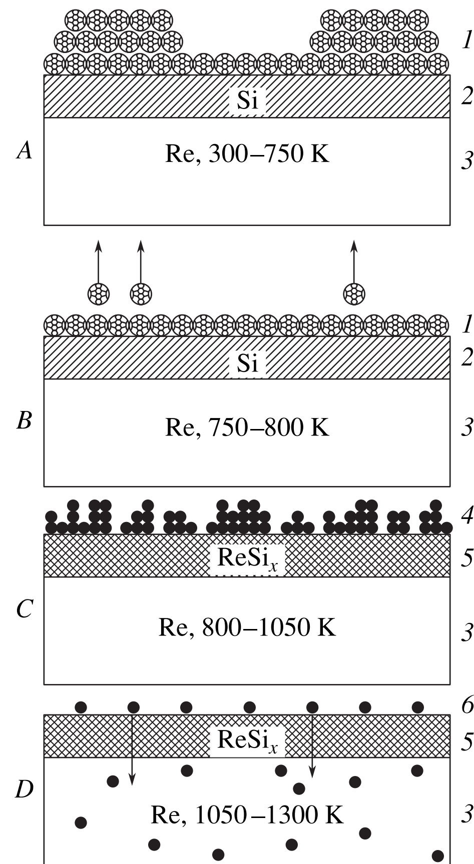

Fig. 1. Schematic diagrams illustrating the sequence of processes during the annealing of a layer of C_{60} molecules adsorbed on a silicon film deposited onto a $(10\bar{1}0)$Re substrate surface: (*A*) T = 300–750 K, a thermally stable fullerene C_{60} film exists on silicon; (*B*) 750–800 K, thermodesorption of fullerene molecules from the second and subsequent monolayers; (*C*) 800–1050 K, transformation of the remaining C_{60} molecules into carbon clusters of a nonfullerene nature and silicide formation; (*D*) 1050–1300 K, complete decomposition of the surface clusters and dissolution of the liberated carbon atoms in the bulk metal; (*1*) C_{60} molecules; (*2*) multilayer silicon film; (*3*) rhenium substrate; (*4*) carbon clusters; (*5*) rhenium silicide layer; (*6*) separate carbon atoms.

As the temperature is increased from 800 to 1050 K (region *C* in Fig. 2), the intensity of the Auger signal from carbon remains unchanged. This is evidence of a constant carbon content on the surface. Apparently, this region features gradual decomposition of C_{60} molecules in the first monolayer, with their conversion into carbon clusters possessing a structure significantly different from that of fullerenes (Fig. 1*C*). Indeed, the shape of the C*KVV* Auger signal is no longer like that of fullerenes: a component peaked at 251 eV becomes well pronounced, while the main peak energy shifts to 270 eV. Analogous processes take place on the surface of single crystal silicon. However, the signal shape also differs from that of carbide and indicates the presence of strong C–C bonds [18]. The intensity of the Auger peak of silicon keeps decreasing, which is evidence of continuing silicide formation. The same is confirmed by the appearance of the Auger signal of rhenium on an almost background level (Fig. 2, region *C*).

Finally, heating the sample to $T > 1050$ K leads to a sharp increase in intensity of the signals from silicon and rhenium, while the signal from carbon decays to zero (region *D* in Fig. 2). The shape of the carbon peak still differs from that typical of carbides. The ratio of intensities of the Auger signals of silicon and rhenium at T = 1300 K corresponds to the formation of a bulk Re_2Si phase [17]. At this temperature, the clusters of adsorbed carbon apparently exhibit final decomposition (loosing memory of their fullerene origin) and dif-

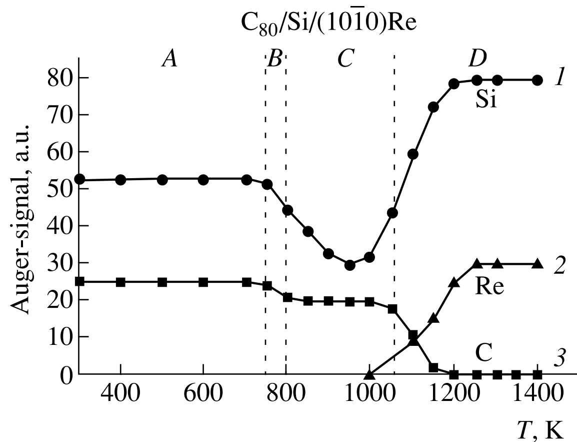

Fig. 2. Variation of the Auger signals of (*1*) silicon, (*2*) rhenium, and (*3*) carbon during the annealing of a fullerene C_{60} film (with an average thickness of two monolayers) adsorbed at $T = 300$ K on a thin (about six monolayers) silicon film on $(10\bar{1}0)$Re surface. Regions *A*–*D* correspond to the events illustrated by Figs. 1*A*–1*D*, respectively.

fused through the bulk silicide to dissolve in the substrate. It is interesting to note that neither decay of the carbon clusters nor the diffusion of carbon atoms influence the process of silicide formation. We believe that similar independence of various processes can be expected in other metal–silicon systems with adsorbed fullerene molecules. This pattern is schematically illustrated in Fig. 1*D*.

Conclusions. We have studied the transformation of a layer of fullerene C_{60} adsorbed on a multilayer substrate, representing a silicon film deposited onto a $(10\bar{1}0)$Re surface, in the temperature range from 300 to 1400 K. There are clearly separated stages featuring the existence of a thermally stable fullerene film, thermodesorption of fullerene molecules from the second and subsequent monolayers, transformation of the remaining C_{60} molecules into carbon clusters of a nonfullerene nature, and complete decomposition of these clusters with dissolution of the liberated carbon in the bulk metal. It is shown that these events do not influence the process of silicide formation in the system on heating. We have suggested that similar independence of various processes can be expected in other metal–silicon systems with adsorbed fullerene molecules.

Acknowledgments. This study was supported in part by the Presidium of the Russian Academy of Sciences ("Low-Dimensional Quantum Structures," project 4G19) and by the Ministry of Science and Technology of the Russian Federation ("Controlled Fullerene Synthesis").

REFERENCES

1. Hang Xu, D. M. Chen, and W. N. Creager, Phys. Rev. Lett. **70**, 1850 (1993).
2. Y. Z. Li, M. Chander, J. C. Partin, and J. H. Weaver, Phys. Rev. B **45**, 13837 (1992).
3. T. Sato, T. Sueyoshi, and M. Iwatsuku, Surf. Sci. Lett. **321**, L137 (1994).
4. D. Chen and D. Sarid, Surf. Sci. **319**, 74 (1994).
5. P. H. Beton, A. W. Dunn, and P. Moriarty, Surf. Sci. **361**/**362**, 878 (1996).
6. T. Hashizume, K. Motai, X. D. Wang, *et al.*, J. Vac. Sci. Technol. A **12**, 2097 (1994).
7. T. Chen, S. Howelles, M. Gallager, *et al.*, J. Vac. Sci. Technol. B **9**, 2461 (1991).
8. D. K. Kim, Y. D. Suh, K. H. Park, *et al.*, J. Vac. Sci. Technol. A **11**, 1675 (1993).
9. G. K. Wertheim, Solid State Commun. **88**, 97 (1993).
10. E. V. Rut'kov, A. Ya. Tontegode, and Yu. S. Grushko, Pis'ma Zh. Éksp. Teor. Fiz. **57**, 712 (1993) [JETP Lett. **57**, 724 (1993)].
11. E. V. Rut'kov, A. Ya. Tontegode, and M. M. Usufov, Phys. Rev. Lett. **74**, 758 (1995).
12. N. R. Gall, E. V. Rut'kov, A. Ya. Tontegode, and M. M. Usufov, Mol. Mat. **17**, 187 (1996).
13. N. R. Gall, E. V. Rut'kov, A. Ya. Tontegode, and M. M. Usufov, Pis'ma Zh. Tekh. Fiz. **23** (23), 56 (1997) [Tech. Phys. Lett. **23**, 911 (1997)].
14. N. R. Gall, E. V. Rut'kov, A. Ya. Tontegode, and M. M. Usufov, Zh. Tekh. Fiz. **69** (11), 117 (1999) [Tech. Phys. **44**, 1371 (1999)].
15. N. R. Gall, E. V. Rut'kov, and A. Ya. Tontegode, Fullerene Sci. Technol. **9** (2), 111 (2001).
16. N. R. Gall, S. N. Mikhailov, E. V. Rut'kov, and A. Ya. Tontegode, Surf. Sci. **191**, 185 (1987).
17. N. R. Gall, E. V. Rut'kov, and A. Ya. Tontegode, Zh. Tekh. Fiz. **60** (4), 125 (1990) [Sov. Phys. Tech. Phys. **35**, 475 (1990)].
18. N. R. Gall, E. V. Rut'kov, S. N. Mikhailov, and A. Ya. Tontegode, Poverkhnost, No. 4, 22 (1987).

Translated by P. Pozdeev

Technical Physics Letters, Vol. 29, No. 1, 2003, pp. 69–71. Translated from Pis'ma v Zhurnal Tekhnicheskoĭ Fiziki, Vol. 29, No. 2, 2003, pp. 62–69.
Original Russian Text Copyright © 2003 by Sozaev, Chernyshova.

Surface Energy and Electron Work Function at the Interface of a Thin Alkali Metal Alloy Film and a Dielectric Medium

V. A. Sozaev and R. A. Chernyshova

Kabardino-Balkarian State University, Nal'chik, Kabardino-Balkaria, Russia

Received August 8, 2002

Abstract—The surface energy σ and the electron work function ϕ of a thin film of an alkali metal (or an alloy) in contact with a dielectric medium are calculated by the method of an electron density functional. It is established that both σ and ϕ values decrease with increasing permittivity ε. The $\sigma(\varepsilon)$ and $\phi(\varepsilon)$ functions can be approximated by quadratic polynomials. Irrespective of the permittivity value, there is a linear relationship between σ and ϕ of the alkali metals and alloys studied. © *2003 MAIK "Nauka/Interperiodica".*

Despite numerous theoretical investigations of semiinfinite metals [1–6] and alloys [7–9], our knowledge of the effect of a dielectric medium on the surface properties of metal alloys is still insufficiently complete. However, such data are necessary for the development of systems with matrix-encapsulated nanodimensional objects, micro- and nanoelectronic devices, capillary energy accumulators, etc.

Recently [10], it was demonstrated that a dielectric medium in contact with a nanodimensional object so that there is no charge at the interface leads to a decrease in the surface energy σ and electron work function ϕ of the metal film. However, the relations obtained in [10] did not allow the dependence of σ and ϕ on the permittivity ε of the medium to be found in an explicit form.

In this paper, the surface energy and electron work function of a thin film of an alkali metal or alloy are determined as functions of ε of the medium in a homogeneous background approximation.

The model of a film made of a substitution alloy of the A_xB_{1-x} type was considered in the jelly approximation [11]. The surface segregation effects in a film of thickness L lead to the formation of a surface layer of thickness D in which the positive charge density n_s differs from the bulk value n_0. The film is in contact with an infinite dielectric medium possessing permittivity ε, which is described in the continuum approximation.

In the homogeneous background approximation, the surface energy of the film can be expressed as

$$\sigma_j = 2\int_0^\infty \{\omega[n_-(z)] - \omega[n_+(z)]\}dz + \int_0^\infty \varphi(z)[n_-(z) - n_+(z)]dz, \quad (1)$$

where $\omega[n(z)]$ is the energy density of an inhomogeneous electron gas. This value includes the density of the kinetic energy of the noninteracting electron gas (corrected for the field inhomogeneity) and the density of the exchange-correlation interaction (corrected for a nonlocal character of this interaction).

The electron density profile at the film–dielectric interface is described by the function

$$n_-(z) = n_0\begin{cases} 1 - \exp(-\beta Z_G)\cosh(\beta z), & z < Z_G, \\ \sinh(\beta Z_G)\exp(-\beta Z), & z > Z_G, \end{cases} \quad (2)$$

where Z_G is the coordinate of the Gibbs interface determined from the condition of electroneutrality of the system; β is the variation parameters determined from the condition of minimum surface energy σ_j; and z is the coordinate along the normal to the metal surface, measured from the middle of the film.

The electrostatic potential $\varphi(z)$ at the interface is determined from the Poisson equation, written as

$$\Delta\varphi = -4\pi[n_-(z) - n_+(z)] \quad (3)$$

and solved taking into account the boundary and continuity conditions for $\varphi(z)$ and $\varphi'(z)$ on the film surfaces. Expressions for $\varphi(z)$ are presented elsewhere [11].

The work function of an electron escaping from the film surface into the dielectric medium is calculated by a formula derived using the sum rule [4],

$$\phi_j = \varphi(L/2 - D) - n_s/(n_0)[\varphi(L/2) - \varphi(L/2 - D)] + (\varepsilon - 1)(4\pi q_s)^2/(8\pi\varepsilon n_0) - E(n_0), \quad (4)$$

where q_s is the electric charge density at the interface.

For the model under consideration, it was assumed that $q_s = 0$, D is the segregated layer thickness, n_0 and n_s are the positive charge densities in the surface layer and in the bulk of the film, respectively, and $E(n_0)$ is the total density of the kinetic, exchange, and correlation energies. The quantities $\varphi(L/2)$ and $\varphi(L/2 - D)$ are the values of the electrostatic potential $\varphi(z)$ on the boundary planes $z = L/2$ and $z = L/2 - D$, respectively:

$$\varphi(L/2 - D) = 4\pi n_0/(\beta^2)\exp(-\beta Z_G)\cosh(\beta(L/2 - D)) + C_1,$$

$$\varphi(L/2) = 4\pi n_0/(\beta^2)\exp(-\beta Z_G)\cosh(\beta L/2) - \pi(n_0 - n_s)L^2/2 + 2\pi(n_0 - n_s)(L/2 - D)L + C_2,$$

$$C_1 = C_2 - 2\pi(n_0 - n_s)(L/2 - D)^2,$$

$$C_2 = -4\pi n_0/(\beta^2)\exp(-\beta Z_G)\cosh(\beta L/2)(1 - 1/\varepsilon) - 2\pi(n_s - n_0)(L/2)^2 - 2\pi(n_s - n_0)(L/2 - D)L - \pi n_0 L^2/\varepsilon + 2\pi n_0 Z_G L/\varepsilon + C_3,$$

$$C_3 = -4\pi n_0/(\varepsilon\beta^2) - 2\pi n_0 Z_G^2/\varepsilon.$$

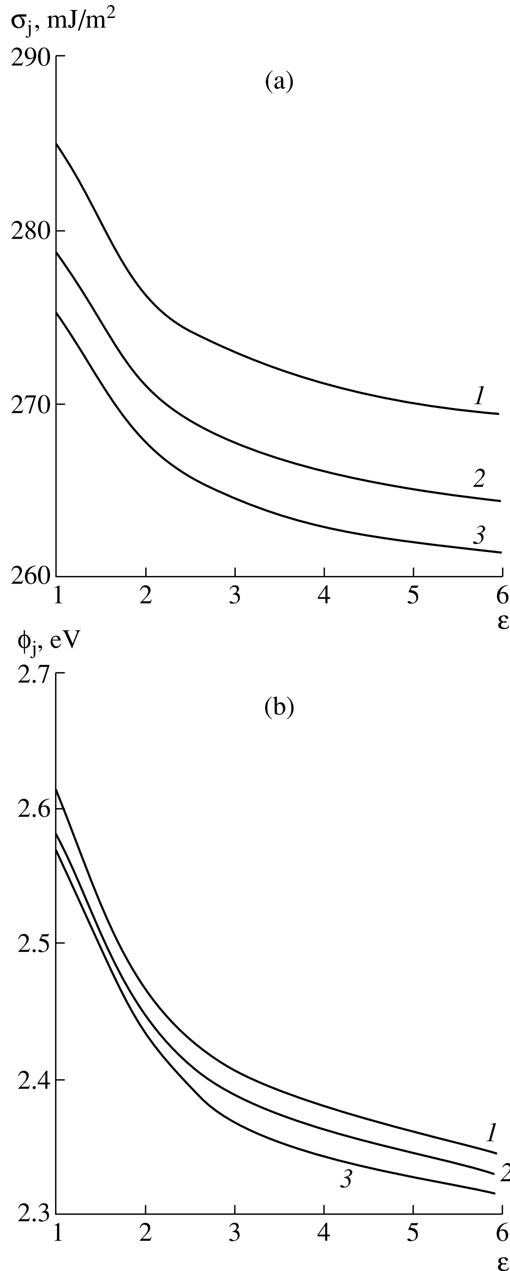

Fig. 1. The plots of (a) surface energy σ_j and (b) electron work function ϕ_j versus permittivity of the dielectric medium for thin $Na_{0.5}K_{0.5}$ alloy films of various thicknesses $L = 10a_0$ (*1*), $15a_0$ (*2*), and $20a_0$ (*3*), where a_0 is the Bohr radius.

Figure 1 shows the results of calculations performed for a $Na_{0.5}K_{0.5}$ alloy using the above formulas in an interval of ε from 1 to 6. As can be seen from these data, both σ and ϕ values decrease with increasing permittivity. Treatment of the $\sigma(\varepsilon)$ and $\phi(\varepsilon)$ functions by least squares yields approximate relations

$$\sigma(\varepsilon) = A + B\varepsilon + C\varepsilon^2, \quad (5)$$

$$\phi(\varepsilon) = A^* + B^*\varepsilon + C^*\varepsilon^2. \quad (6)$$

The results of calculations for σ_j and ϕ_j were used to construct a plot of σ_j versus ϕ_j for pure alkali metals

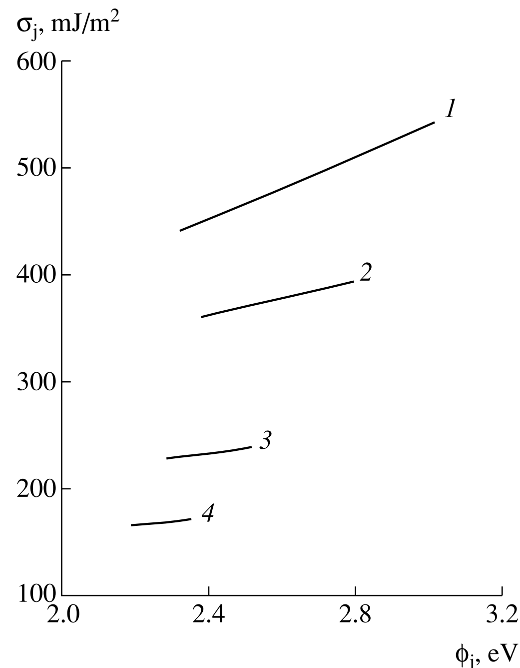

Fig. 2. The plots of surface energy σ_j versus electron work function ϕ_j for thin ($L = 15a_0$) films of alkali metals: (*1*) Li; (*2*) Na; (*3*) K; (*4*) Cs.

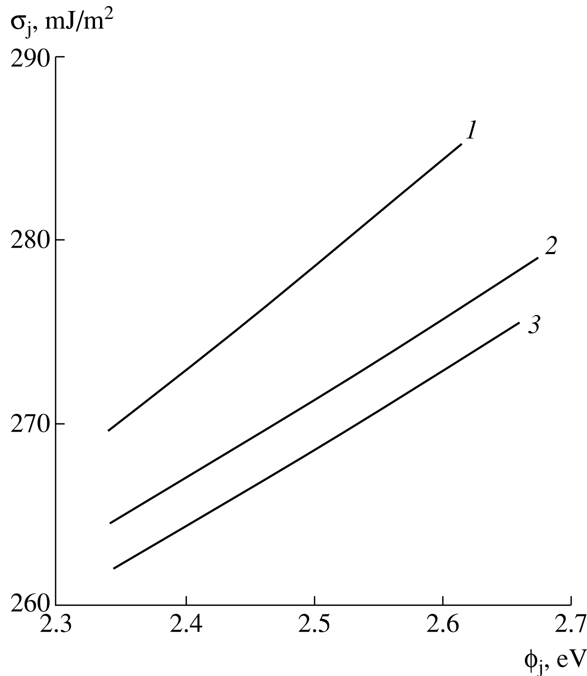

Fig. 3. The plots of surface energy σ_j versus electron work function ϕ_j for thin $Na_{0.5}K_{0.5}$ alloy films of various thicknesses $L = 10a_0$ (*1*), $15a_0$ (*2*), and $20a_0$ (*3*).

(Fig. 2) and the $Na_{0.5}K_{0.5}$ alloy (Fig. 3). As can be seen from Figs. 2 and 3, there is a linear relation between the surface energy σ_j and the electron work function ϕ_j of the films of alkali metals and alloys. Such relations were previously established for pure bulk metals [12]. To our knowledge, the linear relations between σ_j and ϕ_j in thin films are reported for the first time.

The data in Fig. 2 and in the table show that the passage from lithium to cesium (accompanied by an increase in the atomic radius) leads to an increase in slope of the σ_j versus ϕ_j plots, in agreement with the results for pure bulk metals [12]. Thus, our estimates for σ_j and ϕ_j values indicate that linear relations between the surface energy and the electron work function of a metal film are retained on passage to layer thicknesses in the nanometer range, irrespective of the parameters of the dielectric medium in contact with the film.

The values of coefficients in the relation $\sigma_j = A + B\varphi_j$ for alkali metal films

Metal or alloy	Film thickness a_0, nm	A	B	k
Li	15	98.67	147.98	0.9980
Na	15	161.16	83.77	0.9996
K	15	125.56	45.03	0.9984
Cs	15	90.73	34.34	0.9983
$Na_{0.5}K_{0.5}$	10	134.88	57.47	0.9930
$Na_{0.5}K_{0.5}$	15	133.22	56.37	0.9989
$Na_{0.5}K_{0.5}$	20	134.00	54.94	0.9988

REFERENCES

1. S. N. Zadumkin and A. A. Karashaev, Fiz.-Khim. Mekh. Mater., No. 2, 139 (1965).
2. V. F. Ukhov, R. M. Kobeleva, G. V. Dedkov, and A. I. Temrokov, *Electron-Statistical Theory of Metals and Ionic Crystals* (Nauka, Moscow, 1982).
3. M. B. Partenskii and V. E. Kuzeme, Fiz. Tverd. Tela (Leningrad) **21**, 2842 (1979) [Sov. Phys. Solid State **21**, 1639 (1979)].
4. M. B. Partenskii, Poverkhnost, No. 10, 25 (1982).
5. R. M. Digilov, V. A. Sozaev, and Kh. B. Khokonov, Poverkhnost, No. 12, 138 (1987).
6. A. N. Vakilov and V. V. Prudnikov, Fiz. Met. Metalloved., No. 8, 11 (1991).
7. R. M. Digilov and V. A. Sozaev, Poverkhnost, No. 4, 22 (1992).
8. S. I. Masharov, V. A. Masharova, A. F. Rybalko, and D. A. Safarov, Poverkhnost, No. 5, 21 (1992).
9. A. B. Alchagirov, V. A. Sozaev, and Kh. B. Khokonov, Zh. Tekh. Fiz. **67**, 133 (1997) [Tech. Phys. **42**, 118 (1997)].
10. A. Z. Kashezhev, A. Kh. Mambetov, V. A. Sozaev, and D. V. Yaganov, Poverkhnost, No. 12, 53 (2001).
11. V. A. Sozaev, V. V. Chernov, R. A. Chernyshova, and D. V. Yaganov, Vestn. Kabard.-Balkar. Gos. Univ., Ser. Fiz. Nauki, No. 4, 20 (2000).
12. V. S. Fomenko, *Emission Properties of Materials: A Handbook* (Naukova Dumka, Kiev, 1981).

Translated by P. Pozdeev

Technical Physics Letters, Vol. 29, No. 1, 2003, pp. 72–74. Translated from Pis'ma v Zhurnal Tekhnicheskoĭ Fiziki, Vol. 29, No. 2, 2003, pp. 70–76.
Original Russian Text Copyright © 2003 by Dmitriev, Kyarginskiĭ, Panas, Puzikov, Starkov.

Ultrawideband Direct Chaotic Data Transmission in the Microwave Range

A. S. Dmitriev, B. E. Kyarginskiĭ, A. I. Panas, D. Yu. Puzikov, and S. O. Starkov

Institute of Radio Engineering and Electronics, Russian Academy of Sciences, Moscow, Russia

e-mail: chaos@mail.cplire.ru

Received September 24, 2002

Abstract—A method of wireless, high-rate, direct chaotic transmission of digital data is proposed. The method is based on the use of ultrawideband chaotic oscillations generated directly in the microwave range. Experimental results are presented to demonstrate the possibility of data transmission at a rate of up to 200 Mb/s.
© *2003 MAIK "Nauka/Interperiodica".*

Dynamic chaos [1–3] possesses a combination of properties making it an attractive carrier for communication systems. These special properties include, in particular, a high potential rate of data transmission, stability of broadband signals with respect to fading in the case of multipath signal propagation, and the possibility of providing confidential (secret) communications (see, e.g., [4–6]).

However, numerous investigations aimed at the application of chaos to solving the problems of data transmission showed that practical realization of the potential advantages of this carrier encounter considerable problems. One of the major reasons for this is that the proposed systems of communication using chaotic signals were based on traditional transceiver schemes, in which chaos was only employed as subcarrier oscillations modulating the high-frequency (or microwave) carrier. This hindered making use of a broadband (ultrawideband) character of chaos, which is one of the most attractive features of chaos capable of providing for extremely high rates of data transmission and formation of large-base signals.

In order to remove this problem, we have recently [7] suggested to pass from the traditional transceiver scheme to a direct chaotic communication system (DCCS) [7]. The DCCS implements the idea of directly generating the data-carrying chaotic oscillations in the microwave range and modulating these oscillations by an information signal [7–10]. One possible method of introducing information into the chaotic carrier consists in the formation of a stream of chaotic rf pulses, the positions of which at certain sites along the stream (i.e., the presence or absence of the information pulses at these sites) provides coding of the transmitted data. In the simplest variant, definite positions are set on the time axis, whereby the presence of a pulse in such position corresponds to transmitting 1, while the absence of pulses in these positions transmits 0. Figure 1a presents a schematic diagram of a direct chaotic data transmission system. Recently [8–10] we reported the experimental results on a broadband (100 MHz) direct chaotic data transmission in a 1-GHz frequency range. The data transmission rate achieved in these experiments

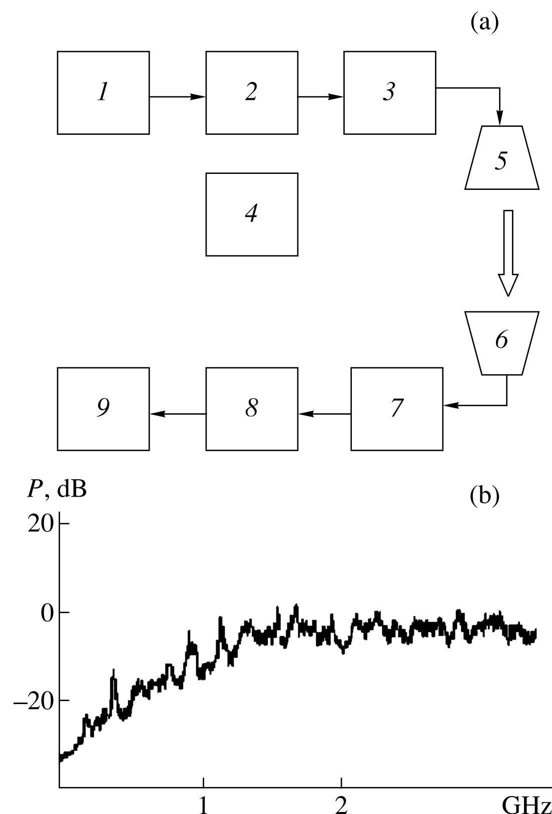

Fig. 1. (a) Schematic diagram of a ultrawideband direct chaotic data transmission line: (*1*) ultrawideband chaotic signal generator; (*2*) modulator; (*3*, *7*) microwave amplifiers; (*4*) digital control signal generator; (*5*, *6*) transmitting and receiving antennas; (*8*) demodulator; (*9*) oscillograph. (b) Output power spectrum of ultrawideband chaotic oscillations.

1063-7850/03/2901-0072$24.00 © 2003 MAIK "Nauka/Interperiodica"

amounted to 70 Mb/s. These data showed a high potential of DCCS and confirmed that a high data transmission rate and stability with respect to fading in the case of multipath signal propagation are inherent in these systems.

This paper is aimed at demonstrating that the principle of direct chaotic data transmission can also be effectively realized using ultrawideband chaotic signals. The existing technologies allow the creation of simple and compact transceivers possessing high communication characteristics. Our experiments were performed with a prototype of the data transmission scheme constructed in accordance with the schematic diagram depicted in Fig. 1a. The transmitter comprises a source of chaos generating a chaotic signal in the frequency range of data transmission (500–3500 MHz), a device controlling the operation mode of the chaotic signal generator, a modulator, microwave amplifiers, and a transmitting antenna.

For the obtaining of ultrawideband oscillations, we developed a chaotic signal generator scheme including three bipolar microwave transistors and two frequency-selective chains. Each of these chains represents a system of coupled microstrip resonators of various lengths with the ends loaded to 2T938A transistors. Figure 1b shows the output power spectrum of the chaotic signal generator operating in one of the typical chaotic regimes. The width of the spectrum on a –20 dB level is 3 GHz. The average output power of the generator is about 10 mW.

The modulator is a device providing commutation of the chaotic microwave signal. This device possesses input and output for the chaotic carrier and a control input to which the binary information code is supplied. The commutation function in the modulator is performed by p-i-n diodes. When a voltage of ~5 V (logical unity) is applied to the control input, the modulator transmits a chaotic signal from the generator. If the control signal level is zero (logical zero), the modulator is closed and the chaotic signal is not transmitted. Thus, a two-level information signal applied to the control input of the modulator yields a stream of chaotic rf pulses at the output.

The prototype transceiver employed two microwave amplifiers. The first of these performed, besides the amplification function, the role of a buffer between the chaotic signal generator and the modulator. The amplifiers were built around a microassembly of the MGA 81563 type and provided for an amplification level of 10–15 dB. The signals were transmitted and received by ultrawideband disk-cone antennas possessing linear phase characteristics. The receiver consists of an antenna and a demodulator comprising the input microwave amplifier with a gain of 10 dB, a detector, and a dc amplifier. The detector represents a balanced amplifier implemented on 2T3132A bipolar transistors one of which operates in the detector mode. A signal from the detector output enters the dc amplifier (with a gain of 20 dB), from which the signal is transmitted to an oscillograph.

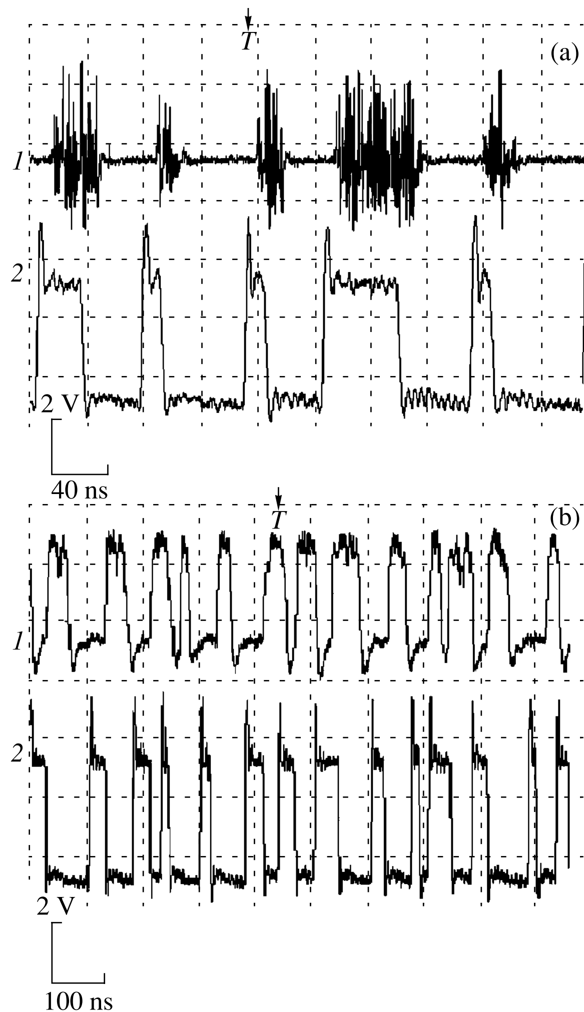

Fig. 2. (a) The formation of a stream of chaotic rf pulses for the data transmission at a rate of 100 Mb/s (bottom fragment shows the initial information stream; top fragment shows the corresponding chaotic rf pulses); (b) the results of experiments with ultrawideband direct chaotic data transmission (bottom fragment shows the initial 100 Mb/s digital stream; top fragment shows the envelope obtained in the receiver).

The aim of these experiments was to demonstrate the possibility of a high-rate transmission of digital data by means of the ultrawideband chaotic carrier. The experiments were conducted in a wide range of control pulse durations, which corresponded to various data transmission rates. The pulsed signal generator allowed the control pulse duration to be varied from 100 to 3 ns. It was also possible to form pulse trains with variable numbers of pulses and the on/off ratio. We have also performed experiments on the transmission of real information signals taken from a PC card.

The first series of experiments was performed with relatively long pulses (20–100 ns), which corresponded to a data transmission rate from 10 to 50 Mb/s. When

the chaotic carrier was modulated by a pulse train, the envelope of the stream of chaotic rf pulses at the demodulator output was measured with the oscillograph. In this interval of the control pulse durations, the envelope of the stream of chaotic rf pulses at the demodulator output reproduced the modulating pulse stream with a good precision.

In the subsequent series of experiments, the control pulse duration was varied within 3–15 ns, which corresponded to a data transmission rate from 70 to 350 Mb/s. However, the available pulse generator could produce pulses of the required shape (rectangular) and amplitude (5 V) only for a duration of not less that 5 ns. In the 5–15 ns interval, the envelope of the stream of chaotic rf pulses at the demodulator output also reproduced well the modulating pulse stream. Figure 2b shows an example of the modulating signal corresponding to a data transmission rate of 100 Mb/s and the corresponding stream of chaotic rf pulses. The spectral characteristics of the initial (transmitted) and received ultrawideband carrier practically remained unchanged with respect to the chaotic signal spectrum at the generator output (Fig. 2a).

As can be seen from Fig. 2b (cf. upper and lower oscillograms), the receiver signal (representing envelope of a ultrawideband signal taken from the demodulator output) reproduced well both the shape and structure of the initial (transmitted) data stream. The bottom fragment of the oscillograms corresponds to the shape of the initial data stream envelope, while the top fragment represents the signal at the output of demodulator.

Thus, the experiments with a prototype demonstrated the possibility of high-rate data transmission. This, in combination with other advantages of the ultrawideband direct chaotic schemes, such as stability of the broadband signals with respect to fading in the case of multipath signal propagation and the possibility of a flexible control of the signal base, makes these schemes a promising technology for digital wireless communication systems.

Acknowledgments. The authors are grateful to Yu.V. Andreev, L.V. Kuz'min, N.P. Chubinskiĭ, and A.G. Chernokalov for their help in planning experiments and for discussion of results.

REFERENCES

1. V. S. Anishchenko, *Complex Oscillations in Simple Systems* (Nauka, Moscow, 1990).
2. A. S. Dmitriev and V. Ya. Kislov, *Stochastic Oscillations in Radiophysics and Electronics* (Nauka, Moscow, 1989).
3. H. G. Schuster, *Deterministic Chaos* (Physik-Verlag, Weinheim, 1984; Mir, Moscow, 1988).
4. A. S. Dmitriev, A. I. Panas, and S. O. Starkov, Zarubezhn. Radioélektron. Usp. Sovr. Radioélektron., No. 10, 4 (1997).
5. V. D. Shalfeev, G. V. Osipov, A. K. Kozlov, and A. R. Volkovskii, Zarubezhn. Radioélektron. Usp. Sovr. Radioélektron., No. 10, 27 (1997).
6. M. Hasler, Zarubezhn. Radioélektron. Usp. Sovr. Radioélektron., No. 11, 33 (1998).
7. A. S. Dmitriev, B. E. Kyarginskiĭ, N. A. Maksimov, *et al.*, Radiotekhnika **42** (3), 9 (2000).
8. A. S. Dmitriev, B. E. Kyarginskiĭ, N. A. Maksimov, *et al.*, *Direct Chaotic Data Transmission in the Microwave Range*, Preprint IRE RAN No. 1 (625) (Moscow, 2000).
9. A. S. Dmitriev, B. E. Kyarginskiĭ, A. I. Panas, and S. O. Starkov, Radiotekh. Élektron. (Moscow) **46**, 224 (2001).
10. A. S. Dmitriev, A. I. Panas, and S. O. Starkov, *Nonlinear Science Preprint* (nlin. CD/0110047).

Translated by P. Pozdeev

Technical Physics Letters, Vol. 29, No. 1, 2003, pp. 75–77. Translated from Pis'ma v Zhurnal Tekhnicheskoĭ Fiziki, Vol. 29, No. 2, 2003, pp. 77–82.
Original Russian Text Copyright © 2003 by Morozov, Rasulev.

Thermal Spikes Observed during the Tantalum Sputtering by Gold Cluster Ions

S. N. Morozov and U. Kh. Rasulev
Arifov Institute of Electronics, Academy of Sciences of the Republic of Uzbekistan, Tashkent, Uzbekistan
e-mail: ariel@.uzsci.net
Received July 15, 2002

Abstract—The emission of atomic and cluster ions during the sputtering of a tantalum target by gold cluster ions was experimentally studied for primary ion energies ranging from 6 to 21 keV. An increase in the number of atoms in the bombarding cluster ions of gold leads to a considerable increase in the yield of atomic ions of tantalum possessing quasithermal energies. The results provide experimental evidence for the appearance of thermal spikes in the target bombarded with cluster ions, with the corresponding contribution to the emission of atomic ions. *© 2003 MAIK "Nauka/Interperiodica".*

When heavy cluster ions interact with a solid, simultaneous collision of several atoms of a large projectile with a small surface region leads to a sharp increase in the local energy deposition, which results in the development of high-density nonlinear collision cascades. However, an increase in the sputtering coefficient and the yield of secondary cluster ions is not proportional to the number of atoms in the bombarding particle. The corresponding factor of nonadditivity (molecular effect) is rather large [1–3]. There has been a long discussion concerning the existence of the so called "thermal spikes," related to nonlinear cascades, and their possible influence on various emission processes [4, 5]. It was suggested that thermal spikes represent relatively long-lived (up to 10^{-11} s) high-temperature regions adjacent to the surface, and that thermal evaporation of atoms and ions from these regions may contribute to the sputtering and ion emission.

There are numerous experimental data [5] which indicate that the sputtering coefficients significantly exceed the values calculated according to the Sigmund theory [6] in the case of using heavy primary ions (especially molecular ions) and heavy-metal targets. Such cases are characterized by a high density of energy liberated as a result of ion stopping near the target surface. However, the available data do not allow establishing a direct relationship between changes in the sputtering coefficients and secondary ion emission, on the one hand, and the presence of thermal spikes, on the other hand.

We have studied the emission of atomic and cluster ions of tantalum (Ta_n^+) during the sputtering of a tantalum target by gold cluster ions of the Au_m^- type (m = 1–9) with primary energies ranging from 6 to 21 keV. The experimental results show evidence for the presence of thermal spikes in the target bombarded by cluster ions.

The experiments were performed in an experimental setup described in [2], including a source of negative gold cluster ions of the sputtering type, a magnetic separator of primary ions, a polycrystalline tantalum target, and a magnetic secondary-ion mass analyzer based on a mass spectrometer of the MI 1201 type. The original setup was significantly modified in order to increase the mass range and provide for a more correct measurement of the current of primary cluster ions [3]. The tantalum target was bombarded by gold cluster ions at an angle of 45°, while the secondary ions were collected along the normal to the surface, with a positive potential of 2000 V applied to the target. The primary currents of Au_1^-, Au_2^-, Au_3^-, Au_5^-, Au_7^-, and Au_9^- ions measured using a Faraday cup were equal to 1 : 0.22 : 0.35 : 0.035 : 0.012 : 0.005 nA, respectively. The current density of the primary Au_m^- ions on the target varied from 0.3 to 50 nA/cm^2 depending on the m value.

During measurements, the working chamber was pumped only by ion-sublimation pumps which provided a residual pressure not exceeding 3×10^{-6} Pa. The target purity, ensured by using a base working temperature as high as 2300 K during the measurements, was monitored by the presence of Ta_nO^+ ions, the relative content of which did not exceed 0.5% of the total flux of the secondary cluster ions of tantalum. The temperature dependence of the secondary ion yield was measured by adjusting the analyzer to the corresponding mass and rapidly scanning the target temperature (around the base working level) within a time period not exceeding 2–3 s (during which the surface could not be significantly contaminated).

The mass spectra of tantalum cluster ions Ta_n^+ (n = 1–11) were obtained for various energies of the bom-

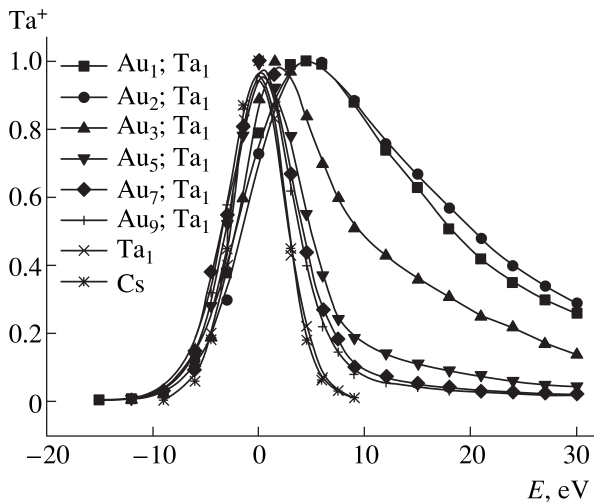

Fig. 1. Relative energy distributions of atomic Ta^+ ions sputtered by gold cluster ions, in comparison with the analogous distributions of evaporated Ta^+ and Cs^+ ions.

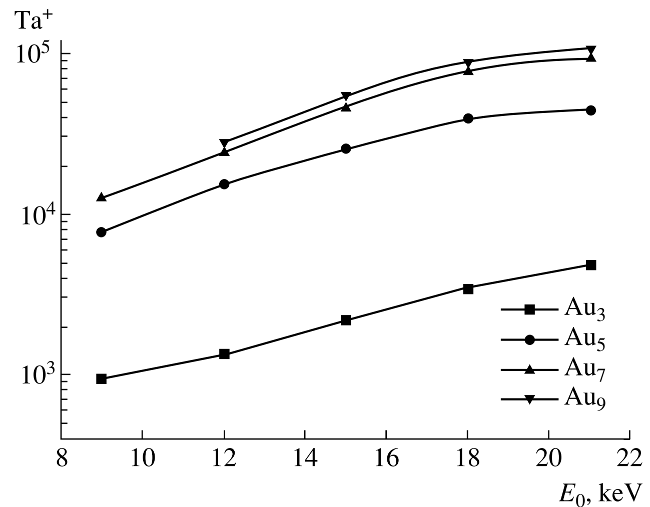

Fig. 2. Dependence of the yield of sputtered quasithermal atomic Ta^+ ions on the energy and size of bombarding Au_m^- clusters.

barding gold clusters Au_m^-. An increase in the number of atoms (m) in the bombarding cluster ions of gold leads to a considerable (nonadditive) increase in the yield of secondary tantalum ions Ta_n^+, whereby the number of atoms in the secondary clusters (n) increased as well. The standard nonadditivity factor determined according to [2] reached a level of 50–100 for $n = 8–11$, $m = 3–5$. We have also observed a sharp increase in the yield of atomic ions (Ta^+) when the number of atoms in the bombarding cluster Au_m^- increased above $m = 3$. An analysis of the experimental relative distributions of the secondary ions with respect to the kinetic energy showed that the increase in the yield of Ta^+ ions with m takes place predominantly due to a growth in the number of ions with energies close to the thermal energy.

Figure 1 shows the relative distributions of the secondary ions with respect to the kinetic energy (ion energy profiles) for the atomic ions of tantalum sputtered by various gold clusters. For comparison, Fig. 1 shows the Cs^+ surface ionization peak and the Ta^+ evaporation peak measured at 2300 K without ion bombardment of the tantalum target. As can be seen, the maximum of the energy distribution of Ta^+ ions sputtered by monomers and dimers is shifted relative to the peak of evaporated ions by 4–5 eV, which amounts to approximately half of the tantalum sublimation energy; the intensity of Ta^+ ions sputtered by monomers and dimmers decreases rather slowly with increasing energy. This behavior is characteristic of the spectra of kinetic energies of the ions sputtered according to the mechanism of collision cascades [6]. As the number of atoms in the bombarding gold clusters Au_m^- increases, the energy distributions of the secondary Ta^+ ions approach the thermal (Maxwell) distributions.

Using the ion energy profiles, it was possible to reliably determine the quasithermal component of the atomic ion emission (by subtracting the usual collision-cascade component characteristic of the bombardment with atomic ions).The quasithermal component is 25% for the bombardment with Au_3^- ions and exceeds 90% of the total yield for the bombardment with Au_9^- clusters. The yield of low-energy atomic ions (reduced to the primary ion current) sharply increases both with the energy of bombarding clusters and with the number of atoms in these clusters (see Fig. 2). The factor of nonadditivity for an increase in the yield of quasithermal Ta^+ ions on passage from Au_3^- to Au_9^- amounts to ~30. This effect possesses a sharply pronounced threshold character and is not observed in the case of bombardment with Au_1^- and Au_2^- ions in the energy range studied. It should be noted that the low-energy component appears only in the spectra of atomic sputtered ions.

Although the yield of secondary cluster ions also exhibits a significantly nonadditive increase with the number of atoms in the bombarding clusters, the shape of their energy spectra remains virtually unchanged. Nor did we observe any correlation between the yield of these ions and the threshold of the appearance of quasithermal atomic ions with respect to the number of atoms in the primary cluster ion. Moreover, as the number of atoms in the gold cluster (projectile) increases, the energy spectra of Ta_n^+ cluster ions (n = 2–11) exhibit broadening and enrich with high-energy particles. This behavior probably indicates that the main mechanism responsible for the formation of sputtered cluster ions is not directly related to their evaporation from the thermal spikes.

The results of measurements of the yield of atomic clusters as a function of the target temperature showed

an almost synchronous monotonic growth in the yield (by a factor of 1.8–2.0) with the temperature increasing in the 300–2300 K range for both quasithermal and collisional components. The relations between these components remained virtually unchanged. Taking into account the experimentally measured relatively weak dependence of the quantum yield of quasithermal sputtered Ta^+ ions on the target temperature and assuming that this temperature adds to the thermal spike temperature, we can estimate the effective temperature T_{eff} in the thermal spikes. With allowance for the well-known exponential character of the temperature dependence of the yield of evaporated ions, we may conclude from the experimental data obtained that the target temperature is a small additive to T_{eff}, so that the temperature in the thermal spikes is much greater than 2300 K.

Thus, our results provide experimental evidence for the existence of thermal spikes in the targets bombarded with cluster ions and for their contribution to the emission of atomic ions.

REFERENCES

1. S. Bouneau, A. Brunelle, S. Della-Negra, *et al.*, Phys. Rev. B **65**, 144106 (2002).
2. S. F. Belykh, B. Habets, U. Kh. Rasulev, *et al.*, Nucl. Instrum. Methods Phys. Res. B **164–165**, 809 (2000).
3. U. Kh. Rasulev and S. N. Morozov, Izv. Ross. Akad. Nauk, Ser. Fiz. **66**, 522 (2002).
4. P. Sigmund and C. Claussen, J. Appl. Phys. **52**, 990 (1981).
5. H. H. Andersen, Mat. Fys. Medd. K. Dan. Vidensk. Selsk. **43**, 127 (1993).
6. P. Sigmund, Phys. Rev. **184**, 383 (1969).

Translated by P. Pozdeev

Technical Physics Letters, Vol. 29, No. 1, 2003, pp. 78–80. Translated from Pis'ma v Zhurnal Tekhnicheskoĭ Fiziki, Vol. 29, No. 2, 2003, pp. 83–87.
Original Russian Text Copyright © 2003 by Chertova.

An Analysis of the Wave Structure of the Defect Field in a Viscoplastic Medium

N. V. Chertova

Institute of Strength Physics and Materials Science, Siberian Division, Russian Academy of Sciences, Tomsk, 634055 Russia

e-mail: chertova@ispms.tsc.ru

Received August 27, 2002

Abstract—The wave structure of a defect field in a viscoplastic medium is studied in terms of equations of defect field theory. It is established that waves in the defect field characterized by tensors of the defect density and the defect flux density possess a transverse character. A relation between the two quantities in a plane harmonic wave is determined. Partial cases of media with strongly and weakly decaying waves are considered.
© 2003 MAIK "Nauka/Interperiodica".

In a continuation of the previous investigation [1], devoted to an analysis of the laws of propagation of plane defect waves in a viscoplastic medium based on defect field theory, let us concentrate on the wave structure. Studying this problem, in addition to its purely methodological significance, is of importance for the following reasons. First, investigation of the wave structure of the defect field is a necessary stage in the further theoretical analysis of the laws of propagation of plane defect waves, in particular, with allowance for the presence of an interface between two viscoplastic media. Second, based on an analysis of the wave structure of a defect field, we can supplement the results of experimental measurements of the rate of plastic distortion by calculating the corresponding components of the dislocation density tensor characterizing the defect structure of a given material [2]. At the same time, these results allow us to estimate the density of dislocations related to the moment stresses [3–4] proceeding from the known plastic deformation rate usually measured in experiment.

The initial system of equations of the defect field theory [1, 5] is as follows:

$$B(\nabla \cdot I) = -P, \quad \nabla \cdot \alpha = 0,$$
$$\frac{\partial \alpha}{\partial t} = \nabla \times I, \quad S(\nabla \times \alpha) = -B\frac{\partial I}{\partial t} - \sigma, \tag{1}$$

where α and I are the tensors of the defect density and the defect flux density, respectively; P and σ are the effective stress and momentum, respectively; B and S are constants quantities determined in defect field theory; and symbols $(\cdot)$ and $(\times)$ denote the scalar and vector products. According to Eqs. (1), the effective stress and momentum meet the consistency condition

$$\frac{\partial P}{\partial t} = \nabla \cdot \sigma, \tag{2}$$

which is the dynamic equilibrium condition in the mechanics of continuum. By definition of a viscoplastic body (for which the stresses depend on the plastic deformation rate [6]), we can write

$$\sigma = \eta I, \tag{3}$$

where, the defect flux density tensor I is determined by the plastic deformation rate β [7],

$$I = -\frac{\partial \beta}{\partial t}, \tag{4}$$

and η is the viscosity coefficient (note that $\alpha = -\nabla \times \beta$). As was noted previously [1], relation (3) can be formally written proceeding from the analogy between Eqs. (1) and the system of Maxwell equations in electrodynamics [8].

By jointly solving Eqs. (1)–(3), it is possible to show that the effective momentum in a viscoplastic medium decays with time according to the law

$$P = P_0 \exp(-t/\tau), \tag{5}$$

where $\tau = B/\eta$ is the relaxation time and P_0 is the initial momentum. The smaller the relaxation time, determined by the quantities characterizing the inertial properties of the ensemble of defects (B) and the viscosity of the medium (η), the faster the momentum decays. Taking into account relations (4) and (5), the initial system (1) can be written as

$$\nabla \cdot I = 0, \quad \nabla \cdot \alpha = 0,$$
$$\frac{\partial \alpha}{\partial t} = \nabla \times I, \quad S(\nabla \times \alpha) = -B\frac{\partial I}{\partial t} - \eta I. \tag{6}$$

Let us consider the defect field in which both tensors α and I depend only on a single spatial coordinate $\xi =$

1063-7850/03/2901-0078$24.00 © 2003 MAIK "Nauka/Interperiodica"

mr and the time t. In this case, each of the nine tensor components α_{ik} satisfies the equation

$$\frac{B}{S}\frac{\partial^2\alpha_{ij}}{\partial t^2} - \frac{\partial^2\alpha_{ij}}{\partial\xi^2} + \frac{\eta}{S}\frac{\partial\alpha_{ij}}{\partial t} = 0. \quad (7)$$

An analogous equation can be written for the components I_{ik} of the defect flux density. As was demonstrated in [1], these equations describe the propagation of two plane harmonic waves

$$\alpha^{1,2} = \alpha e^{i\omega(t \pm \xi/V)}, \quad I^{1,2} = Ie^{i\omega(t \pm \xi/V)} \quad (8)$$

in the $\pm m$ directions at a velocity of

$$V = \sqrt{\frac{S}{B}/\left(1 + \frac{i\eta}{B\omega}\right)}. \quad (9)$$

In order to determine the wave structure of the defect field, let us consider a wave propagating in the m direction. In this case, Eqs. (6) take the form

$$\frac{\partial}{\partial\xi}(mI) = 0, \quad \frac{\partial}{\partial\xi}(m\alpha) = 0,$$
$$\frac{\partial}{\partial\xi}[mI] = \frac{\partial\alpha}{\partial t}, \quad S\frac{\partial}{\partial\xi}[m\alpha] = -B\frac{\partial I}{\partial t} - \eta I. \quad (10)$$

From the first two of these equations, it follows that $\partial_\xi I_{\xi i} = 0$ and $\partial_\xi \alpha_{\xi i} = 0$; this implies that the projections of tensors α and I on the direction of wave propagation are either equal to zero or depend only on time. Taking scalar products of the last two equations by vector m, we obtain

$$\frac{\partial\alpha_{\xi i}}{\partial t} = 0, \quad B\frac{\partial I_{\xi i}}{\partial t} + \eta I_{\xi i} = 0. \quad (11)$$

The first of these equations indicates that the projection of the defect density wave onto the direction ξ is independent of time (so that $\alpha_{\xi i} \equiv 0$). In other words, the defect density wave is a transverse wave and all nonzero components are lying in the wave plane. Using the second equation (11), we arrive at the conclusion that the longitudinal components of the defect flux density tensor decay with time as

$$I_{\xi i} = I_{\xi i}(0)\exp(-t/\tau),$$

so that the wave I in the viscoplastic medium studied is also a transverse wave.

Let us determine a relation between the defect field characteristics in a plane harmonic wave. Substituting solution (8) into the first equation in the second line of (10), we obtain

$$\alpha = [mI]/V. \quad (12)$$

From this equation, is follows that tensors α and I (for the first index) and vector m form an anticlockwise orthogonal triad of vectors. The quantity

$$\frac{1}{V} = \sqrt{\frac{B}{S}\left(1 + \frac{i\eta}{B\omega}\right)} = \sqrt{(1 + i\tan\delta)}/C \quad (13)$$

plays the role of impedance of the medium, and $\tan\delta = \eta/B\omega$ is the loss tangent. Using relation (12), we can determine the ratio of moduli of the defect field parameters

$$\frac{|I|}{\alpha} = |V| = \sqrt{(n^2 + \chi^2)}/C \quad (14)$$

and the phase shift

$$\tan\varphi = \frac{\chi}{n} = \tan(\delta/2), \quad \varphi = \delta/2, \quad (15)$$

where

$$n = (\sqrt{\tan^2\delta + 1} + 1)^{1/2}, \chi = (\sqrt{\tan^2\delta + 1} - 1)^{1/2} \quad (16)$$

are the coefficients of refraction and absorption, respectively, and $C = \sqrt{S/B}$.

Let us consider the limiting cases of large and small losses. For weakly decaying waves ($\tan\delta \ll 1$) propagating in the viscoplastic medium, relations (16) yield $n = 1$, $\chi = (\tan\delta)/2 = \chi(\omega)$, and

$$\frac{|I|}{|\alpha|} = |V| = (\sqrt{1 + \tan^2\delta/4})/C \approx 1/C,$$
$$\tan\varphi = (\tan\delta)/2. \quad (17)$$

In the case of strongly decaying waves, $\tan\delta \gg 1$, $n \approx \chi = \sqrt{(\tan\delta)/2} = \sqrt{\eta/(2B\omega)}$, and

$$\frac{|I|}{\alpha} = |V| \approx \sqrt{\tan\delta}/C, \quad \tan\varphi \approx 1. \quad (18)$$

Note that, for $\tan\delta \gg 1$, the wave process hardly develops because the wave of defects decays over a very short distance

$$d = C/(\chi\omega) = \lambda/(2\pi\chi). \quad (19)$$

Indeed, for $\tan\delta \gg 1$ and $n \approx \chi \gg 1$, this distance is much shorter than the wavelength λ.

In concluding, it is necessary to make two remarks. First, the conditions of strong ($\eta/B\omega \gg 1$) or weak ($\eta/B\omega \ll 1$) decay of the wave process for the given material constants η and B allow us to select the regimes of surface or bulk dynamic action, depending on the frequency. In the case of surface action, the thickness of a plastically deformed layer is determined as $d = \sqrt{2S/(\eta\omega)}$.

Second, the transverse character of the defect density wave is established based on the kinematic identities for the elastic continuum with defect, $\nabla \cdot \alpha = 0$ and $\partial\alpha/\partial t = \nabla \times I$, while material relations determining the properties of the medium were not involved. As for the defect flux density waves, their character is mutually related to the properties of the medium; a transverse character of these waves was only established for the viscoplastic waves under consideration.

Acknowledgments. This study was supported by the Russian Foundation for Basic Research, project no. 02-01-01188.

REFERENCES

1. N. V. Chertova and Yu. V. Grinyaev, Pis'ma Zh. Tekh. Fiz. **25** (18), 91 (1999) [Tech. Phys. Lett. **25**, 756 (1999)].
2. Yu. N. Rabotnov, *Mechanics of Deformed Solids* (Nauka, Moscow, 1979).
3. E. Kroner, Int. J. Eng. Sci. **1**, 261 (1963).
4. Yu. V. Grinyaev and N. V. Chertova, Theor. Appl. Fract. Mech. **28**, 231 (1998).
5. Yu. V. Grinyaev and N. V. Chertova, Fiz. Mezomekh. **3** (5), 19 (2000).
6. P. Perzyna, *Fundamental Problems in Viscoplasticity* (New York, 1966; Mir, Moscow, 1968).
7. A. M. Kosevich, *Foundations of Crystal-Lattice Mechanics* (Nauka, Moscow, 1972).
8. L. D. Landau and E. M. Lifshitz, *Electrodynamics of Continuous Media* (1st ed., Nauka, Moscow, 1970; Pergamon Press, Oxford, 1982).

Translated by P. Pozdeev

Technical Physics Letters, Vol. 29, No. 1, 2003, pp. 8–11. Translated from Pis'ma v Zhurnal Tekhnicheskoĭ Fiziki, Vol. 29, No. 1, 2003, pp. 18–26.
Original Russian Text Copyright © 2003 by Kirdyashev.

On the Interaction of Electromagnetic Radiation with Plasma of an Electric Jet Thruster

K. P. Kirdyashev
Fryazino Branch, Institute of Radio Engineering and Electronics, Russian Academy of Sciences, Fryazino, Moscow oblast, Russia
Received July 23, 2002

Abstract—Experimental data on the amplification of electromagnetic radiation in a plasma of an electric jet thruster are presented. The conditions of anomalous radiation–plasma interaction are established. © *2003 MAIK "Nauka/Interperiodica".*

The problem of electromagnetic compatibility between plasma jet thrusters and other systems of space vehicles is of special importance in designing radioelectronic equipment for communication satellites and spacecraft voyagers exploring cosmic space and planets of the Solar system. The interaction of electromagnetic fields generated by the on-board radioelectronic equipment with the plasma of electric jet thrusters modifies the electromagnetic environment in the vicinity of a spacecraft and alters the conditions of electric signal transmission in radio channels. It is a common approach to consider the attenuation and refraction of radio waves in plasma formations, the fluctuations of signal amplitude and phase in the radio lines, and the directivity pattern distortions and screening of transmitting and receiving antennas [1–4]. However, the interaction of electromagnetic radiation with plasma of an electric jet thruster is by no means restricted to these effects.

Based on the results obtained using a ground stationary plasma thruster (SPT) test system, an additional factor has been found through which an electric jet thruster can influence the electromagnetic situation around a spacecraft. This factor is related to amplification of external electromagnetic radiation in a plasma generated by the thruster. The electromagnetic field acting upon the plasma is generated by various units of the on-board instrumentation complex (microwave transmitting antennas of the space communication systems, parasitic radiation sources unavoidable in any operating radioelectronic equipment).

The effect of the electromagnetic radiation amplification was discovered during ground tests on the SPT modules (of the SPD-70 type) for the Yamal-100 spacecraft [5]. In the SPT operation regimes studied, intensity of the microwave field created inside the vacuum chamber by the on-board radioelectronic equipment exhibited a considerable increase (Fig. 1). The microwave field intensity during the SPT operation was measured by means of a microwave antenna tuned to the frequency range of a heterodyne of the on-board receiver-retransmitter. The intensity of the field acting upon the plasma was changed by attenuating the heterodyne signal at the output of the microwave tract of the retransmitter. Note the nonstationary character of the secondary radiation field, which appears as a sequence of intense pulses in the microwave field envelope with a duration not exceeding 1–10 ms. By connecting the detector input to a matched load and vary-

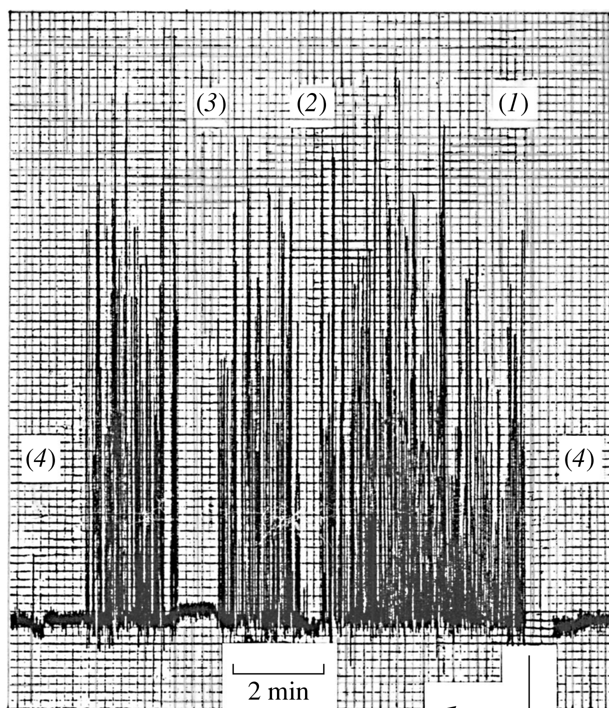

Fig. 1. Typical pattern of microwave signals observed at the measuring receiver output in various operation regimes of a thruster and the on-board radioelectronic equipment: (*1*, *2*) thruster switched on and off, respectively; (*3*) detector input connected to a matched load; (*4*) parasitic heterodyne signal at the receiver input suppressed.

ing the thruster regimes, it was possible to exclude a correlation between the observed effect and the signals directly induced in the measuring circuit by the onboard radioelectronic equipment, so that amplification of the microwave field inside the vacuum chamber could be considered as a result of interaction of the external electromagnetic field (microwave radiation) with the thruster plasma. Taking into account the pulsed character of the secondary radiation and the smoothening action of the measuring instrumentation on the microwave envelope overshoots, the coefficient of amplification of the electromagnetic radiation during thruster operation was estimated as reaching up to 30–35 dB.

A detailed study of the conditions of effective interaction of the microwave radiation field with the thruster plasma was performed on an experimental SPT model described in [6]. During these experiments, it was possible to shift the thruster relative to the transmitting antenna so that the microwave radiation acted upon various regions of the output plasma jet and upon different structural elements of the thruster. The measurements were performed at various frequencies in the range from 2 to 4 GHz, using radiation source power varied from 10^{-6} to 10^{-2} W (which corresponds to the energy parameters typical of the electromagnetic situation around a spacecraft). The microwave field intensity inside the vacuum chamber was measured in a peripheral region of the plasma jet, with the aid of a bifilar microwave probe providing for a spatial resolution of 1–1.5 mm. At the same time, the electromagnetic radiation intensity was measured with a broadband microwave antenna mounted outside, on a dielectric window of the vacuum chamber. The measuring receivers possessed a fluctuational sensitivity threshold as low as 10^{-15} W/MHz, which allowed the system to be calibrated relative to a standard microwave noise source [7]. Therefore, the results of measurements could be compared to the intensity of microwave fields both from the external radiation source and from the intrinsic oscillations in the plasma jet.

The experimental results lead to a conclusion that there are certain threshold values of the microwave field intensity at the plasma thruster above which the effect of amplification of the external radiation is manifested. When the microwave radiation envelope was measured at a time resolution on the order of 1 s (Fig. 2), the microwave field amplification coefficient near the thruster in the frequency range studied was 10–15 dB relative to the field intensity measured with the thruster switched off. The threshold levels are 3–4 orders of magnitude higher than the field intensity due to intrinsic plasma oscillations in the vicinity of a cathode-compensator. The amplification effect was most pronounced for the mutual arrangement of the transmitting antenna and the thruster such that the plasma jet produced no screening action upon the external radiation flux toward the thruster structure elements. As the thruster was displaced relative to the transmitting

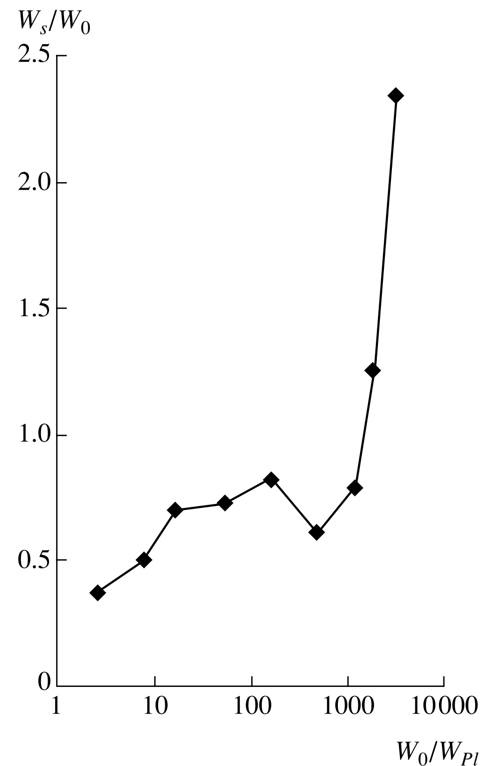

Fig. 2. The plot of the microwave amplification coefficient W_s/W_0 near the experimental thruster versus the external electromagnetic radiation intensity W_0/W_{Pl} (W_{Pl} is the energy density of the intrinsic microwave oscillations in a cathode region of the plasma jet).

antenna (Fig. 3), the observed pattern revealed characteristic zones featuring radiation action upon the plasma directly via the thruster elements (zone I), in the central part of the plasma jet (zone II), and from outside (zone III). In determining the amplification coefficient for each zone, the microwave field energy density was determined relative to that for the thruster switched off, which provided a correction for the contribution of microwave radiation reflected from thruster elements to the initial microwave field distribution. It should be noted that an increase in frequency is accompanied by a growth in the radiation intensity and by a decrease in the amplification threshold for the electromagnetic radiation acting upon the truster.

The obtained experimental data cannot be rationalized within the framework of common notions about the interaction of electromagnetic radiation and plasma. Therefore, a mechanism of the anomalous interaction of microwave radiation with an SPT plasma has to be established in order to explain the observed effects and, probably, take them into account in designing radio communications for space vehicles. There are two important factors indicated by the results of experiments. First, the observed effect is manifested in the range of Langmuir frequencies of electrons in the zone of neutralization of the accelerated ion flow. According

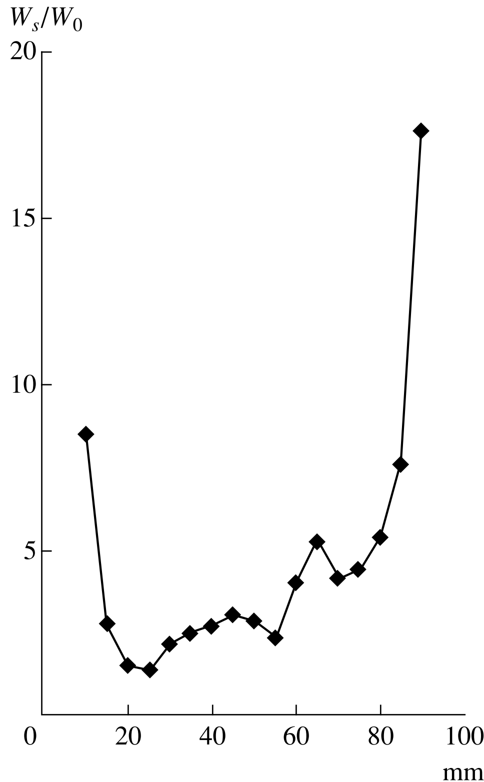

Fig. 3. The plot of microwave amplification coefficient W_s/W_0 versus transmitting antenna displacement relative to the thruster. Zones I–III correspond to antenna displacements within 0–20, 20–80, and 80–100 mm, respectively.

to [8], this zone is a source of microwave oscillations related to the development of a beam instability in the plasma jet. In various SPT operation regimes, the cathode-compensator potential relative to the plasma jet varies within 20–35 V at an accelerating voltage of 300–350 V. Under these conditions, the velocity of electrons injected into the plasma jet is (2.7–3.5) × 10^8 cm/s, which is significantly higher than the thermal velocity of electrons in the neutralization zone (1.5 × 10^8 cm/s) at an electron temperature of 5–7 eV [6]. According to the experimental data and related estimates [9], the relative density of a high-energy electron beam in the neutralization zone is $n_{eb}/n_{e0} \leq 0.1$ (n_{e0} is the density of low-energy electrons in the plasma jet).

It should be noted that, under real thruster operation conditions, there are limitations on the electron emission from a cathode-compensator, which leads to a significant increase in the cathode potential drop and in the velocity of electrons injected into the ion flow. Under these conditions, the beam instability development in the SPT plasma acquires a nonstationary character and the microwave radiation envelope exhibits considerable pulsations [5]. The same nonstationary character is typical of the secondary microwave radiation field observed in this experiment (Fig. 1).

The second important feature is a significant dependence of the amplification effect on the position of a transmitting antenna relative to the thruster elements (Fig. 3). This is related to the screening action of the plasma jet on the radiation transmission toward the cathode-compensator. The fact that the secondary radiation intensity increases with the frequency is consistent with a decrease in the screening action of the plasma jet upon electromagnetic radiation. This circumstance suggests that the radiation can act upon the SPT plasma by means of microwave fields induced in the thruster structure elements. The effect of such induced fields on the wave processes in the SPT plasma should be most significant in the region where electrons escape from the cathode-compensator. In this case, the cathode-compensator can be considered as an effective receiving antenna loaded on the plasma resistance in the electron escape region, the capacitive impedance of the near-electrode plasma layer, and the equivalent wave impedance of the thruster elements. The induced microwave field intensity depends on the ratio of the size of the cathode receiving the electromagnetic radiation to the characteristic size of the plasma region perturbed by the external microwave field. Under certain conditions, the intensity of perturbations significantly increases as compared to the intensity of fluctuational fields, which leads to modulation of the velocity of electrons injected into the thruster plasma. As a result, there is a microwave field buildup in time over the plasma jet volume: the thruster can be considered as a plasma-pumped microwave amplifier.

Estimates of the degree of amplification of the microwave fields induced in an SPT plasma can be obtained based on the existing notions about the instability of a modulated electron beam in a plasma [10, 11]. A sufficiently rigorous theory describing the interaction of electromagnetic radiation with an SPT plasma can hardly be developed at present because there are considerable difficulties in making allowance for a large number of important factors. These include distribution and orientation of radiation-field components near the elements of a particular spacecraft, the influence of a metal chamber employed in ground SPT tests, the inhomogeneous structure of a plasma jet, mechanisms of saturation of the amplification of induced microwave fields, and conversion of the plasma waves into electromagnetic radiation.

When the frequency of an electromagnetic wave acting upon the thruster plasma is close to the Langmuir frequency of electrons ($\omega \approx \omega_{Pe}$), we may neglect the capacitive impedance of the near-electrode plasma layer and the equivalent wave impedance of the thruster elements. In this case, a condition for electromagnetic radiation amplification in the SPT plasma can be written as follows:

$$(1/8\pi)(1 - R_A)(S_A/\Delta S_{Pl})(c/\Delta l_{Pl}\nu_e)W_0 > W_{Te},$$

where R_A is the coefficient of reflection of the incident

electromagnetic wave from a receiving part of the cathode-compensator and S_A is the effective area of this part; W_0 is the wave energy density; ΔS_{Pl} and Δl_{Pl} are the cross-section area and linear dimension of the microwave excitation region in the plasma; ν_e is the effective frequency of electron collisions; W_{Te} is the energy density of the thermal plasma oscillations in the region of frequencies $\omega \approx \omega_{Pe}$ [12]; $W_{Te} \approx (1/12\pi^2)(kT_e/r_{De}^3)$; and T_e and r_{De} are the temperature and Debye radius of electrons in a near-cathode region of the plasma jet. The threshold character of the radiation amplification and the conditions of manifestation of this effect under the action of an external electromagnetic field upon SPT elements are qualitatively confirmed by the results of experiments presented above (Fig. 2).

The degree of amplification of the induced microwave fields in the SPT plasma can be estimated using a linear theory developed for an electron beam interacting during a limited period of time with an inhomogeneous plasma [13]. The estimates based on this theory show that, for the values of parameters typical of the electron component of a thruster plasma, the coefficient of amplification of the induced microwave fields localized at the cathode-compensator can reach up to 50–60 dB. For an efficiency of conversion of the amplified plasma waves into electromagnetic waves on the order of 10^{-3}–10^{-2} [7], the secondary microwave radiation will produce a dominating contribution to the electromagnetic situation around a space vehicle. The related effects can be accompanied by amplitude, phase, and frequency distortions of signals in the radio channels and by mutual interference in the on-board receiving-transmitting equipment of communication satellites. This study is of special importance in view of the possible use of plasma devices as transmitting microwave antennas on space vehicles.

Acknowledgments. The author is grateful to A.I. Morozov, A.I. Bugrova, and A.I. Efimov for fruitful discussions of the results, and to V.L. Zarembo and A.V. Desyatskov for their help in conducting experiments.

REFERENCES

1. J. S. Sovey, L. M. Carney, and S. C. Knowles, J. Propul. Power **5** (5), 534 (1989).
2. S. G. Ohler, A. B. Ruffin, B. E. Gichrist, *et al.*, in *Proceedings of 32nd AIAA/ASME/SAE/ASEE Joint Propulsion Conference, Lake Buena Vista, 1996*, AIAA Pap. 96–2706 (1996).
3. G. G. Shishkin, in *Proceedings of II German–Russian Conference on Electric Propulsion Engines and Their Technical Applications, Moscow, 1993*, p. 111.
4. I. P. Kozlov, Pis'ma Zh. Tekh. Fiz. **27** (24), 71 (2001) [Tech. Phys. Lett. **27**, 1058 (2001)].
5. K. P. Kirdyashev, A. I. Efimov, and D. S. Lukin, Pis'ma Zh. Tekh. Fiz. **28** (3), 80 (2002) [Tech. Phys. Lett. **28**, 119 (2002)].
6. A. I. Morozov, A. I. Bugrova, A. V. Desyatskov, *et al.*, Fiz. Plazmy **23** (7), 635 (1997) [Plasma Phys. Rep. **23**, 587 (1997)].
7. K. P. Kirdyashev, *High-Frequency Wave Processes in Plasmadynamic Systems* (Énergoatomizdat, Moscow, 1982), p. 142.
8. K. P. Kirdyashev and A. I. Morozov, Fiz. Plazmy **25** (4), 326 (1999) [Plasma Phys. Rep. **25**, 293 (1999)].
9. A. I. Morozov and V. V. Savelyev, in *Reviews of Plasma Physics*, Ed. by B. B. Kadomtsev and V. D. Shafranov (Consultants Bureau, New York, 2000), Vol. 21, pp. 203–391.
10. A. K. Berezin, G. P. Berezina, L. I. Bolotin, *et al.*, in *Plasma Physics and Problems of Controlled Nuclear Fusion* (Naukova Dumka, Kiev, 1965), Vol. 4, pp. 129–143.
11. G. A. Bernashevskiĭ, E. V. Bogdanov, V. Ya. Kislov, *et al.*, in *Microwave Plasma and Electron Amplifiers and Oscillators*, Ed. by Z. S. Chernov (Sov. Radio, Moscow, 1965), p. 96.
12. *Radiation Processes in Plasmas*, Ed. by G. Bekefi (Wiley, New York, 1966; Mir, Moscow, 1971).
13. D. D. Breĭzman and D. D. Ryutov, Zh. Éksp. Teor. Fiz. **57** (4), 1401 (1969) [Sov. Phys. JETP **30**, 759 (1970)].

Translated by P. Pozdeev

Technical Physics Letters, Vol. 29, No. 1, 2003, pp. 81–83. Translated from Pis'ma v Zhurnal Tekhnicheskoĭ Fiziki, Vol. 29, No. 2, 2003, pp. 88–94.
Original Russian Text Copyright © 2003 by Elistratov, Shibkov.

An Analysis of Nonlinear Ion Drift Spectrometry for Gas Detectors with Separating Chamber of Planar Geometry

A. A. Elistratov and S. V. Shibkov
Institute of Cryptography, Communications, and Informatics, Moscow, Russia
e-mail: elist@fssr.ru
Received August 6, 2002

Abstract—A consistent analytical model of nonlinear ion drift spectrometry for modern gas analyzers is developed. A procedure for determining the field dependence of the ion mobility using the experimental data is described. An ionogram is calculated for the case of a flat drift chamber and polynomial character of the field dependence of the ion mobility. © *2003 MAIK "Nauka/Interperiodica"*.

Nonlinear ion drift spectrometry (NIDS), characterized by a detection limit on the order of $\sim 1 \times 10^{-12}$ kg/m^3, is one of the most sensitive methods for detecting traces of explosives and drugs in the atmosphere [1]. However, to our knowledge, no consistent analytical model of this method has been developed so far.

The typical scheme of a gas detector employing the NIDS principle was described in detail elsewhere [2, 3]. Here, we only briefly point out that a drift chamber represents a flat capacitor with plate electrodes of length l and width a, spaced by a gap of width d through which the air (containing impurity ions to be determined) is pumped at a flow rate u. Occurring inside the capacitor, ions perform transverse oscillations under the action of alternating high-frequency ($f \sim 10^5$–10^6 Hz) asymmetric electric field $E(t) = E_s(t) + E_c$, where $E_s(t)$ is the alternating separating field satisfying the conditions $\langle E_s \rangle = 0$, $\langle E_s^{2k+1} \rangle \neq 0$ ($k = 1, 2, 3\ldots$) and E_c is a small slowly varying component (compensating field).

The NIDS method is based on the nonlinear relationship between the drift velocity v of heavy impurity ions in a light carrier gas and the electric field strength E in moderately strong alternating electric fields [4]. The character of the behavior of ion mobility, defined as $k(E) = v/E$, is individual for ions of each kind. By selecting a small (relative to the alternating component $E_s(t)$) quasiconstant compensating field E_c, it is possible to allow only ions of a certain kind to pass through the drift chamber of the gas detector.

Distribution of the velocities of molecules of a neutral gas across a tube can be considered as homogeneous. This is explained as follows.

(i) The gas can be considered as incompressible because the flow velocity ($u \sim 15$ m/s) is much lower as compared to the velocity of sound in air.

(ii) The gas flow in a drift chamber is laminar, because the Reynolds number $R = ud/\mu \sim 500$ is much smaller than the critical value ($\mu \approx 0.15$ cm^2/s is the kinematic viscosity).

(iii) A typical length of the drift chamber ($l \sim 1$ cm) is much smaller than the characteristic scale $L = dR \sim 20$ cm on which the velocity distribution obeys the Poiseuille law.

This circumstance allows the motion of ions in the transverse electric field to be treated as quasi-one-dimensional. Using the continuity equation, $\partial n/\partial t + \mathrm{div}\mathbf{J} = 0$, and an expression for the ion current $\mathbf{J} = -D\nabla n + nk\mathbf{E}$ (D is the diffusion coefficient of ions in the gas), we obtain an equation describing the ion concentration as a function of transverse coordinate x and time t:

$$\frac{\partial n}{\partial t} = D\frac{\partial^2 n}{\partial x^2} - kE\frac{\partial n}{\partial x}.$$

In order to estimate the relative value of each term in this equation, it is convenient to pass to dimensionless variables: the coordinate $\xi = x/d$ and time $\tau = (D/d^2)t$. As a result, the above equation takes the form

$$\frac{\partial n}{\partial \tau} = \frac{\partial^2 n}{\partial \xi^2} - \eta\frac{\partial n}{\partial \xi}, \quad (1)$$

in which the dimensionless coefficient $\eta = (dk/D)E$ (called the Peclet number) amounts to $\sim 10^4$ over most of the period, which implies that the convective term is dominating. As is known, solutions to Eq. (1) in this range represent essentially nonequilibrium distributions characterized by the formation of shock waves and lines of tangential discontinuities.

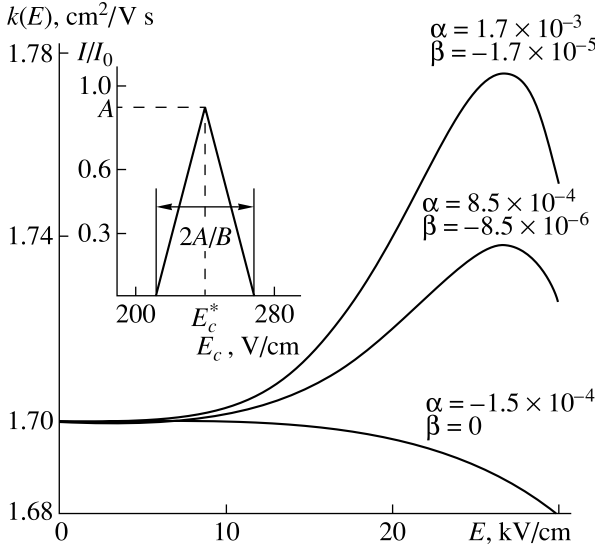

Fig. 1. The plots of ion mobility k versus electric field strength E calculated for $n = 2$, $m = 4$, and various values of α and β. The inset shows a peak of the ionogram corresponding to the upper curve.

To a first approximation, we may neglect the diffusion term in Eq. (1) and reduce the order of this differential equation. The influence of diffusion on ion motion is significant only for time intervals on the order of $d^2/D \sim 10^{-3}$ s (comparable with the time of an ion staying in the drift chamber). These effects are considered in [5]. Passing from the analysis of an ensemble of noninteracting particles to the description of motion of a single particle and returning to the dimensional variables, we obtain an equation for the characteristics:

$$\frac{dx}{dt} = kE(t). \tag{2}$$

Let us ignore the effects related to the possibility of formation of a bulk ion charge. These effects become significant for an ion concentration on the order of $n \sim \varepsilon_0 E/ed \sim 10^{17}$ m^{-3} (e is the electron charge), which corresponds to the ion current of $I = jS = enuad \sim 10^{-7}$ A. Thus, we consider the case of lower ion currents.

For most of the period T, the system features a field strength of $E \sim 5$ kV/cm. At a pressure of $\sim 10^5$ Pa, this value is classified as a moderately strong field [4]. For this regime, expression for the mobility has not yet been derived from the basic physical laws, hence we will write an expression for the ion mobility in the form of a polynomial convenient for comparison with experiment:

$$k(E) = k_0\left(1 + \alpha\left(\frac{E}{E_{\max}}\right)^{2n} + \beta\left(\frac{E}{E_{\max}}\right)^{2m}\right), \tag{3}$$

where k_0 is the mobility in the zero-field limit; m and n are integers such that $m > n > 0$; α and β ($\alpha, \beta \ll 1$) are dimensionless coefficients determining the relative contribution of the nonlinear component of mobility; and $E_{\max}$ is the electric field strength above which it is necessary to take into account the dependence of k of the field strength. According to the experimental data [2, 3, 6], for most substances $E_{\max} \approx 10$ kV/cm.

Upon integrating Eq. (2), it is possible to determine the shape of the ionogram—a curve representing dependence of the ion current I on the compensating field strength E_c (see the inset in Fig. 1). The value of $E_c = E_c^*$, determining the position of the peak on the ionogram, corresponds to a selection rule that can be formulated as follows: $\Delta x(T) = x(T) - x(0) = 0$. As a result, we obtain to within terms linear in α and β

$$E_c^*(E_{s0}) = -\left(\frac{\alpha}{E_{\max}^{2n}}\langle E_s^{2n+1}\rangle + \frac{\beta}{E_{\max}^{2m}}\langle E_s^{2m+1}\rangle\right), \tag{4}$$

where E_{s0} is the maximum value of the separating field $E_s(t)$ over the period $t \in [0; T]$. Simple geometric considerations lead to an expression for the ionogram:

$$\frac{n(E_c)}{n_0} = \begin{cases} A - B|E_c - E_c^*| & \text{at} \quad |E_c - E_c^*| < A/B, \\ 0 \quad \text{at} \quad |E_c - E_c^*| > A/B, \end{cases} \tag{5}$$

where A and B are the constants determined by the formulas

$$A = 1 - c\left\{\langle E_c\rangle_\tau + \frac{\alpha}{E_{\max}^{2n}}(\langle E_s^{2n+1}\rangle_\tau - \tau_1\langle E_s^{2n+1}\rangle)\right.$$
$$\left. + \frac{\beta}{E_{\max}^{2m}}(\langle E_s^{2m+1}\rangle_\tau - \tau_1\langle E_s^{2m+1}\rangle)\right\},$$

$$B = cN\left\{1 + \frac{\alpha}{E_{\max}^{2n}}(2n+1)\langle E_s^{2n}\rangle + \frac{\beta}{E_{\max}^{2m}}(2m+1)\langle E_s^{2m}\rangle\right\}.$$

Here, $N = lf/u$ is the number of voltage periods during which the particles stay inside the gap, $c = k_0T/d$, $\tau_1 = t_1/T$, t_1 is the time instant such that $E_s = 0$, and

$$\langle E_s^p\rangle_\tau = \int_0^{t_1}(E_s(t))^p dt.$$

As an example of application of the proposed approach, let us calculate the field dependence of mobility for the ions of tertiary amines using the experimental data reported in [3]: $d = 0.5$ mm, $a = 5$ mm, $l = 15$ mm, air flow rate 2 l/min, $f = 2$ MHz, a maximum value of $E_{s0} = 30$ kV/cm, $E_c = -60$–240 V/cm. For definiteness, the separating field is taken in the form of an

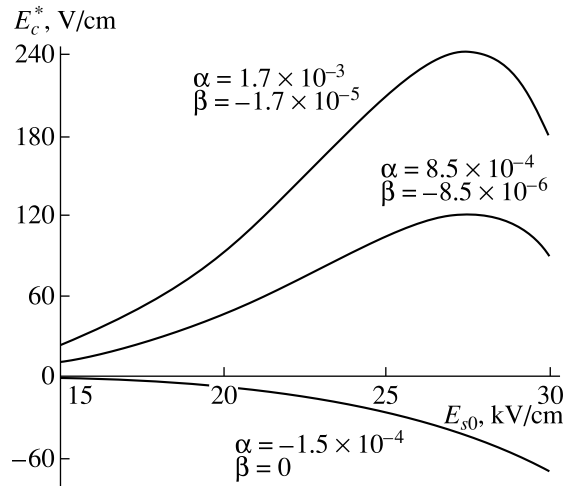

Fig. 2. The plots of $E_c^*(E_{s0})$ calculated for $n = 2$, $m = 4$, and various values of α and β.

asymmetric ramp $E_s(t) = \{E_{s0}(T/t_1 - 1), 0 < t < t_1; -E_{s0}, t_1 < t < T\}$, where the moment of switching of the separating field polarity is $t_1 = 0.8T$. An analysis shows that the best fit to experimental curves of $E_c^*(E_{s0})$ is obtained for $n = 2$, $m = 4$, and α, β as indicated in Fig. 2. Using these n, m, α, and β, it is possible to reconstruct the dependence of k on E from the experimental data (Fig. 1).

In concluding, it should be noted that the proposed approach can be of interest as the limiting case for an analysis of a cylindrical drift chamber [7]. This design makes it possible to use a focusing regime. Operation of such a chamber will be considered in a special publication.

Acknowledgments. The authors are grateful to Prof. S.D. Beneslavskii, E.M. Maksimov, V.G. Pronin, and V.V. Ionov for fruitful discussions.

REFERENCES

1. M. P. Gorshkov, USSR Inventor's Certificate No. 966583; Byull. Izobret., No. 38 (1982).
2. I. A. Buryakov, E. V. Krylov, A. L. Makas', *et al.*, Pis'ma Zh. Tekh. Fiz. **17** (12), 60 (1991) [Sov. Tech. Phys. Lett. **17**, 446 (1991)].
3. I. A. Buryakov, E. V. Krylov, A. L. Makas', *et al.*, Zh. Anal. Khim. **48**, 156 (1993).
4. E. McDaniel and E. Mason, *The Mobility and Diffusion of Ions in Gases* (Wiley, New York, 1973; Mir, Moscow, 1976).
5. A. V. Kudryavtsev and A. L. Makas, *Proceedings of the 10th Int. Conf. on IMS* **4** (2), 117 (2001).
6. E. G. Nasarov, R. A. Miller, G. A. Eiceman, *et al.*, *Proceedings of 10th Int. Conf. on IMS* **4** (2), 43 (2001).
7. I. A. Buryakov, Yu. N. Kolomiets, and V. B. Luppu, Zh. Anal. Khim. **56**, 381 (2001).

Translated by P. Pozdeev